I. Rupture Properties of Large Subduction Earthquakes

II. Broadband Upper Mantle Structure of Western North America

Thesis by

Timothy Ian Melbourne

In Partial Fulfillment of the Requirements

for the Degree of

Doctor of Philosophy

Caltech

Pasadena, California

1998

(Submitted December 30, 1997)

Acknowledgements

My time here in the Seismo Lab has proven thoroughly enjoyable almost without exception, and for this there are many thanks.

First and foremost, my parents showed me early on the deep satisfaction obtained from a mechanistic understanding of the world. That I've spent my first 30 years in school is itself testament to and acknowledgement of their efforts. I also thank them for instilling the critical skeptism which has served me well and will no doubt prove invaluable henceforth. Finally, and above all, they've been great parents all around and I count myself extremely lucky.

Joann and Don have kept things fun and interesting all the while and have given me a remarkable amount of freedom to do as I please. It's my hope that I will be able to emulate their attributes with my students down the line.

Frank Webb helped me immensely with all things GPS, from supplying complete data processing scripts to generating new research ideas.

My lab cohorts-students and staff alike, it's my dubious hope that I've put out as much as I've soaked up. Thanks for just about everything. Dr. Sizmo Scrivner has been very helpful across the board and saved great amounts of my time by explaining the endless minutae of grad student existence. Lupei Zhu was also very generous with the use of his FK codes and was a fountain of technical help.

Sharon Kedar and Miriam Jackson made possible endless months of idyll chatter and superfluous bantering without which my experience here would have been both severely shortened and much more productive.

Lastly, Anne Marie Jorunn Johansen has made life the most fun of all with her ideas, strength and vitality.

TeX-master: t

Abstract

This thesis contains two studies, one of which employs geodetic data bearing on large subduction earthquakes to infer complexity of rupture duration, and the other is a high frequency seismological study of the upper mantle discontinuity structure under western North America and the East Pacific Rise. In the first part, we present Global Positioning System and tide gauge data which record the co-seismic deformation which accompanied the 1995 M_w8.0 Jalisco event offshore central Mexico, the 1994 M_w7.5 Sanriku event offshore Northern Honshu, Japan, and the 1995 M_w8.1 Antofagasta earthquake offshore Northern Chile. In two of the three cases we find that the mainshocks were followed by significant amounts of rapid, post-seismic deformation which is best and most easily explained by continued slip near the co-seismic rupture patch. In Jalisco, we find that the post-seismic deformation which occurred during the two weeks following the mainshock amounted to as much 70% of the co-seismic deformation, from which we estimate an additional moment release of 40%, while in the Sanriku event an additional 30% moment release followed in the 10 days after the mainshock. Because of the favorable geometry of the Jalisco network, we infer that the post-seismic faulting occurred predominantly down-dip of the co-seismic rupture plane. This is the first documented case of rapid slip migration following a large earthquake, and is pertinent to earthquake prediction based on precursory deformation. Following the Antofagasta mainshock there was no rapid post-seismic displacement within the resolution of the GPS measurements, which equals roughly 1% of the co-seismic displacement. As the three GPS data sets represent the best observations of large subduction earthquakes to date and two of them show significant amounts of aseismic energy release, they strongly suggest silent faulting may be common in certain types of subduction zones. This, in turn, bears on estimates of global moment release, seismic coupling, and our understanding of the natural hazards associated with convergent margins.

The second part of this dissertation utilizes high frequency body waves to infer the upper mantle structure of western North America and the East Pacific Rise. An uncharacteristically large M_w5.9 earthquake located in Western Texas provided a vivid topside reflection off the 410 Km velocity discontinuity ("410"), which we model to infer the fine details of this structure. We find that, contrary to conventional wisdom, the 410 is not sharp, and our results help reconcile seismic observations of 410 structure with laboratory predictions. By analyzing differences between our structure and seismic 410 structure estimates under the nearby Gulf of California, we attempt to extract differences in temperature and mineralogy between subcontinental and suboceanic 410 structures.

Extending this analysis, we utilize teleseismic events from East Pacific Rise transform faults to model multiple S upper mantle triplications. We find that for raypaths traversing the rise crest the 1-D model TNA [Grand and Helmberger (1984)] derived for the western US accurately predicts differential SnS-S travel times and triplication waveform structure, implying that there is little velocity heterogeneity along the ridge crest along nearly its entire length. We find that for energy traversing paths increasingly away from the ridge axis there is no discernible change in the apparent depth of the 410 and 670 Km discontinuities. In the shallowest mantle (uppermost 75 Km), there is a strong lateral shear velocity gradient amounting to 3% over roughly 150 Km. The LID, nonexistent at the ridge crest, grows slowly in thickness beyond 150 Km from the axis. The compatible geodynamic model of these two results is that the East Pacific Rise is not fed from the local lower mantle, rather, upper mantle material must be transported laterally to supply the ridge axis spreading center, and the LID reflects the source region of the East Pacific Rise magma supply.

Contents

Acknowledgements iii

Abstract v

1 Introduction 1

2 The Geodetic Signature of the Mw8.0 1995 Jalisco Subduction Earthquake 6

2.1 Abstract . . . 6
2.2 Introduction . . . 6
2.3 GPS Observations . . . 7
2.4 Inversion . . . 10
2.5 Discussion . . . 12
2.5.1 Subduction of the Rivera Plate . . . 14
2.5.2 Tsunami Constraints . . . 15
2.5.3 Sediment Rheology . . . 15
2.5.4 A Hazards Model for Cascadia? . . . 16
2.6 Acknowledgments . . . 18

3 The Demonstration and Mechanics of Rapid, Postseismic Deformation in Subduction Zones 19

3.1 Abstract . . . 19
3.2 Introduction . . . 20
3.3 Data . . . 22
3.3.1 The 1995 Jalisco Earthquake . . . 24
3.3.2 1994 Sanriku-Hakura-Oki . . . 33
3.3.3 1995 Antofagasta Event . . . 36

3.4 Slip Distributions 42
3.4.1 Deformation Modelling 42
3.5 Discussion 52
3.6 Acknowledgements 59

4 Fine Structure of the 410 Km Discontinuity **60**
4.1 Abstract 60
4.2 Introduction 61
4.3 Data 63
4.4 Synthetics 72
4.5 Interpretation 81
4.6 Discussion and Conclusions 83
4.7 Acknowledgments 86

5 The Broadband Structure of the East Pacific Rise Axis **87**
5.1 Abstract 87
5.2 Introduction 88
5.3 Data 90
5.3.1 A Survey of Triplicated S **Multiples** 93
5.4 Modeling 103
5.4.1 F-K Synthetics 103
5.5 Evolution of the Lid 120
5.6 Discussion 134

Bibliography **137**

List of Figures

2.1 Coseismic Displacements 8
2.2 Slip Distribution 11
2.3 Finite Fault Vertical Deformation 13

3.1 Coseismic Displacements 23
3.2 CRIP Daily Solutions and Rapid Postseismic Displacements at Jalisco, Mexico 25
3.3 Rapid Postseismic Displacements at Jalisco, Mexico 26
3.4 Rapid Postseismic Tide-Corrected Displacements at Jalisco, Mexico . 27
3.5 Manzanillo Harbor Six Minute Tide Gauge Measurements 29
3.6 Tide Gauge Estimate of Co-seismic subsidence, Transient Removed . 30
3.7 Differenced Tide Gauge Measurements: Puerto Vallarta - Manzanillo. 31
3.8 Differenced Tide Gauge Measurements: Acapulco - Manzanillo. . . . 32
3.9 1994 Co-seismic Displacements at Sanriku-Hakura-Oki 34
3.10 Rapid Postseismic Displacements at Sanriku 35
3.11 South American Geodynamics Array (SAGA) 38
3.12 SAGA Co-seismic Displacements from the 1995 Antofagasta Earthquake 39
3.13 Antofagasta Continuous GPS Measurements During the July 30, 1995, Earthquake 40
3.14 Comparison of Trench-Receiver Geometries for 3 Subduction Zone GPS Datasets 41
3.15 Finite Fault Vertical Deformation 43
3.16 Shallow Thrust Fault Horizontal Deformation 44
3.17 Variable Fault Vertical Dislocation Models 47
3.18 Variable Fault Trench-normal Deformation Models 48
3.19 Horizontal Vs Vertical Surface Deformation for Thrust Faults 50

3.20 Sediment Thickness Map at Jalisco, Sanriku and Antofagasta 58

4.1 Station Locations 63
4.2 Short Period Data and Stacks 64
4.3 Wood-Anderson Long Period Data 66
4.4 Vertical Short Period Data from 10/06/96 Vancouver Island Event . . 68
4.5 Vertical SP Data from 8/28/95 Baja California Event 69
4.6 Synthetic Velocity Models 73
4.7 Linear 410 Short Period Synthetics 75
4.8 Long Period Synthetics 76
4.9 Double 410 Short Period Synthetics 78
4.10 Composite 410 Short Period Synthetics 79

5.1 Raypaths of Triplicated Mulitple S Phases 89
5.2 Transverse Component of East Pacific Rise Events Recorded on West Coast Arrays 91
5.3 Data Raypaths for Events Along the East Pacific Rise 92
5.4 *S* Emergence from Love Wave 94
5.5 Moveout of the D and F Branches of *S* 95
5.6 Moveout of the A and C Branches of *SS* 97
5.7 Crossing of AB-CD and CD-EF Branches of *SS* 98
5.8 *SSS* -G Phase Separation 99
5.9 Moveout of F and D Branches of *SSS* 100
5.10 Tectonic North America-PREM Velocity Model 104
5.11 Comparison of FK Synthetics with Data for D and F Branches of *SSS* 106
5.12 Comparison of FK Synthetics with Data for D and F Branches of *SSS* - 69°-71° and 73°-74.5° 107
5.13 Blowup of Synthetic-Data *SSS* Misfit 108
5.14 *S* 670 Triplication; D-F Branch Moveout and FK Synthetics 110
5.15 Data and Synthetics of *SS* 410 triplication, Back Branch 111
5.16 *SS* Delays Contoured with Raypaths 113

5.17 Breakout of Inland and Coastal Stations arrival of the A and C Branches of *SS* 114
5.18 Topography, Bathymetry and Raypaths of *SS* Phases 115
5.19 Enlargement of Figure 5.18 116
5.20 Modified TNA with a Lid 118
5.21 Data and Synthetics of *SS* 410 and 670 Triplications 119
5.22 Modified TNA Synthetics with Data for D and F Branches of *SSS* . 121
5.23 Data and Synthetics of Moveout of A,C and D,F Branches of *SSS* . . 122
5.24 Data and Synthetics of Moveout of A,C and D,F branches of *SSS* . . 123
5.25 Data and Synthetics from Modified TNA of *SS* 410 and 670 Triplications 125
5.26 Modified TNA Synthetics for *S* 670 Triplication; D-F Branch Moveout and FK Synthetics 126
5.27 Modified TNA with LIDs suitable for *SSS* and *SS* data 128
5.28 Data and Synthetics from Modified TNA of *SS* 410 and 670 Triplications 129
5.29 Data and Synthetics of Moveout of A,C and D,F Branches of *SSS* . . 130
5.30 Modified TNA Synthetics with Data for D and F Branches of *SSS* . 131
5.31 Raypaths of Gulf of California Event 132
5.32 Contoured *S* Delays with Raypaths 133

List of Tables

2.1 Table of Coseismic Displacements and Model Results 9
2.2 Table of Model Results and Misfit 10

Chapter 1 Introduction

This thesis is composed of and presented in two disparate parts, and follows in a roughly chronological fashion my time spent in the Caltech Seismological Laboratory. The first part, entitled "Faulting Dynamics of Large Subduction Earthquakes," is a detailed geodetic investigation of subduction zone fault mechanics in which I analyze, under the guidance of Joann Stock, three high resolution GPS data sets which bear on large subduction earthquakes. In Chapter II, I map the surface deformation produced by the M_w 8.0 1995 Jalisco earthquake in terms of the slip distribution at depth and show that this earthquake was characterized by faulting sufficiently shallow that it is usually considered unlikely to occur at such depths. However, the geometry of our network and the nature of the measurements leave little room for doubt that in this particular earthquake such shallow faulting did in fact occur and that this narrow plate interface released a magnitude 8's worth of seismic energy, a result which is extremely important for evaluating the potential seismic risk associated with subduction zones such as Cascadia. After developing the manner in which the GPS data were processed, modelled, and interpreted, I discuss the possible causes of such shallow faulting and relate this observation to the mechanical role of subducted sediments, which are sparse offshore central western Mexico relative to the global average.

In addition to the co-seismic geodetic signal, we also recorded in Jalisco evidence that slip continued to occur downdip of the co-seismic fault plane during the weeks following the mainshock. We can definitively state that the post-seismic slip was located predominantly downdip of the mainshock rupture plane, rather than within the same region as the mainshock rupture, due to the unique geometry of our network relative to the co-seismic rupture. Chapter III is devoted to the modelling and interpretation of this observation from Jalisco. Because six days passed after the earthquake before we could re-occupy our network, we resort to tide gauge data from those six days to estimate the faulting which occurred during the time not covered

by GPS measurements. Relying on the tide gauge data, we find that an additional 40% of the co-seismic strain energy was released during the two weeks following the mainshock. However, the tidal data is noisy, and there is significant uncertainty with this estimate. Relying on only the GPS measurements, however, we find that at the minumum an additional 10% extra moment was released during the period from 6 to 15 days following the earthquake. Because these data do not include the week immediately following the event, this latter figure must be considered to be a lower limit of energy released post-seismically during this event.

Additionally, in this chapter we incorporate and discuss continuous GPS time series from two other recent large subduction earthquakes, the 1994 Sanriku earthquake (M_w 7.5), which ruptured the Japan Trench, and the 1995 Antofagasta, Chile, event (M_w 8.1), which occurred along the Nazca-South American plate interface offshore northern Chile. The Sanriku data set contains a superlative set of measurements showing clear post-seismic moment release, but unfortunately possesses a geometry which is not sensitive for differentiating the down-dip extent of rupture between the co- and post-seismic rupture planes. The Antofagasta data set, however, comes from a station which has continuous GPS measurements both before and after the earthquake and which was ideally situated approximately at the vertical deformation hingeline during the event. It therefore combines the sensitive geometry of the Jalisco data with the continuity of the Sanriku data set and is therefore perfectly suited to mapping, within inherent limits, deviations in the post-seismic faulting from the co-seismic. However, we find no evidence for any rapid post-seismic deformation whatsoever, and can state that no post-seismic faulting with net moment greater than about 1% of the co-seismic occurred here. This naturally begs the question of why some faults should continue to creep following large earthquakes while others do not. Plausible speculations are presented in the discussion section of this chapter.

Together, these three data sets represent the most detailed geodetic observations of large subduction earthquakes to date, and in two of the three cases there is compelling evidence that a large fraction of the total energy released occurred aseismically immediately following the earthquake. These observations constitute a definitive statement

that the general behavior of subduction zone faulting is not necessarily a temporal delta function, but rather one which is characterized by strong heterogeneity in duration and rate of energy release. They indicate that rapid aseismic afterslip may be common but has gone previously unnoticed due to the lack of continuous measurements. This idea bears heavily on ideas pertaining to natural hazards mitigation related to convergent margins and estimates of global seismic coupling. As in Chapter II, we explore faulting mechanisms in terms of sediment rheology, thermodynamics, and abundance, and suggest that the continued slip can be explained in terms of the velocity-strengthening behavior of the sediments in this particular subduction zone.

The second part of this thesis is a seismological investigation of the upper mantle structure of Western North America. Chapter IV is a straightforward application of high frequency body waveform modeling aimed at identifying the fine structure of the 410 km discontinuity. The data in this study is a strong topside bounce produced by a relatively large event in Western Texas recorded by the short period and broadband arrays deployed along the west coast of the US. Nearly 400 vertical short period and 24 broadband instruments are used to constrain structure, affording us an unprecedented level of resolution in evaluating different models. The structure which best fits the Texas data is a composite structure containing a linear gradient (3.5% compressive velocity change over 12 radial Km) overlying a sharp offset of 3%. This is the first high frequency seismic demonstration of fine structure in the 410 Km discontinuity and represents a major step towards resolving the longstanding discrepancy between seismic observations and thermodynamic predictions of what the fine structure of the 410 km discontinuity should be. It is only the incredibly dense seismic observations which allow the resolution of the subtle details in our structure. One interesting implication of our model is that it predicts the visibilty of 410 arrivals to be dependent on source spectrum and therefore helps explain the noted inconsistency of 410 arrivals even among events traversing similar propagation paths.

Our model of the 410 can be interpreted within the existing literature bearing on mineralogic constraints of the 410 Km discontinuity to yield temperature and

composition estimates of the mantle at 410 Km depth under western North America. In the discussion section of Chapter IV, we review the existing literature pertaining to 410 thermodynamics and summarize seismic inferences of 410 structure. Given the numerous studies and reasonable consensus that the 410 under the Gulf of California is in fact sharp, the differences between our 410 structure and that appropriate for the Gulf are due either to temperature or compositional differences, or both, and in this section we explore that possibility. We find that a temperature decrease of about 200-250 C° is expecteed to cause a net change in thickness of the 410 Km discontinuity of about 10 Km, which is roughly consistent with our observation.

In Chapter V, we model whole transverse seismograms recorded on North American broadband networks which traverse profiles along the East Pacific Rise. Five transform events form a nearly continuous record section ranging from 8° to 82° in distance whose transverse components show S, SS, SSS, and SSSS arrivals clearly triplicated by upper mantle discontinuities. The waveform shape of these triplicated arrivals provides a sensitive diagnostic of average discontinuity depth, from which we find that there is no discernible variation over great distances ($\sim$1000 Km) from the ridge axis. This result implies that the East Pacific Rise is not supplied directly with local lower mantle material. In the shallowest mantle, we find evidence of systematic growth of a high velocity zone, or LID, with distance from the ridge axis. Along the EPR crest proper, a modification of the 1-D model Tectonic North America (Grand and Helmberger (1984)) to contain a 7 Km thick crust adequately predicts the overall arrival times of the individual triplication branches, but increasingly off-axis energy requires a 3.5% velocity increase over 150 Km laterally within the upper 70 Km of the mantle to model emergent A-B branch direct-S phases. For raypaths near the Gulf of California, there is no correlation of the boundaries of this LID with the Baja peninsula, indicating that the surface expression of the peninsula is not simply related to the uppermost mantle velocity immediately below it. For more distant events with raypaths lying well offshore, the existence of the LID is supported by the relative amplitudes of the triplicated multiple S phases. Together these show that the LID forms rapidly near the ridge axis and continues to evolve outside of the immediate

vicinity of the axis.

Chapter 2 The Geodetic Signature of the Mw8.0 1995 Jalisco Subduction Earthquake

2.1 Abstract

The October, 1995, Mw 8.0 Jalisco subduction earthquake has provided a thorough geodetic observation of the coseismic subduction process. An 11-station regional GPS network located directly onshore from the rupture demonstrates consistent vertical subsidence verified by tide gauge data and southwest-directed extension, with measured displacements reaching 1 meter. Unusually shallow and non-uniform faulting is required to explain the displacements. We determine that up to 5 meters of slip occurred within the upper 15 km of the thrust fault zone and 2 meters possibly as shallow as 8 km, and that slip was likely distributed in two main patches. The paucity of continental sediments in this subduction zone could be responsible for the anomalously shallow faulting.

2.2 Introduction

The October 09, 1995, Mw 8.0 subduction zone earthquake located near Manzanillo, Mexico, was well recorded by an 11-station regional GPS network located directly onshore of and bracketing the epicentral region, giving a detailed geodetic view of the subduction process. The largest event in 60 years along the active Northern Middle America subduction zone, this earthquake produced widespread coastal subsidence rather than the uplift characteristic of most large subduction events [Tsuji *et al.* (1995); Tabei *et al.* (1996); Savage (1983); Thatcher (1984)]. Through inversion of the

geodetic data, we find that the cause of the anomalous behavior is extremely shallow faulting. This earthquake broke the uppermost regions of the subduction zone, and much of the slip occurred at depths usually considered to be unlikely to undergo brittle failure, typically those above 10 km and characterized by unconsolidated wet sediments which deform by gradual creep [Byrne *et al.* (1988); Marone and Scholz (1988)]. We hypothesize that the relative lack of continental derived sediments within the Northern Middle America subduction zone allows the anomalously shallow seismic front.

2.3 GPS Observations

The Jalisco GPS network was first occupied in March of 1995, seven months prior to the Mw 8.0 earthquake of October 09, 1995[1]. Fifteen stations were occupied with dual frequency P-code receivers for three days each, with the exception of one coastal station at Manzanillo, which was occupied for nine days. Following the earthquake, the network was re-occupied six days after the mainshock, and 11 stations were re-measured over the following week. The GIPSY-OASIS II software [Lichten and Border (1987)] and ephemerides and satellite clock corrections provided by the Jet Propulsion Laboratory for the International Geodynamics Service [Zumberge *et al.* (1995)] were used to reduce the data to absolute displacements within the ITRF'94 reference frame [Zumberge *et al.* (1997)]. Average station coordinate repeatabilities (scaled such that χ^2=1) from the first occupation were 4, 8 and 14 mm in North, East and Vertical components.

The long-term tectonic deformation rates within our GPS network are not expected to exceed several millimeters/yr (Allan (1986)) and may be as low as 1 mm/yr (Ferrari and Rosas (1996)), and any inter-seismic strain associated with the roughly 2 - 5 cm/year Rivera-North America plate convergence [DeMets and Stein (1990); Kostoglodov and Bandy (1995)] during the seven months between network occupa-

[1]National Earthquake Information Center (NEIC), Electronic report of revised Harvard CMT solutions, October, 1995

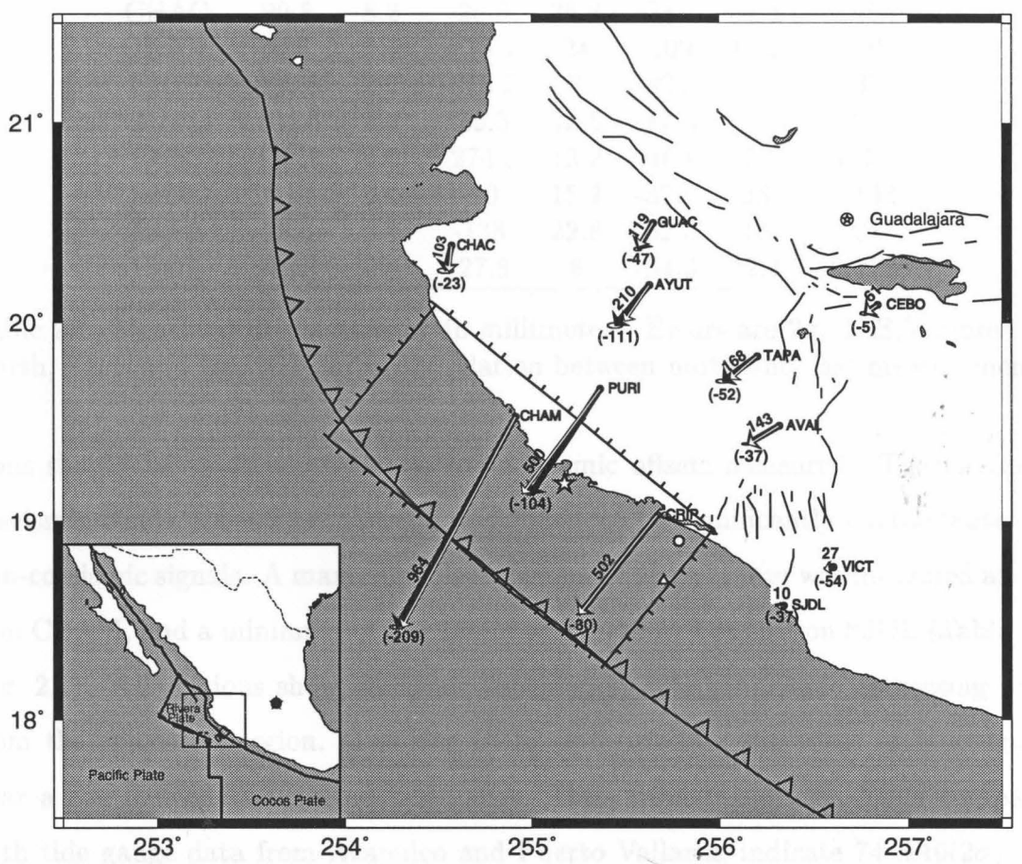

Figure 2.1: Coseismic displacements for the Oct., 1995, Rivera plate subduction earthquake (Mw=8.0). GPS measurements are shown as solid black vectors, with amount (in millimeters) of horizontal offset written along the vector and vertical offset in parentheses at the vector tip. GPS vectors at stations SJDL and VICT point west. Ellipses represent 2D 95% confidence intervals. Thin white vectors are modeled from slip distribution in Fig. 3. Gridded rectangle is the surface projected model fault plane, and the Harvard and Caltech centroids and the NEIC epicenter are indicated by the star, circle and triangle, respectively. Inset. The Rivera and Cocos plate subduction zones.

Station	GPS Displacements						
ID	N	Nerr	E	Eerr	V	Verr	NE_Cor
AVAL	-72.2	3.2	-124.7	16.4	-37.8	33	0.187
AYUT	-160.8	8.8	-137	25	-111	87.6	0.026
CEBO	-34	5.2	-50.5	14.4	-5	37.8	0.075
CHAC	-99.8	8.2	-25.6	25.8	-23.1	54.4	0.194
CHAM	-836	6.4	-479.1	24	-209	47.2	0.25
CRIP	-392.8	2.2	-315.2	7	-80.3	14.8	0.073
GUAC	-104.6	5.4	-59.3	12.6	-47.5	34	0.285
PURI	-417.9	4.6	-274.6	13.2	-104	30.6	0.17
SJDL	0.6	5.4	-10	18.2	-37.5	28	0.142
TAPA	-99.6	6.4	-138	22.8	-52.3	48	0.015
VICT	-3.2	2.4	-27.8	8	-54.3	22.4	0.172

Table 2.1: Measured displacements, in millimeters. Errors are 2σ. N,E,V represents North, East, and Up; NE_Cor is cor relation between north and east measurements.

tions should be small compared to the coseismic offsets measured. The measured coseismic displacements are therefore not likely to be significantly contaminated by non-coseismic signals. A maximum displacement of 986±14 mm was measured at station CHAM, and a minimum of 39±15mm was measured at station SJDL (Table 2.1, Fig. 2.1). All stations show coseismic subsidence, with amplitude decreasing away from the epicentral region. The site CRIP is located on the coast at Manzanillo, near a continuously monitored tide gauge. Data from this gauge, when compared with tide gauge data from Acapulco and Puerto Vallarta, indicate 74 $\pm 10(2\sigma)$ mm of subsidence at Manzanillo between the time of the earthquake and 7 days later. The GPS-derived offset, measured 6 days after the event, shows 80±14 mm (2σ) of subsidence, in good agreement with the tide measurements.

The pattern of displacement is qualitatively consistent with a purely elastic response to thrust faulting along a shallowly dipping plane offshore the GPS network. The orientation of the displacement vectors varies smoothly across the network; the site furthest to the northwest (CHAC) has an SSW-oriented vector while at the southern end of the network (SJDL, VICT) the vectors are oriented west, and displacement of stations directly inland of the epicenter point SW, as is expected for a response uncontaminated by imbricate faulting or other local tectonic processes. The small

Station	Model Displacement and Residuals					
ID	N	Nres	E	Eres	V	Vres
AVAL	-75.2	3	-120.8	-3.9	-16.7	-21.1
AYUT	-144.6	-16.2	-99	-38	-13.4	-98
CEBO	-34.4	0.4	-45.4	-5.1	0.9	-5.9
CHAC	-103.1	3.3	-10.8	-14.8	-30.6	7.5
CHAM	-836.3	0.3	-457.3	-21.8	-253.9	44.9
CRIP	-392.8	0	-314.8	-0.4	-79	-1.3
GUAC	-95.4	-9.2	-57.1	-2.2	-3	-44.5
PURI	-417.2	-0.7	-308.2	33.6	-180.5	76.5
SJDL	-7.6	8.2	-24	14	-17.5	-20
TAPA	-92.2	-7.4	-106.9	-31.1	-9	-43.3
VICT	-8.2	5	-37.1	9.3	-12.4	-41.9

Table 2.2: Modelled displacements, in millimeters. Errors are 2σ. N,E,V represents North, East, and Up; NE_Cor is cor relation between north and east measurements.

offsets measured at coastal sites furthest from the epicenter show that the network bracketed the deformation field well; SJDL and CHAC have offsets of only 4% and 11% of the largest coastal displacement, measured at CHAM.

2.4 Inversion

To estimate the distribution of thrust-slip on the rupture plane we invert the data using singular value decomposition (SVD) after Larsen (1991) and Hudnut *et al.* (1996). We find that a uniform slip model cannot adequately fit the three large displacements at CHAM, PURI and CRIP without an excessively large seismic moment; using a smaller fault plane situated so as to best fit CHAM and PURI produces a very poor fit at CRIP. The SVD method, whose limitations we discuss below, inverts the three component GPS vectors (accounting for uncertainties) for slip along an *a priori* fault with a specified number of sub-faults. For the fault we use a single plane consistent with the Harvard CMT solution for this event as well as the fault geometry inferred for the region by Pardo and Suarez (1993) from local and teleseismic data.

The fault plane (Fig. 2.1, Fig. 2.2) has an along-strike length of 200 km, a down-dip width from the trench of 100 km, a dip of 16° and has 200 10x10 km sub-faults. We

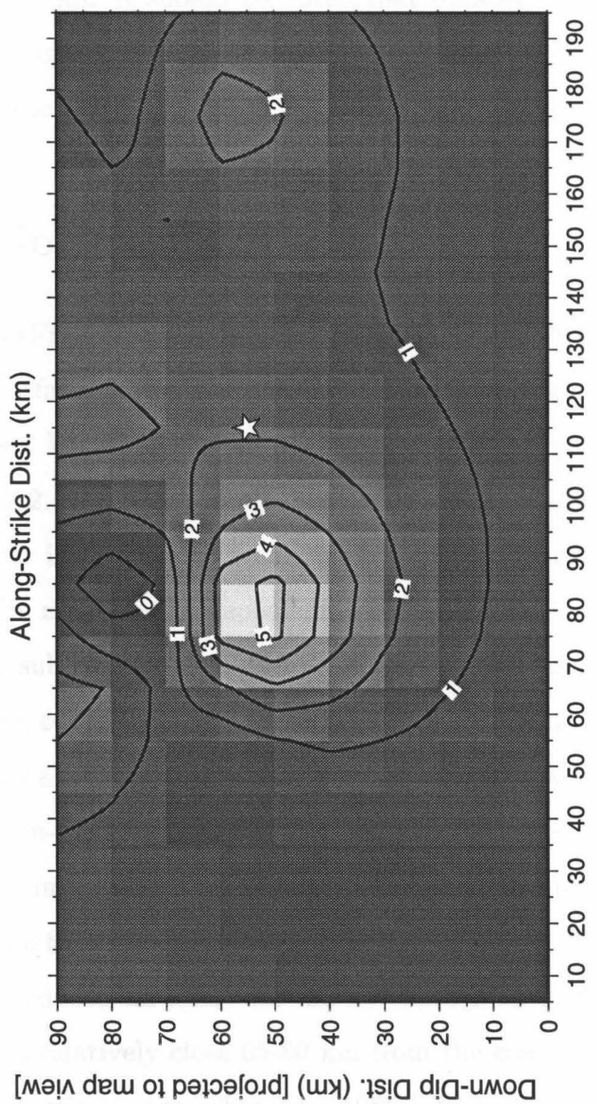

Figure 2.2: Distribution of slip on the Rivera plate thrust fault. Contours and shading indicate the thrust-slip amplitude (in meters). The model plane has 20 subfaults along-strike and 10 sub-faults down-dip, each 10 km by 10 km. The distribution indicates two distinct slip patches separated by 95 km, in agreement with seismic evidence for a multiple-source event. The star indicates the projected position of the Harvard CMT epicenter.

placed no constraints on the amount of slip at the edges and employed no smoothing outside of the averaging intrinsic to singular value decomposition; in this inversion there are 8 singular values. It should be noted that because stations CHAM, PURI and CRIP contain roughly 80% of the total offset measured in the network, these three stations dominate the inversion.

2.5 Discussion

The slip distribution (Fig. 2.2) indicates that nearly all of the slip occurred within the upper 18 km of the surface, with a maximum of 5 meters at 15 km depth and 2 meters of slip as shallow as 8 km. The displacements predicted from this slip distribution are shown in Table 2.2. The most robust aspect of the inversion is this lower depth limit of faulting; it is insensitive to small variations in either the dip, the area of the fault plane, or the number of independent sub-faults, and is primarily a result of the geometry of the subduction zone and its proximity to the coast. Qualitatively, the boundary between coseismic uplift and subsidence for slip along a shallow-dipping thrust fault delineates a trench-parallel axis, or hingeline, whose position lies near the surface-projected down-dip terminus of fault rupture. To match the coastal vertical subsidence measured in Jalisco, the majority of slip on the fault must be located sufficiently far offshore that the deformation hingeline also lies offshore, i.e., such that only subsidence is produced on land. As the northern Middle America trench near Jalisco is located at a relatively close 65-80 km from the coast, or half that of Chile and other major subduction zones [Thatcher (1984)], fault slip located sufficiently far offshore to produce the measured subsidence is therefore constrained to lie within the upper reaches of the fault. Tests of the *a priori* fault parameters cause only minor deviations from the slip distribution presented here, and in particular, extending the fault plane further to the southeast produced negligible slip there.

The SVD inversion also shows two distinct slip regions, one offshore of station CHAM and another at the same depth but 95 km to the southeast, offshore of CRIP. Although these two slip concentrations are consistent with seismic interpretations of

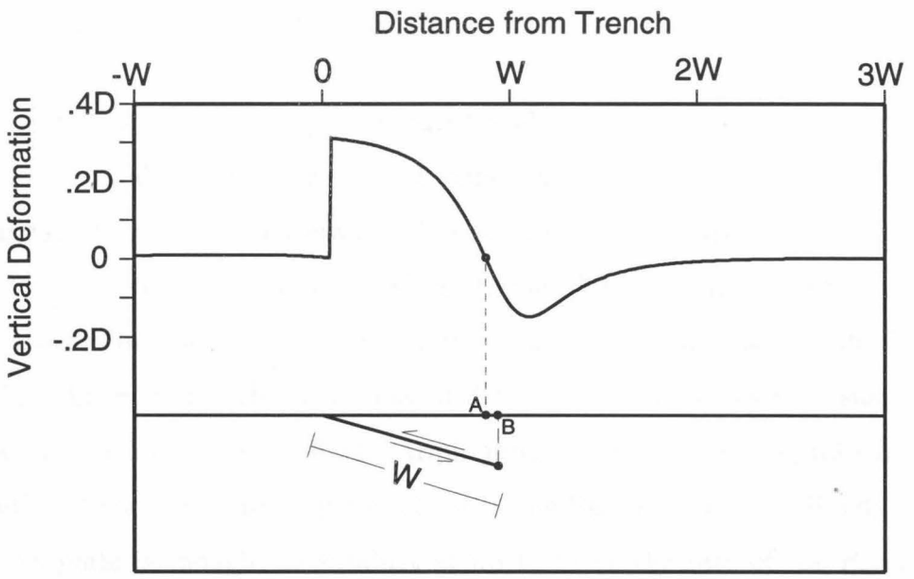

Figure 2.3: Vertical deformation profile for a uniform-slip, shallow thrust fault of width W, dipping 18° and slip D. The boundary between coseismic uplift and subsidence delineates a trench-parallel axis, or hingeline (A), whose position lies near the surface projection of the down-dip terminus of fault rupture (B). Calculated from Okada (1993).

a 100 km rupture length (Kikuchi (1995)) and a major sub-event separated in time from the mainshock by approximately 35 seconds[2] (implying a slip-patch separation distance of 90-115 km for a rupture velocity between 2.5 to 3 km/s), it should be noted that the inversion cannot uniquely resolve the along-strike shallow slip. The slip patch directly offshore CRIP reflects the fact that there are no stations near CRIP which could better constrain the inversion. Furthermore, slip in the uppermost regions of the fault is poorly constrained due to a lack of GPS stations offshore. The SVD inversion therefore gives a reliable lower depth limit to faulting and attempts to resolve the first order slip distribution in the shallow portions of the fault; however, additional data is needed for increased resolution.

[2]NEIC

2.5.1 Subduction of the Rivera Plate

The slip distribution indicates that the earthquake ruptured the Rivera-North American boundary and not the Cocos-North America boundary, although the nature of the boundary between the Rivera and Cocos plates at the surface has proven enigmatic. Recent seafloor observations suggest that the boundary is not necesarily a discrete feature but rather a zone of deformation between the East Pacific Rise and the Middle America Trench. This zone of deformation comprises extensional structures east of the Rivera-Cocos-Pacific triple junction (the El Gordo graben) (Figure 2.1, inset) and compressional features closer to the East Pacific Rise (Bandy (1992)). The Cocos plate is thought to subduct at up to twice the rate of the Rivera plate (DeMets and Stein (1990); Kostoglodov and Bandy (1995)), but more recent evidence indicates oblique convergence across the Cocos-Rivera boundary amounting to nearly 20 mm/yr directed N10E (Wilson and DeMets (1997)).

The small, westward displacements at stations located near the Cocos-Rivera-North America triple junction (VICT, SJDL) make it unlikely that any significant slip occurred southeast of the El Gordo graben along the northern-most part of the Cocos subduction zone. If significant thrust slip had occurred near or southeast of the triple junction, the displacement measured at SJDL and VICT would contain a SW-directed extensional component and the measured vectors would therefore point more southernly. Oriented almost due west, they indicate that no significant subduction-related thrust faulting could have occurred either nearby or southeast of the Rivera-Cocos boundary.

The difficulty in identifying a Rivera-Cocos boundary precludes an absolute determination on the basis of geodetic information alone of which plate interface with North America broke during this event. The CMT epicentral locations suggest the possibility that the earthquake ruptured across the Rivera-Cocos boundary within the trench. The Caltech and NEIC locations (USGS (1995)) lie in the vicinity of the Cocos-Rivera-North America triple junction, while the Harvard CMT is located 80 km to the northwest. Additional evidence of Rivera plate subduction was inferred

by Zobin (1997) from a teleseismic analysis of the rupture history of the event. The rupture propagation inferred from his study begins near the boundary between the Rivera and Cocos plates and propagates mainly along the Rivera-North American plate boundary. In the model, the high-slip asperities are additionally located along the Rivera-North American plate boundary.

2.5.2 Tsunami Constraints

The Jalisco earthquake produced a large tsunami for its magnitude, with tide-gauge amplitudes measured at Manzanillo, Cabo San Lucas and Kahului, Hawaii of 2, 0.5 and 0.12 meters, respectively (USGS (1995)). While debate exists over the exact dependence of tsunami generation on depth of slip, the theory that shallower faulting will produce a bigger tsunami is intuitive and generally held (Satake (1995)). In particular, Okal (1988) has shown that earthquakes in which as little as 10% of the total moment release takes place in sediments can produce a tsunami up to a factor of 10 greater than their moment would suggest. For the tsunami generated by the 1992 Nicaragua subduction earthquake (Mw=7.6-7.7) (Satake (1995)) found that the source model derived from seismic data, which mapped slip into the upper 30 km of the fault, produced amplitudes and modeled run-up heights which were small compared to the actual tsunami. Instead Satake (1994) found that a source model in which an average of 3 meters of slip occurred in the upper 10 km produced a much larger tsunami which fit the data better. Although the wave run-up heights have not yet been modeled for the source we derive, the relatively large tsunami generated by the Jalisco event would appear to provide, at least qualitatively, independent evidence of shallow faulting.

2.5.3 Sediment Rheology

The slip distribution agrees with previous studies showing a shallow seismogenic zone in the Middle America Trench extending only to a depth of 25±5 km; this depth is roughly half of that observed in most subduction zones of the world and appears to

control the maximum earthquake size here (Suarez and Sanchez (1996)). The narrow locked portion of the faults could be controlled in part by sediment supply. The Jalisco-Colima coast has no large river systems through which a high continental sediment flux can reach the trench, and there is little to no accretionary prism offshore this subduction zone relative to a global average and therefore presumably relatively little subduction of hydrated sediments compared to other convergent margins with deeper seismogenic zones. Danobeitia *et al.* (1997) have presented multichannel seismic data which indicate roughly 1 Km of sediment; in comparison, the thicknesses offshore Cascadia are greater than 3 Km. Faulting mechanisms tying brittle failure in subduction zones to sediment rheology and supply [Marone and Scholz (1988)] predict a shallower seismic front in subduction zones which receive less sediment.

Sediment rheology provides a consistent explanation for the up-dip limit of seismicity offshore Jalisco but the shallow down-dip limit is more likely to be controlled by temperature. The temperature of the down-going slab has been suggested by several studies to be the primary controlling factor on the down-dip extent of the locked portion of subduction zones (Tichelar and Ruff (1993); Hyndman and Wang (1995a)). As the down-going slab offshore Jalisco is relatively thin, the temperature-controlled transition from velocity-weakening to velocity-strengthening in the fault constitutive properties within hydrothermal environments can occur at shallower depths in this subduction zone compared to the global average.

2.5.4 A Hazards Model for Cascadia?

As one of the fundamental parameters controlling both the potential moment release and tsunami excitation in subduction zone earthquakes is the depth range over which faulting can occur, the implications of the demonstration here of very shallow rupture indicates a potentially systematic underestimation of seismic hazards associated with Cascadia. The general absence of shallow earthquake nucleation in subduction zones (Byrne *et al.* (1988)) does not preclude rupture from propagating into this region from below (Chen *et al.* (1982)). This can significantly increase the seismogenic

potential of subduction zones over an estimation not including shallow faulting, as this earthquake illustrates. Despite there having been little historical shallow (< 10 km) seismicity located in the northern Middle America Trench (Chen *et al.* (1982); Pardo and Suarez (1993)), based on the slip inversion 18% of the total moment of the Jalisco earthquake came from slip above 10 km. Although most subduction zones exhibit shallow aseismicity, this example merely illustrates that the accretionary prism should not be discounted out of hand in estimations of seismogenic potential.

We suggest that the larger pattern of coseismic displacement reported here may serve as a model for Cascadia subduction earthquakes. A host of recent studies have discussed the geologic evidence of coseismic subsidence in Cascadia as well as current uplift and E-W shortening (Hyndman and Wang (1995b)). Comparisons between Jalisco and Cascadia have been made in terms of the subducted plate age and convergence rate, dip angle and the relatively narrow locked portions of both subduction zones (Heaton and Kanamori (1984); Scholz (1989)). Although not applicable in fine detail, the overall demonstration of regional subsidence and mainly elastic crustal response validates ground displacement models proposed for Cascadia.

2.6 Acknowledgments

The data were collected with the indispensable help of Dawnika Blatter, Phillip Bonstin, Jaime Dominguez, and Gerardo Perez-Ramos. The data were inverted using GINV and DISL programs written by Shawn Larsen. We thank the GIPSY-OASIS development team at JPL for GPS data-processing help. Supported by NSF grant EAR-9527810. California Institute of Technology, Seismological Laboratory contribution #5795.

Chapter 3 The Demonstration and Mechanics of Rapid, Postseismic Deformation in Subduction Zones

3.1 Abstract

We discuss Global Positioning System derived time series from three large subduction earthquakes of which two show significant, rapid, post-seismic ground deformation most easily explained as afterslip along the co-seismic fault plane. The data address the 1995 Mw 8.0 event offshore Jalisco, Mexico, the 1994 Mw 7.6 Sanriku-Oki event recorded on the permanent Japanese GPS array, and the 1996 Mw 8.1 Antofagasta event offshore northern Chile. Following the Jalisco and Sanriku earthquakes, a significant portion of total ground deformation associated with the event occurred during the two weeks following the mainshock. In the Jalisco data we can demonstrate that the after-slip is located predominantly downdip of the co-seismic rupture concentration, suggesting that the earthquake was succeeded by a slowly propagating rupture front migrating down the Benioff zone from the co-seismic rupture patch. Together these data sets represent the three best continuous geodetic observations of great subduction earthquakes, and the fact that two of the three events showed rapid afterslip suggests that it may be common and increasingly observed with the deployment of continuous deformation measurements in convergent plate margins. The implications of possibly ubiquitous significant afterslip bear on global estimations of seismic coupling (Kanamori (1977)) and seismogenic potential and natural hazards associated with active subduction zones. Possible mechanisms of afterslip are discussed within the context of known thermodynamic properties of subducted sediments at depth.

3.2 Introduction

Transient aseismic deformation subsequent to large earthquakes is well documented and has been shown to occur along both interplate and intraplate faults with timescales ranging from several months to hundreds of years (Heki *et al.* (1997); Smith and Wyss (1968); Thatcher and Rundle (1984); Bucknam *et al.* (1978); Savage and Plafker (1991)). At convergent plate boundaries, intermittent leveling campaigns first demonstrated continued surface deformation following subduction earthquakes (early results summarized in Kanamori (1973)), but the short-term time distribution of such afterslip was unavailable due to the long intervals between geodetic observations. Furthermore, the time interval between a major earthquake and when nearfield geodetic networks could be re-measured disallowed the identification of any rapid post-seismic deformation which might have occurred in the days following the event. Any such slip would instead wrongly be attributed to co-seismic displacement, either augmenting or decreasing the net amount measured. Recently, however, continuous geodesy at convergent margins has begun to show the existence of rapid, aseismic creep within seismogenic subduction zones. For example, continuous strain-dilatometer and GPS measurements along the Sanriku subduction zone offshore northern Honshu, Japan, has documented variable-rate faulting occurring over timescales ranging from seconds (Sato *et al.* (1996)) to days (Kawasaki *et al.* (1995)) to nearly a year (Heki and Tamura (1997)) within the same general subduction zone. With the ongoing deployment of geodetic instruments measuring continuous three-dimensional deformation data at many convergent margins, it has now become feasible to recognize the temporal and spatial distribution of afterslip, and to determine whether it is in fact a generally occurring phenomenon previously hidden by infrequent measurements, or rather one localized to certain subduction zones with specific characteristics.

An outstanding issue concerning convergent margins globally is the discrepancy between convergence rates, as determined from tectonic plate reconstructions and satellite geodesy, and the amount of convergent slip derived from seismic analysis of great ($> M_w 8$) subduction earthquakes. For many subduction zones, only a small

fraction of the total convergence appears to be expressed seismically, i.e., the "interplate seismic coupling" $<$ 1 (Kanamori (1977)). For example, along the active Japan and Kurile trenches, the interplate seismic coupling is only about 30% between the North American and Pacific plates, and in the Sanriku region it is closer to 20% (Pacheco *et al.* (1993)). Presumably, the remainder of the convergence occurs in the form of either continuous creep or slow, seismically undetectable earthquakes. It is therefore of great interest to resolve how this convergence is distributed in time, and to identify whether a significant portion of the 'unseen' interplate slip actually occurs prior to or following large seismogenic subduction earthquakes.

Also of fundamental interest in understanding the mechanical properties of subduction zones is to determine whether the observed creep is additional slip occurring along the co-seismic rupture patch, or whether it is slip elsewhere along the fault plane, either by migration away from the co-seismic rupture patch or triggered faulting elsewhere on the plane. Here the term 'fault plane' refers to the idealized two-dimensional surface containing the co-seismic rupture patch. Earthquake prediction using continuous deformation monitoring of the hanging wall above active convergence zones is based in part on the possibility of precursory deformation preceding seismic rupture. The demonstration of rapid slip migration succeeding a mainshock event is therefore relevant to these endeavors.

The GPS time series we discuss in this paper show the geodetic deformation produced by three large earthquakes which occurred in three subduction zones with very different convergence rates, plate ages, and sediment loads. The earthquakes are the 1994 M_w 7.5 Sanriku-Oki event, the 1995 Mw 8.0 Jalisco earthquake, and the 1995 Mw 8.1 Antofagasta event. In interpreting these data we follow Savage (1983) and Marone *et al.* (1991) by assuming all post-seismic deformation is caused by continued slip somewhere along the fault plane rather than independent processes such as asthenospheric relaxation. Unlike previous reports of transient post-seismic deformation which occurred over timescales of many months to years, which could be the result of non-fault related processes, here we discuss deformation occurring on timescales of days, which has no plausible cause except rapid aseismic fault creep. The data show

co-seismic displacements as well as rapid deformation caused by afterslip during the weeks following the mainshock, and in the Jalisco event we argue that the majority of the afterslip occurred down dip from the co-seismic rupture concentration. For this event deformation measured during the two week interval following the mainshock amounts to approximately 70% of that measured during the mainshock, while the Sanriku data show about 30%. Taken together, these three data sets constitute the most complete continuous deformation measurements of subduction earthquakes collected to date, and raise the possibility that rapid afterslip and affiliated ground deformation is the typical behavior of certain types of subduction zones which are systematically different in how they accommodate plate convergence. With the ever increasing dense arrays of continuous GPS monitoring such as those already established in Japan, Chile, and elsewhere, the test of time of this conjecture will be soon forthcoming. The answer will have important ramifications in evaluating the global seismic coupling and moment release, and evaluation of natural hazards associated with convergent margins.

3.3 Data

The GPS data for all three events were recorded with dual frequency P code receivers and processed using the GIPSY-OASIS II software (Lichten and Border, 1987) and ephemerides and satellite clock corrections provided by the Jet Propulsion Laboratory for the International Geodynamics Service (Zumberge et al., 1995). In this process, station coordinates, carrier phase biases, zenith troposphere delays, and station clocks were estimated using 24 hour data arcs. Phase biases were estimated as real valued parameters and the double-differenced biases were fixed to their dual frequency integer equivalents using the method of Blewitt (1993). In all cases more than 90% of the double-differenced phase biases were resolved. Troposphere delays were estimated as random walk processes at each station with noise added at a rate of 1 cm/hr, and station clocks were estimated as white noise processes reset at every 30 s data epoch. Depending on the data set, station coordinates were processed using either 75 minute

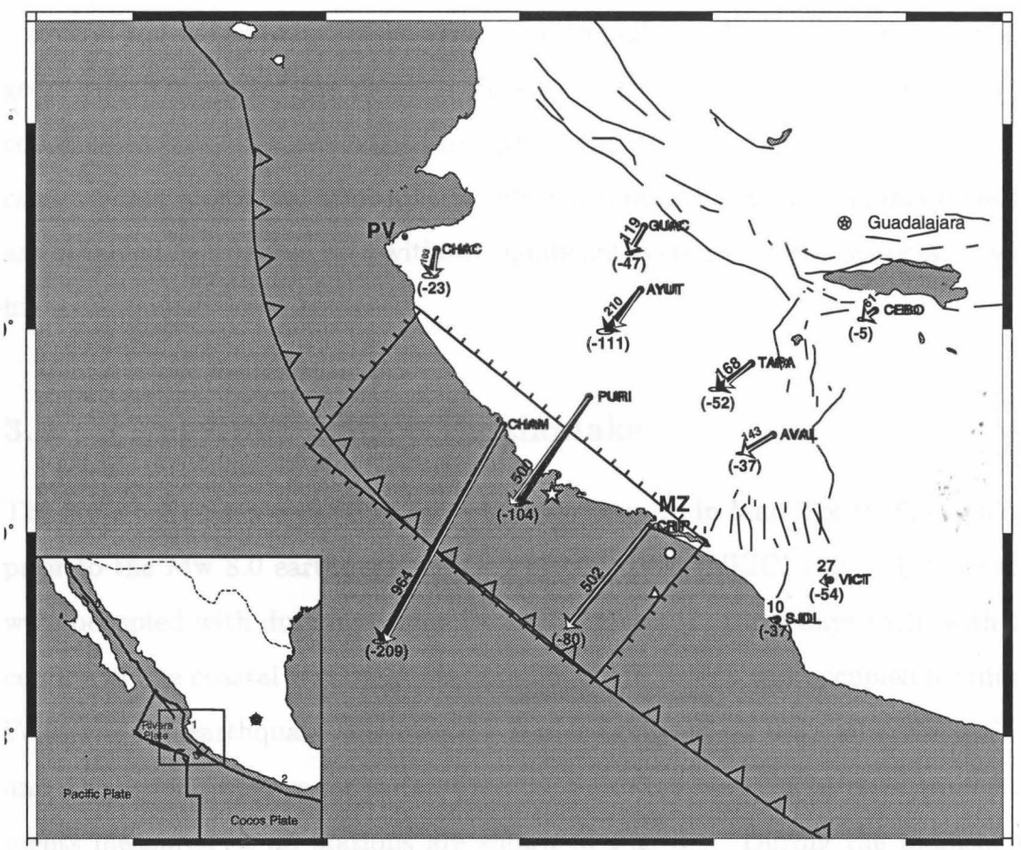

Figure 3.1: Coseismic displacements for the Oct., 1995, Rivera plate subduction earthquake (Mw=8.0). GPS measurements are shown as solid black vectors, with amount (in millimeters) of horizontal offset written along the vector and vertical offset in parentheses at the vector tip. GPS vectors at stations SJDL and VICT point west. Ellipses represent 2D 95% confidence intervals. Thin white vectors are modeled from slip distribution in Fig. 3. Gridded rectangle is the surface projected model fault plane, and the Harvard and Caltech centroids and the NEIC epicenter are indicated by the star, circle and triangle, respectively. Manzanillo Bay and Puerto Vallarta are shown abbreviated with MZ and PV, respectively. Inset. The Rivera and Cocos plate subduction zones. Numbers 1 and 2 show locations of Puerto Vallarta and Acapulco tide gauges, repectively.

(Sanriku), six hour (Jalisco), and two hour (Antofagasta) stochastic coordinate resets. Position errors for high rate solutions can be dominated by higher frequency, GPS signal multi-path and atmospheric delays, and by weak geometric strength of the observations for estimating station positions and carrier phase biases. As the length of the data arc increases, errors due to multi-path are averaged down and the geometric strength of the solution increases. By applying stochastic resets to the coordinates only, the geometric strength of the 24 hour data arc for estimating the carrier phase biases and atmospheric delays is retained and station position estimates are obtained at a higher rate without significant systematic error associated with the higher frequency error sources.

3.3.1 The 1995 Jalisco Earthquake

The Jalisco GPS network (Fig. 3.1) was first occupied in March of 1995, seven months prior to the Mw 8.0 earthquake of October 09, 1995 (NEIC, 1995). Fifteen stations were occupied with dual frequency P-code receivers for three days each, with the exception of one coastal station at Manzanillo, CRIP, which was occupied for nine days. Following the earthquake, the network was re-occupied six days after the mainshock, and 11 stations were re-measured over the following week. The co-seismic displacements measured at all stations are shown in Fig. 3.1. During the mainshock, the entire coastal region showed SW displacement and subsidence, which constrains most of the faulting to have occurred offshore and at very shallow depths (Melbourne *et al.* (1997)).

Estimation of Rapid Post-Seismic Slip

The motion of the station CRIP, in the city of Manzanillo, measured during the two weeks following the event is discussed in the present study. Because of logistical delays, six days passed before we were able to re-occupy the network. Station CRIP was measured continuously over a 9 day period from day 7 to day 16 following the mainshock. Fortunately, a continuously monitored tide gauge station was located nearby

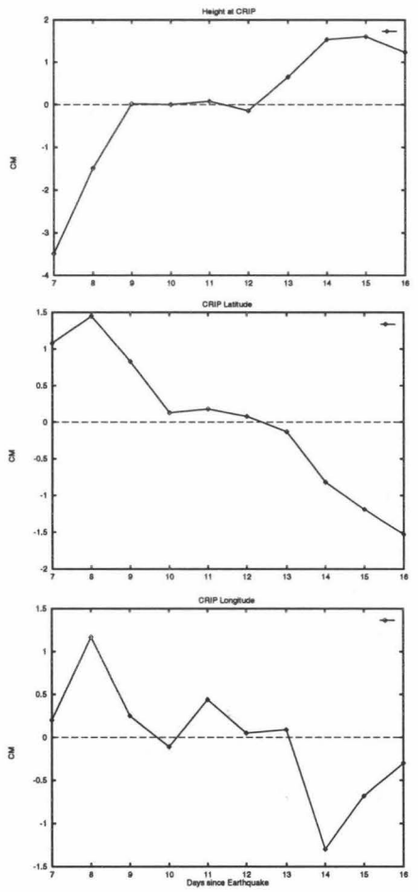

Figure 3.2: Daily solutions at CRIP showng rapid postseismic displacements at Jalisco.

(also within Manzanillo Bay) and we use data from this gauge to assess the vertical motion during the 6 days not covered by the GPS data. During the measurement time following the earthquake, there were no significant aftershocks with magnitudes larger than Mw=5.6 (NEIC, 1995) and so the post-seismic deformation cannot be attributed to aftershocks.

Figure 3.2 shows daily solutions of CRIP during the post-earthquake occupation period, while Figure 3.3 shows 6 hour solutions of the North, East and vertical components of motion during the 9 day time series measured at CRIP between 7 and 16 days after the earthquake. The 24 hour periodicity in the time series is probably multi-pathing of the GPS signals, but an additional source of error is caused by earth

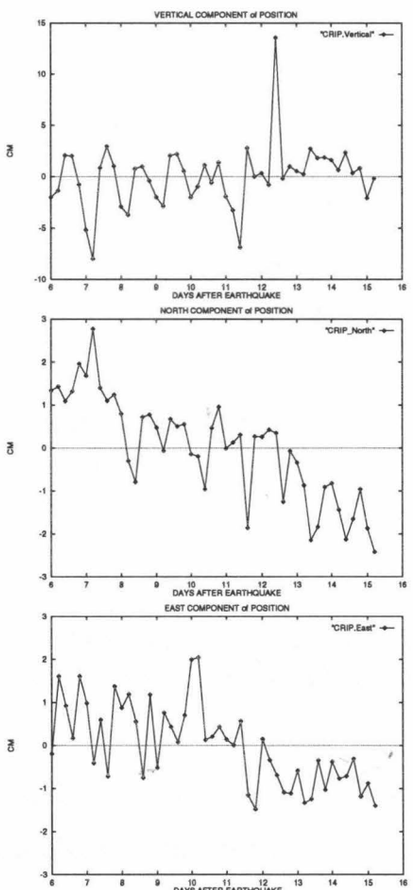

Figure 3.3: Rapid Postseismic displacements at Jalisco. These are 6 hour solutions.

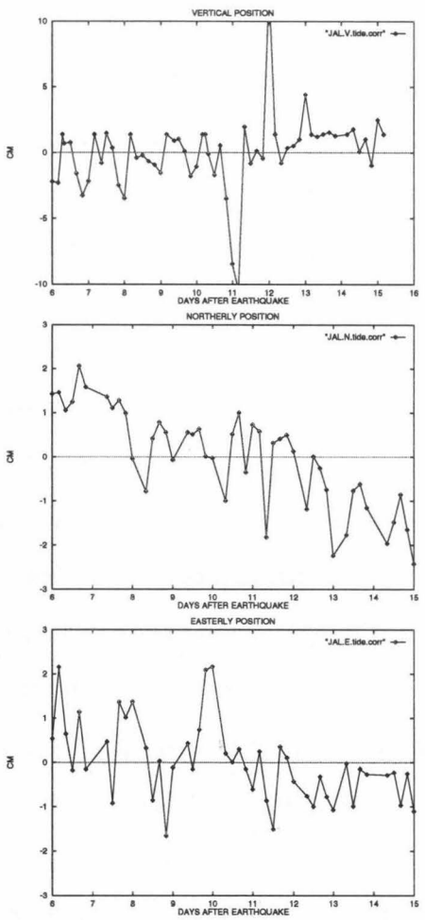

Figure 3.4: Rapid Postseismic displacements at Jalisco. These are 6 hour solutions with lithospheric tidal loading effects (Scherneck (1991)) modelled and removed.

tidal displacements, which can be accounted for to a certain extent. Figure 3.4 shows the same time series after an observational model for earth tide displacements is removed. This model incorporates effects from anelasticity, ellipsoidal figure, and fluid core resonances and was developed in application to Very Long Baseline Interferometry (Scherneck (1991)). The algorithm used to apply the corrections is part of the standard distribution of the GIPSY-OASIS software package and is commonly used for coastal sites employing sub-daily solutions.

As can be seen from both the corrected and uncorrected time series, the station CRIP continued to move during the GPS measurement period. As determined from a straight line regression of the corrected time series, CRIP moved an additional 4.2±1

cm southwest at an azimuth of S26W and rebounded 4.5 $\pm$1 cm up vertically. In comparison, as measured with GPS, the station co-seismically moved 50 cm S38W and subsided 8.4$\pm$1 cm. From these measurements alone, the 3-D post-seismic motion during this time period at CRIP is roughly 12% that of the co-seismic, as measured between the seven months prior to the earthquake and 6 days afterwards. This is by far a minimum estimation of the total post-seismic deformation, of course, because the postseismic GPS observations do not include any displacements which might have occurred during the first 6 days after the earthquake. In light of current ideas about afterslip decay (eg, Marone *et al.* (1991)), most of the post-seismic faulting is expected to have taken place within a few days after the earthquake, during the time when the GPS data are absent. To try to quantify the amount of deformation which occurred during this period, we can take advantage of the continuous sea level height measurements which were made during this week.

The National Autonomous University of Mexico (UNAM) operates three continuous tide gauges, one of which is very close to CRIP in Manzanillo harbor, and the other two of which are at Puerto Vallarta and Acapulco (Figure 3.1. Analysis of the tide gauge data from Manzanillo alone indicated that the co-seismic subsidence during the earthquake amounted to 14 cm (Ortiz *et al.* (1996)). Figure 3.5 shows the raw, unfiltered time series data averaged over six minutes. There is a transient which records the multiple reverberations in the bay caused by the tsunami induced by the earthquake, followed by what appears to be a clear step in the maximum tidal height. Figure 3.6 shows just the data from 5 days before to 5 days after event, and with the transient removed. By simply assuming that the daily tidal maximum stayed roughly constant across the earthquake, then any net offset of the tidal maximum is a result of co-seismic subsidence, and by evaluating the difference we find 13 cm of co-seismic offset, which agrees with the filtering analysis of Ortiz *et al.* (1996). The GPS data indicate 8.4 ± 1 cm of subsidence as measured 6 days after the earthquake. Since the GPS difference is based on the measurement made in March, 1995 and that made 6 days after the event, and in light of the indisputable movement of the station between day 7 and day 16 after the event, we interpret the discrepancy with the tide gauge

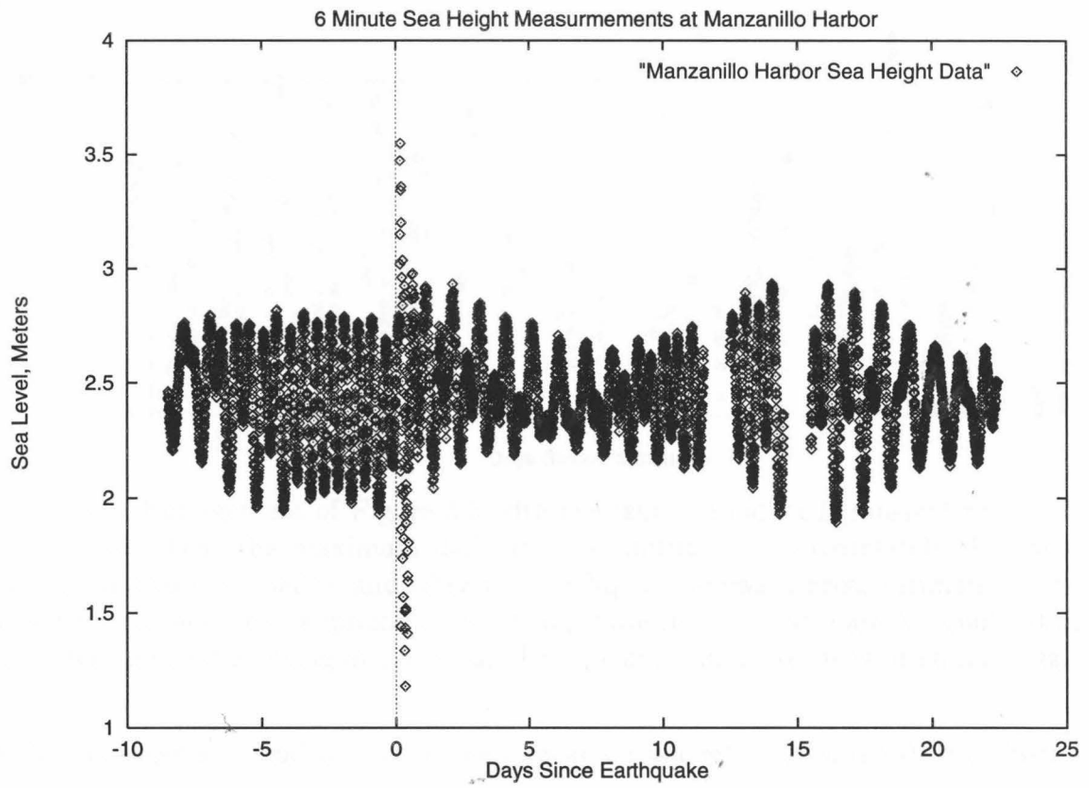

Figure 3.5: Six minute sea height level measurements from the tide gauge operated in Manzanillo Harbor by the National Autonomous University of Mexico. The diurnal cycle and monthly cycles are clearly evident, but the tsunamigenic transient is clearly evident following the earthquake. Following the event, a step in the maximum daily tidal height level is evident. This step is enlarged and quantified in Figure 3.6. (Unpublished data, courtesy O. Sanchez.)

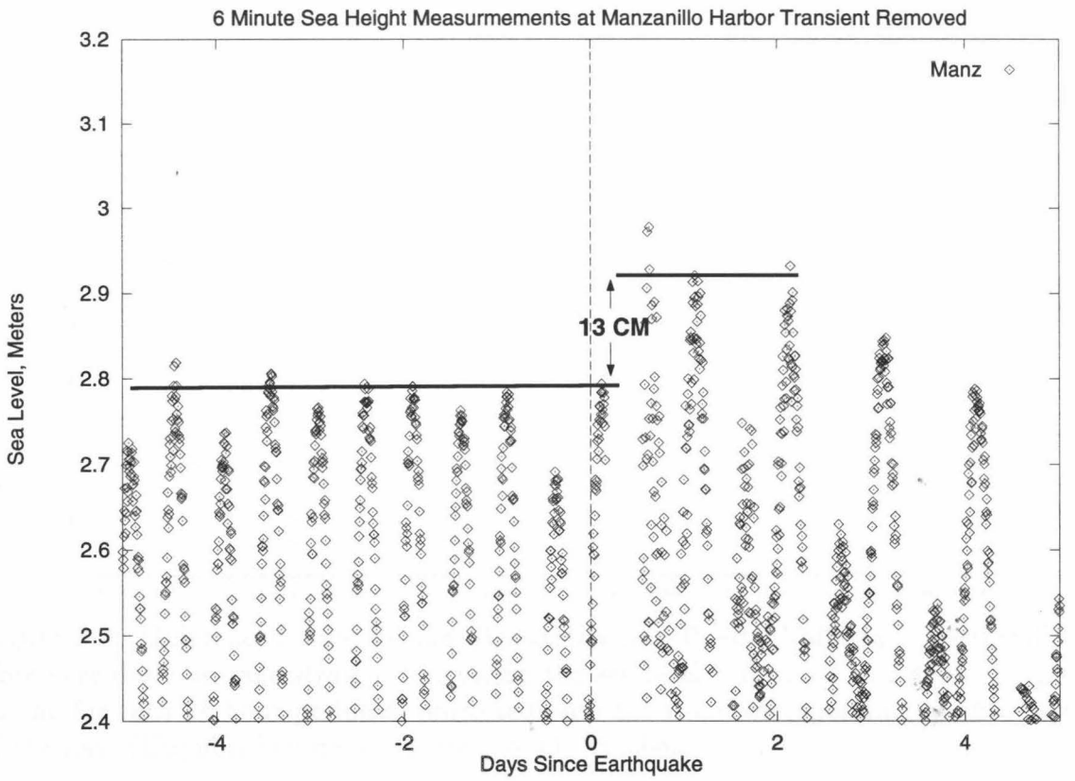

Figure 3.6: Enlargement of Figure 3.5 with the tsunami-induced transient removed. By assuming that the maximum daily tidal amplitude is approximately the same during the two days before and after the earthquake allows a gross estimate of the co-seismic subsidence of approximately 13 cm. Note that this estimate does not entail any filtering or differencing of the data. (Unpublished data, courtesy of O. Sanchez.)

derived co-seismic subsidence to be due to post-seismic rebound of the station during the first six days following the event.

To quantify both the co-seismic subsidence and any rebound missed by the GPS measurements, we use the two additional tide gauge stations which were recording during the earthquake but located sufficiently far away so as to be unaffected by the near field seismic deformation. The station at Puerto Vallarta is located 200 Km to the northwest, and the Acapulco gauge lies 400 Km to the southeast. Because the lunar and solar ocean tides along the central coast of western Mexico are similar, time series from these stations can be differenced with the time series from the Manzanillo tide gauge in order to assess the co- and post-seismic vertical deformation at Manzanillo.

Figures 3.7 and 3.8 are these differenced time series of the daily averaged tidal

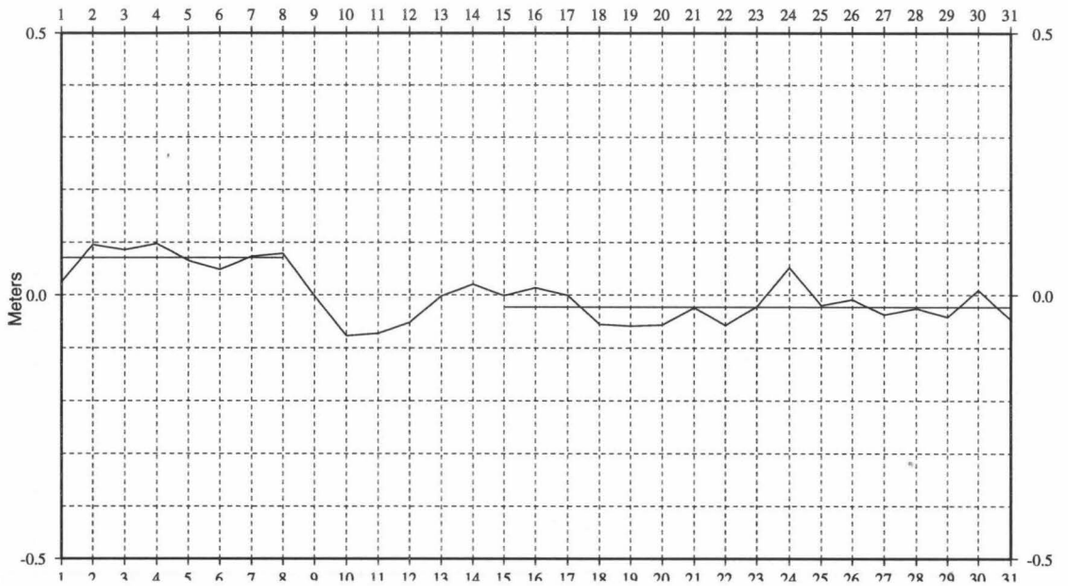

Figure 3.7: Differenced Tide Gauge Measurements: Puerto Vallarta - Manzanillo. These are daily average straight line connected sea level heights. The average height during for each 24 hour period is projected onto the time corresponding to the start of the day. (Unpublished data, courtesy of O. Sanchez.)

height (Sanchez, unpublished data). Figure 3.7 shows the level at Manzanillo subtracted from the level at Puerto Vallarta, and Figure 3.8 shows Manzanillo subtracted from Acapulco. Evident in both of the differenced tidal plots is the large deviation in the differenced tidal level around the time of the earthquake and the days immediately following it. As the gross trends during this time on both plots are similar, the deviation clearly comes from the Manzanillo tide data. Because these are daily averaged sea level heights and do not include error estimates, some care must be used when interpreting them. Looking first at Figure 3.8, during the four days prior to the earthquake, the differenced sea level height is stable to within roughly $\pm$ two centimeters. On October 9, the day of the earthquake, the daily averaged differenced tidal level is approximately 10 cm lower than on the 8th. Since these are daily (Eastern Standard Time) averaged levels, and because the earthquake occurred approximately at 8:30 am EST, the daily averaged tidal height at Manzanillo for the 9th will reflect less than the total co-seismic jump due to the fact that roughly a third of the data were measured before the earthquake. The daily average on October 10 should

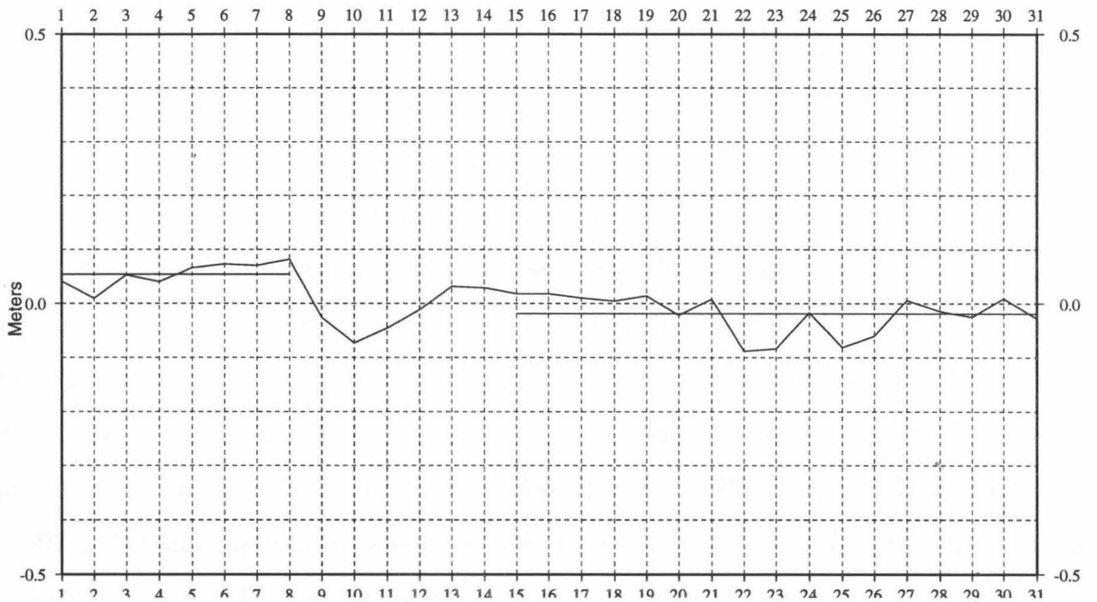

Figure 3.8: Differenced Tide Gauge Measurements: Acapulco - Manzanillo. These are daily average straight line connected sea level heights. The average height during for each 24 hour period is projected onto the time corresponding to the start of the day. (Unpublished data, courtesy of O. Sanchez.)

therefore reflect more truly the co-seismic jump, albeit contaminated by whatever post-seismic deformation occurred during the last half of October 9 and 10. From both Figures 3.7 and 3.8 the co-seismic vertical subsidence between the 8th and the 10th appears to be approximately 15 cm. Although there are no calculated errors, this is in good agreement with the other two estimates of net subsidence, the work of Ortiz *et al.* (1996), who derived the 14 cm of co-seismic displacement by filtering the Manzanillo tide data alone without differencing it, and from the measured net offset in the daily maximum tidal height, as shown in Figure 3.6. Furthermore, the measured difference in the sea-level height between prior to the event and six days after it is roughly 8 cm (Figure 3.7) and 6 cm (Figure 3.8), which is close to the GPS estimate of 8.4 ± 1 cm as the net subsidence during this time period. This agreement is encouraging and attests to the validity of differencing the time series in order to remove the dominant tidal signals. This allows us to examine the six days following the earthquake in order to quantify any post-seismic deformation.

The most striking aspect of both differenced time series is the rapid and significant upward rebound of the Manzanillo station during the three days following the event. Between October 10 and 13 Manzanillo appears to uplift 10 cm as inferred from Figure 3.8, and 8 cm from Figure 3.7. The magnitude of this rebound is well above a conservative estimation of the uncertainty of the tidal level, and for the purposes of identifying a best estimate of the post-seismic deformation by using the tide gauge and GPS data, we assume the following: 1) inter-seismic strain during the six months prior to the event is negligible; 2) the immediate co-seismic subsidence of Manzanillo was 14 cm (Ortiz *et al.* (1996)); and 3) the net subsidence between prior to the event and day 6 following it was 8.4 cm, as inferred from the GPS analysis (Melbourne *et al.* (1997)). Within these constraints, we infer that the net co-seismic subsidence during the earthquake of 14 cm was followed by 5.6 cm of uplift between day 0 and day 6 after the event, followed by 4.5 cm of additional uplift between day 6 and day 15 after the event. By simply treating vertical deformation as a proxy for total strain energy released, these numbers suggest that the net amount of post-seismic strain energy released in the 15 days following the earthquake was equal to 72% of the co-seismic strain energy released. However, taking into account an estimation of the different locations of co- and post-seismic faulting modifies this estimation to 40%. In any case, since this amount of vertical deformation is based largely on two compatible interpretations of the tide data which lack error estimates, this figure should be considered a rough estimate of the upper limit of rapid post-seismic deformation measured. It is nonetheless a highly significant portion of the total moment released in the subduction zone and would not be included in purely seismic considerations of total slip.

3.3.2 1994 Sanriku-Hakura-Oki

While other aspects of this GPS data for this earthquake have been recently discussed elsewhere in conjunction with extensiometer data (Heki *et al.* (1997); Heki and Tamura (1997)), we include a subset of that data set in the present discussion

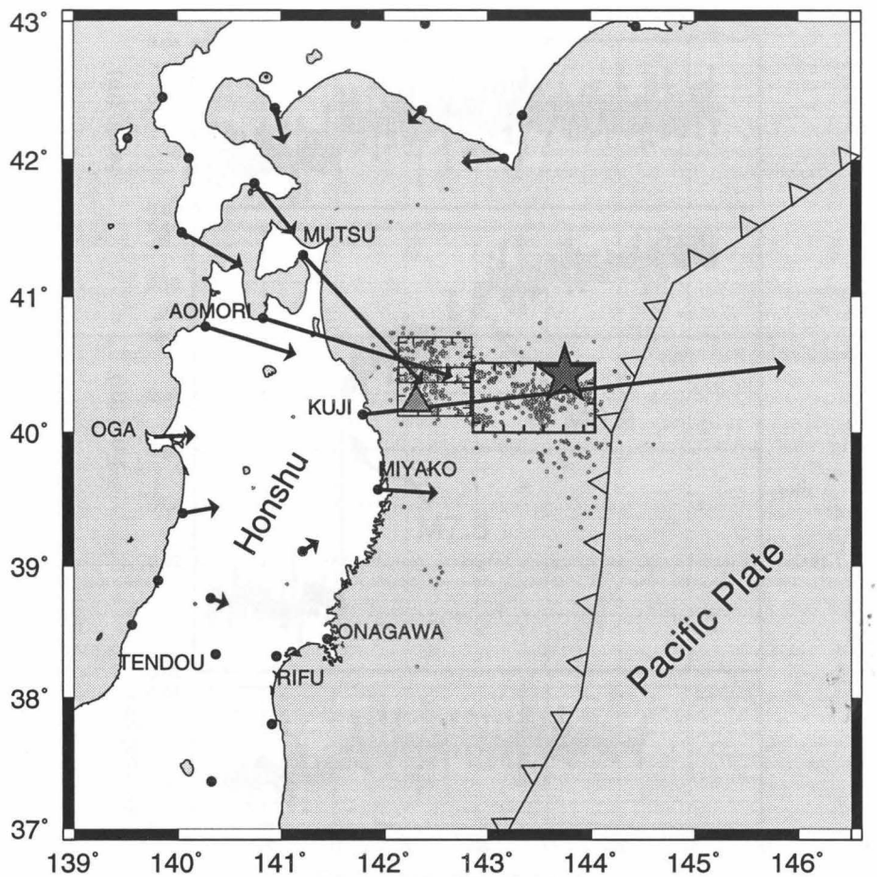

Figure 3.9: 1994 Co-seismic Displacements at Sanriku-Oki. F. Webb, unpublished data (Modified from Heki *et al.* (1997)).

because the measurements are of high quality and useful in illustrating the spectrum of post-seismic deformation rates observed to date with continuous GPS along subduction zones. The 1994 Sanriku-Oki event was a typical interplate thrust event and exhibited very shallow faulting ($< 25Km$, Nishimura *et al.* (1996)) along the west-dipping plate interface east of Northeastern Honshu. Delineation of the co-seismic fault plane and rupture region was based on GPS, aftershock, and broadband seismic data (Sato *et al.* (1996); Nishimura *et al.* (1996); Tsuji *et al.* (1995)).

The GPS station KUJI was located closest to the co-seismic rupture plane (Fig. 3.9) and shows the greatest deformation, with a co-seismic offset approaching 10 cm. Time series of 75 min positions showing the north, east, and up displacements for the 10

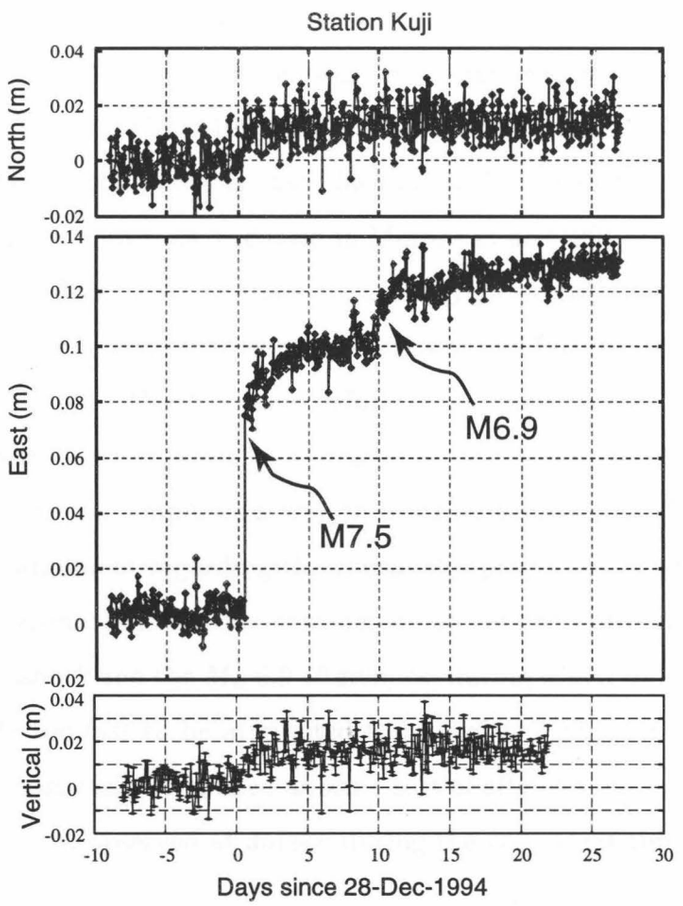

Figure 3.10: Rapid Postseismic displacements at Sanriku. The decay between the time of the M_w 7.5 earthquake and the aftershock 10 days later is the subject of this paper. (F. Webb, unpublished data.)

days before and 20 days after the December 28 event are shown in Figure 3.10.

Looking only at the East component, which has by far the highest signal to noise ratio, the mainshock faulting produced approximately 6.7 cm of offset at this station. Over the following nine days up until the time of the M 6.9 aftershock, an additional 2.25 cm of offset was measured, indicating an additional surface deformation equivalent to nearly 30% of that of the co-seismic. Heki et al. (1997a,b) modeled the deformation with an afterslip formulation in which the slip is proportional to the log of time (Marone *et al.* (1991)):

$$slip \approx \alpha \ln(\beta t + 1)$$

For the year of data following the mainshock, they find that $\beta = 71.2 \pm 22.1\ yr^{-1}$, whereas for the first 3.5 days after the event, measurements with extensiometer data yielded $\beta = 6.5 \pm 0.6\ yr^{-1}$ (Heki 1997b). The functional form of the logarithmic decay of afterslip invoked in this study is based largely on that predicted by the state- and rate-dependent friction laws, as discussed in Marone *et al.* (1991). However, the large discrepancy in the decay rate β arises from applying a single formula to describe phenomena whose underlying causes are not known, and further, the highly different values of β suggest that either the rapid deformation immediately following the event (e.g., the first few days) is causally unrelated to the longer term trend or that a logarithmic decay is too simplistic a way to describe the process. Either way, since any mechanistic argument regarding the causal slip properties depends on the time interval of post-seismic deformation considered, we confine ourselves to the 10 days between the mainshock and the M_w 6.9 aftershock, during which time the post-seismic deformation is 1) too fast to be attributed to crustal or asthenospheric relaxations, and is therefore most easily explained as some sort of afterslip on the co-seismic fault, and 2) similar to that observed at Jalisco during the equivalent time period.

3.3.3 1995 Antofagasta Event

The Antofagasta earthquake occurred July 30, 1995, offshore Northern Chile, along the East dipping interface between the Nazca and South American plates. The preliminary USGS surface wave magnitude was reported as M_s 7.3, but the revised Harvard moment magnitude was reported as M_w 8.1. The large discrepancy between surface wave and moment magnitudes suggests that this earthquake might have had some component of slow rupture propagation (Ruegg *et al.* (1996)). Prior to the event nearly the whole territory of Chile and western Argentina had been instrumented with a network of over 200 GPS monuments and occupied as recently as 1994 (Figure 3.11). Collectively known as the SAGA network (South American Geodynamic Activities), it was established and is operated by the GeoForschungsZentrum Potsdam in cooperation with many partner institutions from the host countries (Klotz *et al.*

(1996)). Many of these stations were located within the near field of the Antofagasta earthquake (Figure 3.11).

Figure 3.12 shows the co-seismic displacements as measured during the event. The network also had several continuously operating receivers during the time of the earthquake, one of which was located just south of the Mejillones Peninsula near the town of Antofagasta, Chile, and nearly directly over the epicenter. This station recorded nearly continuously up until the time of the earthquake; missing are data from one-day segments from 3 days prior to the event, the day of the event, and 15 days after the event. The data loss from the day of the event was caused by an earthquake-induced regional power failure. The station came back on line roughly 24 hours after the event and recorded continuously afterwards.

Figure 3.13 is the time series of this station, starting 20 days prior to the earthquake through 30 days afterwards. It is clear that within the noise level (approximately 10% of the co-seismic) of the data there is no significant afterslip. There may be some hint of it in the North component, but nothing resolvable in the East-West component, which had the largest co-seismic displacement and would therefore be expected to have the largest post-seismic as well. Furthermore, there is nothing resolvable on the vertical component, either co-seismic or post-seismic. We can therefore state that within the current noise level of our data, which is about 10% of the co-seismic signal, we cannot infer any significant post-seismic deformation.

There is no obvious geometric barrier to observing post-seismic deformation at Antofagasta; relative to Jalisco and Sanriku the position of the GPS site to the co-seismic slip patch is not unusual.

Figure 3.14 is a simplified comparison of distances between the ocean-floor expression of the trench, the GPS receiver, and the lower faulting limit of co-seismic faulting as inferred from GPS and source time function analyses. The down dip extent of faulting is defined as the lower limit of at least 0.5 meters of slip, although there are great uncertainties in these estimates. Nonetheless, any significant creep following the Antofagasta event would be observed at the GPS site.

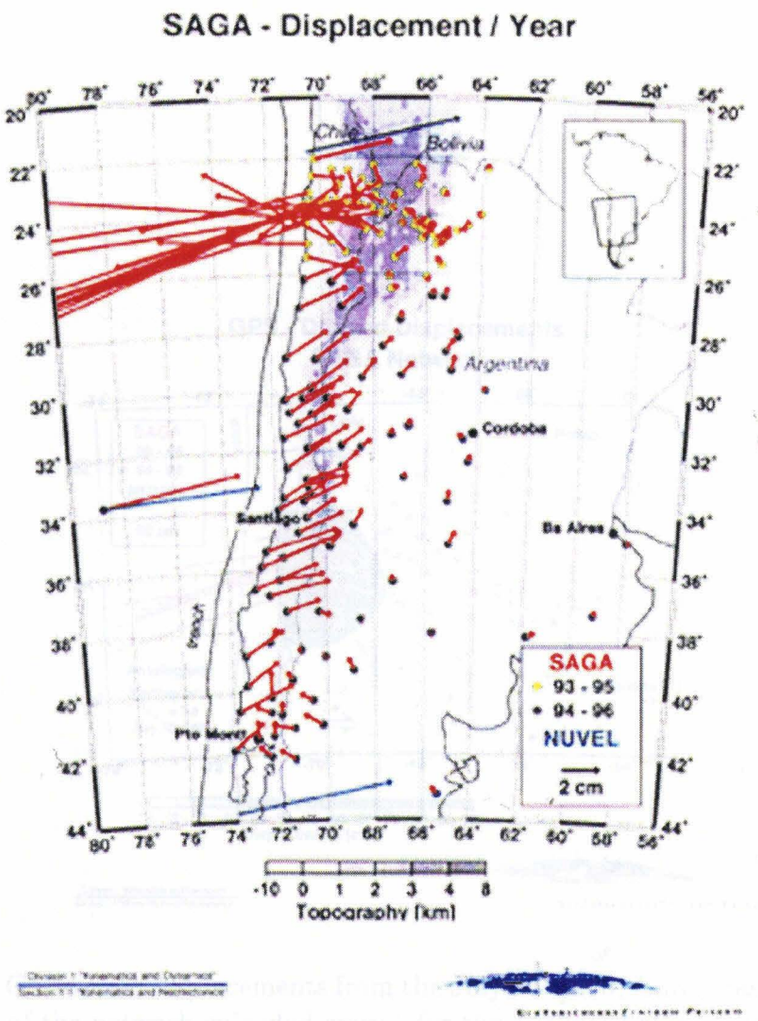

Figure 3.11: South American Geodynamics Array (SAGA) operated by the GeoForschungZentrum Potsdam. The continuous station whose time series are shown in figure 3.13 is shown in red. This station measured continuously up until the time of the earthquake, when it experienced a 24 hour power failure due to strong ground motion. Once back online, the station operated continuously thereafter. Digitized from unpublished data provided courtesy of C. Reigber, GFZ Potsdam.

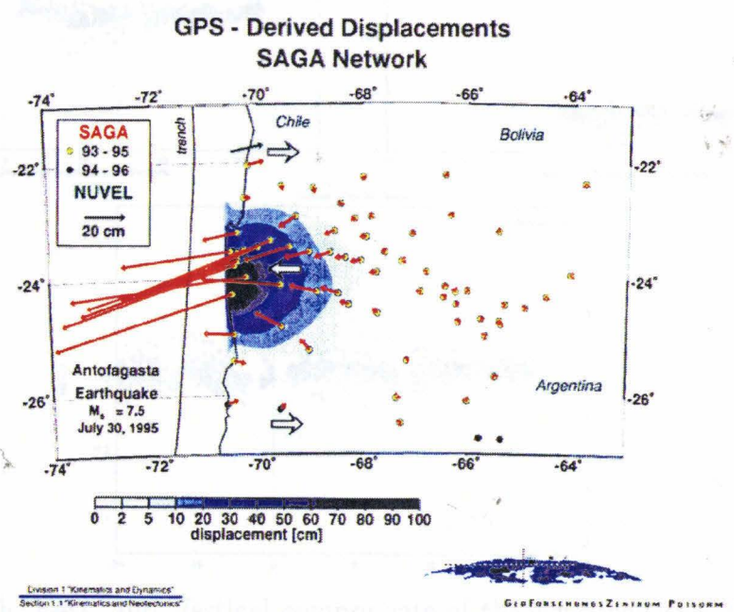

Figure 3.12: Co-seismic displacements from the July 30, 1995, Antofagasta subduction event. Most of the network subsided except for the outboard station at the southern end of the Mejillones Peninsula, which experienced co-seismic uplift. The continuous station which produced the time series shown in Figure 3.13 lies on the coast near the region of maximum co-seismic offset. Digitized from unpublished data, courtesy of C. Reigber, GFZ Potsdam.

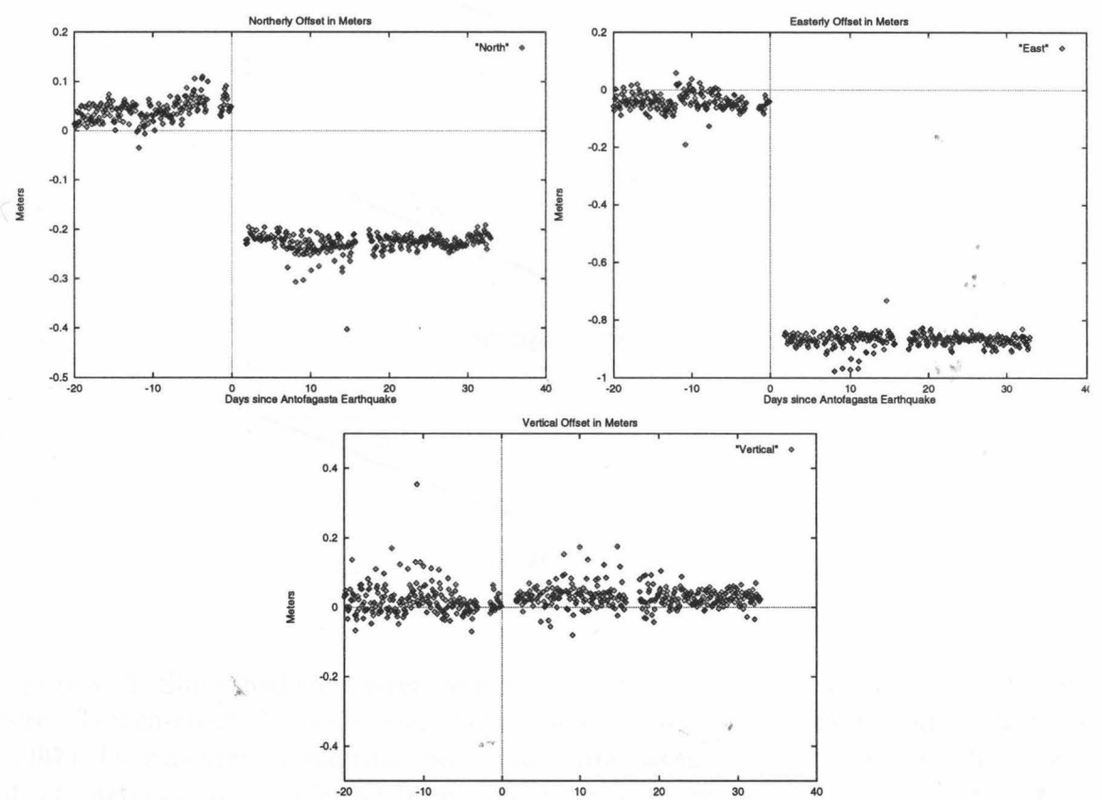

Figure 3.13: North, East, and Vertical components of the Antofagasta GPS station measured during the July 30, 1995, subduction earthquake. These are two hour solutions. (Unprocessed data provided courtesy of C. Reigber, GFZ Potsdam.)

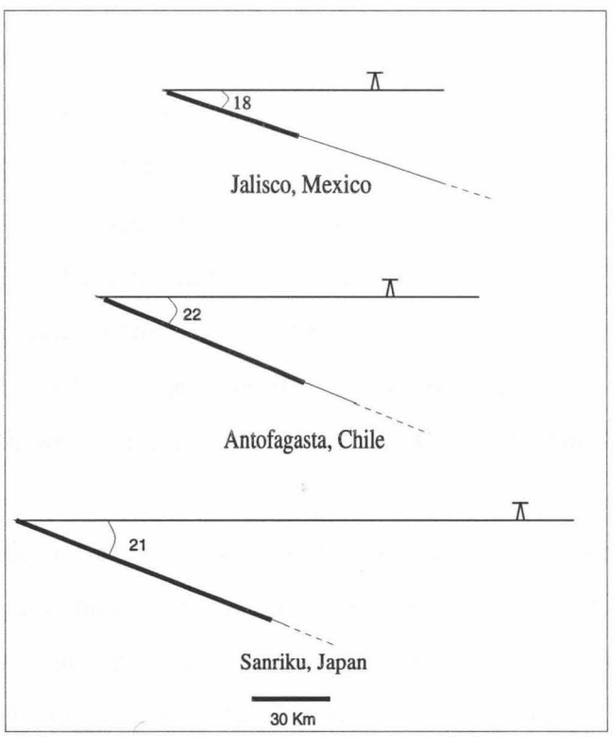

Figure 3.14: Simplified trench-receiver geometry for the three GPS data sets discussed here. Trench-coast distances and shallow slab dip-angles are taken from McCaffrey (1997). Depth extent of faulting (heavy black line) as shown indicates down-dip extent of 0.5 meters slip, as inferred from geodetic and source analyses (Melbourne *et al.* (1997); Ihmle and Ruegg (1997); Tanioka *et al.* (1996)). All three GPS receivers are located at or near sea level along the coast. Not shown are the relative sizes of the accretionary prisms (see Figure 3.20). The trench-coastline distance varies considerably, but the receiver positions relative to the lower limit of faulting are roughly the same. Complexities of the spatial slip distribution will outweigh any geometrical barrier to observing post-seismic deformation at Antofagasta.

3.4 Slip Distributions

3.4.1 Deformation Modelling

To summarize the observations, in two of the three data sets described above, there is strong evidence of rapid deformation following the mainshocks. Given current estimates of the relaxation timescales predicted by lower crustal and asthenospheric viscosities (Thatcher (1984)), this deformation is most readily explained by aseismic afterslip (creep) along the mainshock fault system. In the Jalisco event, the tide and GPS data together suggest an estimate of the two week post-seismic deformation to be approximately 70% of the mainshock. In the Sanriku event, which had continuous GPS observations spanning the time of the earthquake, we see an additional deformation equal to 30% of the co-seismic during the 10 days following the mainshock, while at Antofagasta we see no observable post-seismic deformation above the noise level.

Unlike the Sanriku data, which we discuss first, the unique aspect of the Jalisco data is that they clearly show that station CRIP was post-seismically uplifted over the 9 day span of the continuous data collection, despite having co-seismically subsided. This uplift is strongly suggested in the tide data recorded from 0 to 6 days after the event, and is irrefutable in the GPS time series from 6 to 15 days after the event. By considering the post-seismic deformation to be caused by aseismic afterslip, we can invert the surface deformation for the causal slip. It is therefore useful to discuss the general pattern of deformation produced by a shallowly dipping thrust fault.

For vertical deformation, the boundary between uplift and subsidence for a uniform slip fault delineates a trench-parallel axis, or hingeline, whose position lies near the surface-projected down-dip terminus of fault rupture (Figure 3.15). This dependence allows estimation of the down-dip limit of faulting through identification of the null-displacement node at the surface. As most large subduction zone earthquakes rupture along faults extending under the onshore continental region, uplift and extension dominate the near-coastal deformation signal. When subduction events have very shallow faulting and a trench located sufficiently far offshore, the deformation

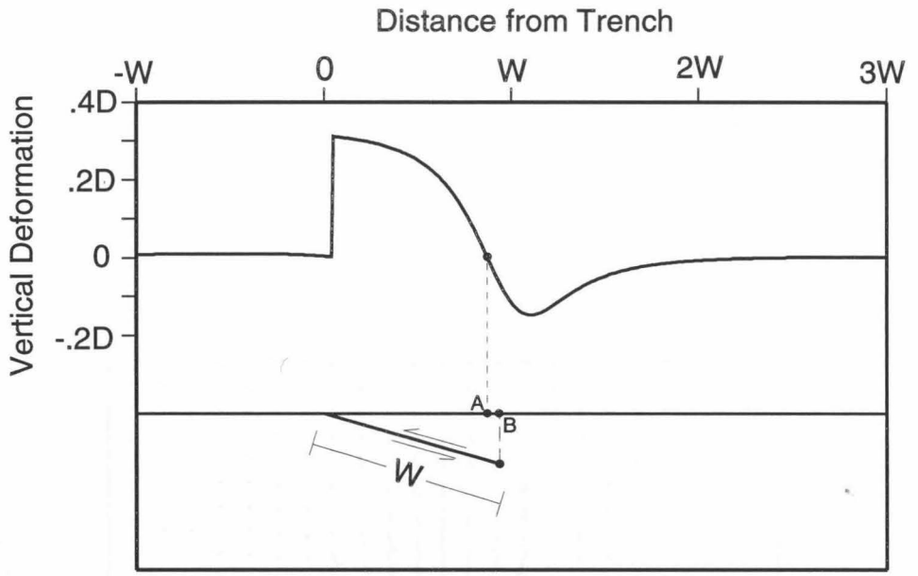

Figure 3.15: Vertical deformation profile for a uniform-slip, shallow thrust fault of width W, dipping 18° and slip D. The boundary between coseismic uplift and subsidence delineates a trench-parallel axis, or hingeline (A), whose position lies near the surface projection of the down-dip terminus of fault rupture (B). Calculated from Okada (1993).

hingeline lies also offshore and the coastal region experiences co-seismic subsidence instead of uplift (Melbourne, 1997).

In contrast to the vertical, the horizontal component of surface deformation is less sensitive to the depth of faulting than to the spatial locus of faulting moment. As is shown in Figure 3.16, the azimuth of displacement is constant along any radial line emanating from the fault, while the amplitude simply decreases with distance rather than flipping sign like the vertical. This holds true for finite dislocations with dimensions small compared to the receiver distance. Therefore, to determine that co- and post-seismic slip actually occurred in different locations requires observing significantly different vertical displacements or horizontal azimuths, in the co- and post-seismic deformation. Unless the two signals are demonstrably different, it is difficult to distinguish between continued faulting along the co-seismic rupture plane and post-seismic faulting along new regions of the plate interface. The optimal geometry for discerning between the two is to have stations immediately overlying the

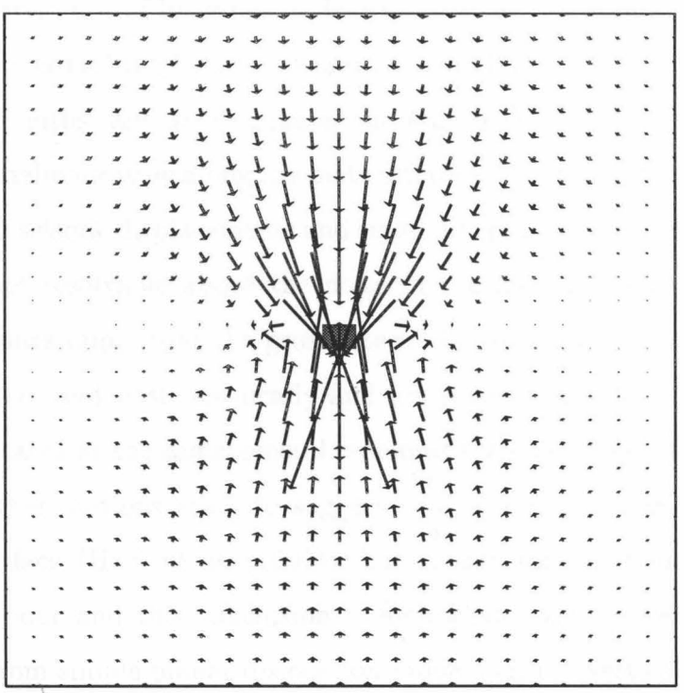

Figure 3.16: Map view of horizontal deformation due to a uniform-slip shallow thrust fault. The displacement vector azimuths follow ("point to") the locus of faulting with amplitudes which decrease with distance. The sense and amount of offset are therefore not particularly sensitive to the lower limit of faulting. Calculated from Okada (1993).

co-seismic rupture concentrations such that differences in faulting location produce noticeable changes in azimuth and vertical motion.

Sanriku-Hakura-Oki

As can be seen from Figure 3.9, the station geometry of KUJI relative to the modelled co-seismic fault plane renders the vertical motion insensitive to the lower limit of faulting and therefore is of little use in determining the depth of afterslip. Similarly, lateral variations in faulting location would only produce small changes in horizontal deformation azimuths, and so in general the station KUJI alone is of little use in defining the afterslip location along the plate interface. Easterly offsets dominate both the co- and post-seismic displacements and small differences in the exact displacement azimuths are not resolvable above the noise in the measurements. This constant-azimuth offset does imply that the gross lateral distribution of slip is approximately the same both co- and post-seismically and led Heki *et al.* (1997) to infer that the afterslip was located at the same general region as the co-seismic slip. Displacements measured at other stations seem to suggest that afterslip continued evenly across the rupture surface (Heki *et al.* (1997)), but in general the resolution of the slip distribution is poor and this conclusion is somewhat unsupported. Although it is not predicted from simple planar dislocation modelling, the vertical time series from station KUJI (Figure 3.10) shows uplift during the event, whereas slight subsidence is expected and suggests deviations from a planar fault. The Sanriku time series is therefore of use in assessing the net rates of post-seismic deformation but is of little use in defining where such afterslip occurred.

Delineating the Jalisco Post-Seismic Faulting

In contrast to the weak KUJI-Sanriku geometry, station CRIP from the Jalisco data set overlies the inferred downdip terminus of the co-seismic rupture plane and is therefore well suited for differentiating between co-seismic and post-seismic slip locations. As with the Sanriku observations, the horizontal azimuth of post-seismic deformation at CRIP is approximately the same as the co-seismic, indicating that the approximate

geographic concentration of post-seismic faulting relative to CRIP was at the same azimuth as the co-seismic (218° versus 213°). However, the post-seismic deformation measured in the 9 days after the mainshock has vertical motion opposite to that of the co-seismic (post-seismic uplift versus co-seismic subsidence). This reversal in the vertical sense of motion without significant change in the horizontal offset azimuths is consistent with the locus of afterslip being located downdip from the co-seismic locus. As can be seen in Figure 3.17, the reversed vertical motion alongside nearly identical horizontal motion is most easily explained by additional faulting migrating after the event directly down-dip of the co-seismic fault plane, thereby effectively moving the hingeline between elastic uplift and subsidence inland and causing uplift at CRIP. There could also have been continued slip over the same region that broke co-seismically, but the majority of post-seismic slip is required to be located further downdip from the majority of co-seismic rupture.

Since we have continuous data from only one station, it is hard to distinguish between different modes of fault propagation, but we can use the relative amounts of vertical and horizontal post-seismic deformation to make a rough estimate of the general locus of faulting. Figure 3.17 shows how the vertical deformation profiles vary for two end-member possibilities; the top panel shows the deformation field caused by increasing the down-dip limit of faulting along a rupture patch which breaks the surface, while the lower panel shows a sequence of 25 km thick 'ribbon' faults breaking at increasing depths down the plate interface. Similarly, Figure 3.18 shows the corresponding trench-normal horizontal offsets, and Figure 3.19 shows profiles of the ratios of vertical to trench-normal offsets for these two end member models. The top panel corresponds to the increasingly wider thrust fault which breaks the surface, while the lower panel shows that for the 'ribbon' fault.

The 3D GPS time series at CRIP show post-seismic trench-normal horizontal deformation simultaneous with vertical uplift, which we can use to differentiate between the two end member models presented here. During the 9 day continuous measurement, the station had a ratio of vertical to horizontal post-seismic deformation equal to about 1. Since CRIP is located 85 Km from the trench offshore Jalisco, on Figure

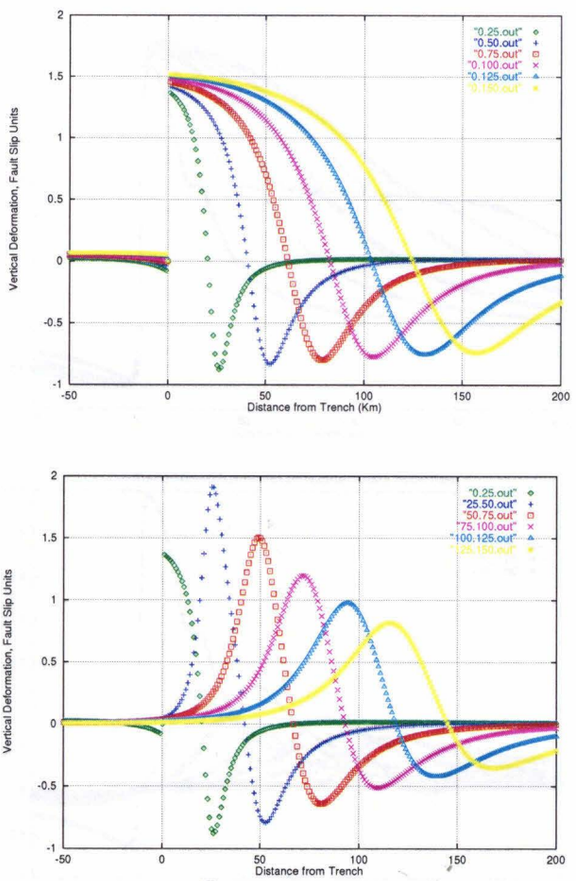

Figure 3.17: Vertical deformation expected as a function of distance from the trench, for two end-member types of fault slip. (Top) Variable depth uniform slip thrust faulting in which the fault breaks the surface. Lower limit of faulting varies from 25 to 150 Km down dip at 25 Km intervals. (Bottom) Constant 25 Km thick uniform slip thrust fault with updip limit of faulting varying from 0 to 125 Km down dip. In each case the dip of the fault plane is assumed to dip at 20°. The vertical deformation scales linearly with slip amount. Calculated from Okada (1993).

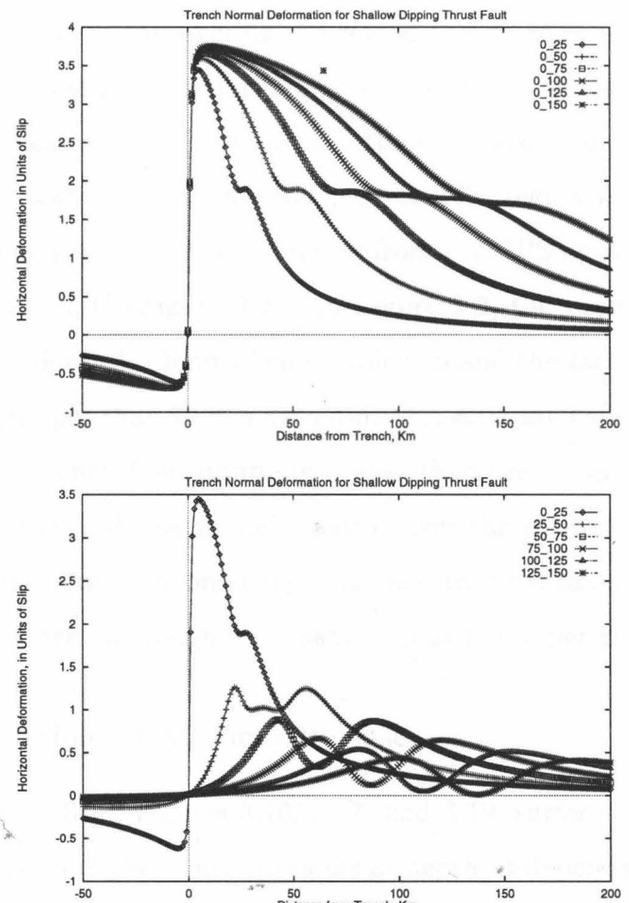

Figure 3.18: (Top) Trench normal horizontal deformation for variable lower depth-limit uniform slip thrust faulting in which the fault breaks the surface. Lower limit of faulting varies from 25 to 150 Km down dip at 25 Km intervals. The shoulder corresponds to the surface projection of lower limit of faulting. (Bottom) Constant 25 Km thick uniform slip thrust fault "ribbon" with updip limit of faulting varying from 0 to 125 Km down dip. Fault plane dips at 20° in all cases. Calculated from Okada (1993).

3.19, therefore, the CRIP data sit at (x,y) = (85,1). On the top plot, the ratio of vertical to horizontal motion never exceeds 0.4, whereas for the ribbon fault, the horizontal motion drops off quickly with depth (Figure 3.18) and the ratio of vertical to horizontal motion quickly increases. The curve appropriate for a ribbon fault which best fits the CRIP data by intersecting the region of x,y=85,1, is that which corresponds to faulting located between 100-125 Km downdip, or an absolute depth of 31-38 Km. This indicates that if one ascribes the post-seismic deformation to faulting, it most likely occurred in this general region. This region lies down-dip of the best fitting co-seismic slip distribution inferred from the GPS network measurements as discussed in Chapter II (Figure 2.2). In Figure 2.2, the most robust aspect of that inversion is the down-dip limit of co-seismic slip and the fact that there was no significant faulting deeper than 70 Km downdip. Our estimate here indicates that the postseismic faulting occurred substantially deeper than the co-seismic. The assumptions here are that the post-seismic deformation over the entire 9 day period was a result of afterslip on a single region of the fault, and that the fault downdip from the co-seismic rupture patch has roughly the same dip as the upper part.

Inverting Deformation for Moment Release

As is readily observed from Figures 3.18, 3.17, and 3.19, surface deformation is not simply a linear function of the moment release at depth; it depends heavily on where the faulting occurs. Although seemingly obvious, this point is often not fully realized, and spurious estimates of moment release can be inferred from surface strain or deformation data, particularly if the data is sparse and the post-seismic rupture plane is inferred to have a different location than the co-seismic. For example, in documenting the ultra slow earthquake offshore Sanriku in 1992, Kawasaki *et al.* (1995) infer that up to a factor of 10 more energy could have been released during the day following the earthquake than during the co-seismic rupture itself. This is based on two strain measurements in which the strain change over the day following the event is a factor of 2 greater than that which occurred during the event. The factor of 10 is therefore a reflection of where they put the causal slip of the post-seismic strain change, which

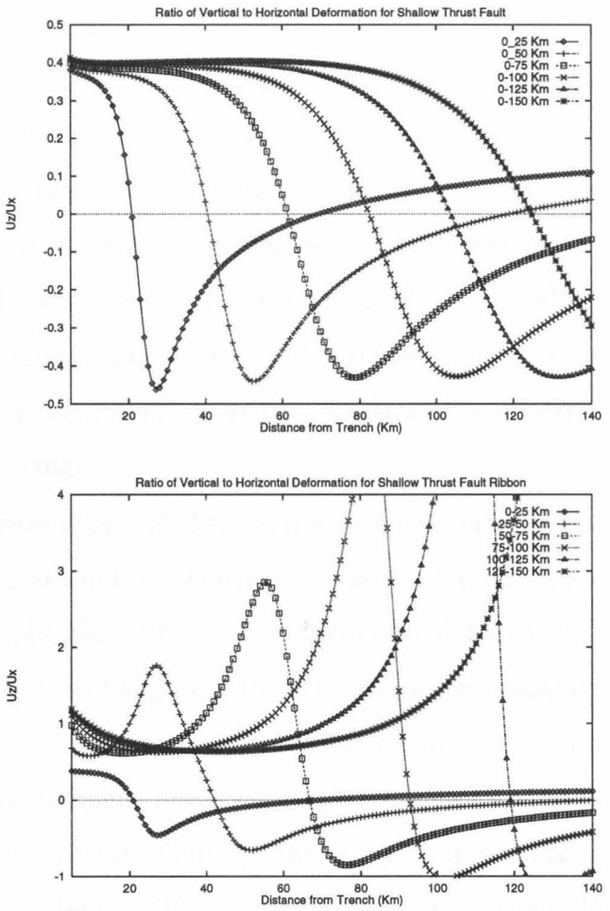

Figure 3.19: (Top) Ratio of vertical to horizontal deformation for shallow thrust fault which breaks the surface but have increasingly deeper lower limit of faulting. The down-dip faulting distance varies from 25 to 150 Km at 25 Km increments. Notice that for this type of thrust fault, the ratio never exceeds 0.4, meaning that for a shallow dipping fault the horizontal motion is greater than the vertical at all depths. (Bottom) Ratio of vertical to horizontal deformation for shallow 25 Km down-dip thickness thrust fault "ribbon." Because of the rapid decrease in trench-normal surface deformation with increasing "ribbon" depth (Figure 3.18), the ratio can reach much higher values. For the data from CRIP, which is located 85 Km from the trench, the ratio of the vertical to horizontal post-seismic deformation is about 1; the curve which is closest to this value at 85 Km from the trench is derived for faulting occurring between 38 and 46 Km depth (125-150 Km downdip distance from trench). Calculated from Okada (1993).

is not well determined.

With post-seismic deformation whose causal fault plane cannot be well located, the most conservative assumption is that the post-seismic faulting occurred in the same region as the co-seismic. With this assumption, the measurable surface deformation scales linearly with the amount of faulting at depth, and therefore with moment release. Had this assumption been made for the 'ultra slow' Sanriku 1992 event, a factor of 5 less post-seismic moment release would have been inferred. For the Sanriku data here, employing this assumption yields an additional 30% moment release, at Antofagasta none, and at Jalisco about 70%. However, the moment release estimate for Jalisco can be improved because we can constrain the relative locations of the co- and post-seismic faulting.

As shown in Figure 3.19 and discussed above, the most probable location of the post-seismic faulting was in the vicinity of 31-38 Km absolute depth, as inferred from the nearly equal amplitudes of horizontal and vertical deformation of CRIP and the coarse dislocation models of Figure 3.19. We can use this location to better estimate how the vertical deformation, particularly that recorded by the tide gauges, can be used to constrain the moment release during this time. An assumption I make here is that all of the post-seismic faulting, including that recorded by the tide gauge, occurred near 40 Km depth. This is not necessarily correct, but our data are to sparse to constrain how the post-seismic rupture path moves with depth.

In calculations similar to those in Figure 3.17, for a uniform slip ribbon of thrust faulting located between 40 and 65 Km downdip on a subduction zone appropriate for Jalisco (see Chapter II), the ratio of vertical deformation produced at the station CRIP to slip on the ribbon fault is about 0.1, i.e., for every 5 m of slip on the fault there is 0.5 meter of vertical motion. For the 25 Km thick ribbon located nearest the post-seismic locus of faulting, this ratio is closer to 0.16, simply because the locus of faulting is nearer to the measurement point and produces greater deformation there for the same amount of slip. Roughly speaking, then, a meter of post-seismic deformation caused by slip along the estimated post-seismic fault plane indicates only about 5/8 of the moment release along the co-seismic rupture patch needed to

produce the same amount of deformation. Given these simple geometric arguments, then, and our best estimates of the location of the co-seismic and post-seismic fault planes, the 70% additional vertical post-seismic motion indicated by the GPS and tide data indicate approximately an additional 40% extra moment release. However, as should be evident, this is at best a coarse estimate given the uncertainties.

3.5 Discussion

Geodetic surveying following large subduction earthquakes has documented post-seismic deformation occurring with timescales of months to years, but evidence of movement during the days following a large earthquake is much more scarce. As mentioned above, this is mainly because the time interval needed to complete network-wide measurements prohibited the identification of transient deformation occurring immediately after the event. Nonetheless, significant longterm post-seismic deformation has been recorded throughout tectonically active environments, most notably Japan, where it is well documented along both interplate convergent margins (Thatcher (1984); Thatcher and Fujita (1984); Thatcher and Rundle (1984)) and intraplate transform faults (Nakano and Hirahara (1997)); in Alaska following the 1964 Good Friday earthquake (Savage and Plafker (1991), Cohen (1998), and in Chile, following the great 1960 event (Barrientos *et al.* (1992)). In these studies, significant amounts of long term post-seismic deformation occurred with varying timescales, but generally with deformation rates decreasing with elapsed time after the event. Thatcher (1984) identified two distinct relaxation times following the 1946 Nankai Trough earthquakes. The first, of about a year or less, he ascribed to deformation concentrated close to the co-seismic rupture plane, while the second, occurring over several tens of years, was attributed to a diffusive spread of the deformation landward and was found to be consistent with models employing an elastic plate overlying a viscoelastic asthenosphere. Deformation here with the year-long timescale was found to be consistent with very localized deformation downdip of the co-seismic rupture plane. Other studies have also inferred down-dip migration of seismicity from the co-

seismic rupture plane. Using tide gauge measurements from southeast Alaska, Savage and Plafker (1991) also found that the post-seismic uplift occurred in areas which had co-seismically subsided. Although the post-seismic relaxation time here was found to be on the order of 5 years, the deformation is attributed to creep on the plate interface directly down-dip from the co-seismic rupture plane as well. Additionally, Thatcher and Fujita (1984) found downdip deformation amounting to 40% of the co-seismic over 10 years. Following the Chilean event, 75 cm of post-seismic deformation over 30 years (Barrientos *et al.* (1992)) also was interpreted to be caused by creep localized downdip of the co-seismic rupture plane. Due to sparsity of the data here, however, there is little control on exactly what percentage of co-seismic energy release this amounts to. Variation of post-seismic rebound was found on shorter timescales following the 1960 Alaska event; here about 15 cm of uplift was found after a year following the event, and also showed evidence for a modest decrease in the uplift rate a few months after the earthquake occurred.

It is important to note that because the post-seismic deformation described in this work occurs so quickly after the mainshock, in the preexisting measurements of post-seismic geodetic deformation this phenomenon would have gone undetected due to the time delay between an earthquake and re-measurement. Therefore, the lack of historical reports of rapid post-seismic deformation similar to that reported in this study does not preclude its occurrence in other large subduction events which have received detailed analysis. It is only the deployment of continuous geodetic measurements which now allows identification of rapid post-seismic faulting. In fact, if anything, the large degree of variability in the documented relaxation times suggests that deformation might regularly occur along very short timescales.

If one looks at recent earthquakes along the convergent margins which have been continuously measured, there is additional evidence to suggest that post-seismic faulting occurs along very short timescales. Since 1992 there have been three subduction events offshore northeastern Honshu which have had reports of significant post-seismic deformation on timescales ranging from days (Kawasaki *et al.* (1995)), to months and years (Heki *et al.* (1997)). Of these, the case most relevant to the present study is the

documentation of a 'ultra slow' earthquake immediately following the 1992 Sanriku-Oki event offshore northern Honshu, in which up to a factor of four greater amount of energy was released over the day following the earthquake than during the main-shock itself (Kawasaki *et al.* (1995)). As in other studies of this type, the quantity of postseismic moment release is not well constrained due to difficulties associated with determining the location of post-seismic faulting. Just to the south of here is the source of the Sanriku data discussed here and more generally in Heki *et al.* (1997).

To summarize, the observations presented here bolster the high frequency end of the post-seismic deformation spectrum. In combination with the pre-existing literature, we can state that post-seismic faulting following subduction earthquakes does in fact occur over timescales ranging from 100s of years (e.g., Thatcher (1984)), tens of years (Barrientos *et al.* (1992)), years (Cohen (1998); Hirahara *et al.* (1996)), and months (Heki *et al.* (1997)) to days (Kawasaki *et al.* (1995), Heki and Tamura (1997)) and fractions thereof (this study).

Perhaps the most important implication of the rapid post-seismic deformation is its impact on global seismic coupling, which is defined as the ratio of seismically inferred convergence and globally determined plate convergence rates using plate tectonics and geodesy. This ratio is known to be substantially less than one, for example, along the Kurile-Bonin trench the seismic coupling is estimated to be 0.3 (Kanamori (1977)). If rapid post-seismic faulting is found to be common in subduction zones, then this may reduce the problem by accounting for significant portions of the global slip deficit. The three data sets studied here comprise the most thorough continuous geodetic observations of large subduction zone events to date. The fact that two of them show afterslip equal to 70% (Jalisco) and 30% (Sanriku) of the co-seismic implies that for at least some subduction zones the rapid post-slip will significantly impact estimates of the global slip deficit.

What controls post-seismic slip?

An obvious question raised by the three GPS time series shown here is, what controls this ultra-rapid deformation in subduction zones? Why should two subduction events

with moment-magnitudes of 7.5 and Mw 8.0 exhibit this behavior while a third, with Mw 8.1, fails to? Possibly, only certain subduction zones exhibit the necessary thermal and physical properties which allow rapid post-seismic deformation, but it may not be only a function of the specific convergent margin. There is no data to constrain whether a given subduction zone always exhibits the behavior in all events or only a subset of them, and it is possible that rapid post-seismic creep is confined to only certain events depends on temporally varying aspects of the seismic cycle. The amount of time since the last event broke the plate interface could be a likely candidate, for example. Fault interface 'healing' rates are a fundamental parameter in velocity dependent friction laws (Scholz (1998)) and introduce a time dependency into observable phenomenon such as post-seismic creep. Alternatively, such creep may be a function of the stess drop during the event, which again will vary with different events at different locations. Because these observations are new, there is little pre-existing work which addresses the underlying mechanism of this type of deformation.

There are two general classes of mechanistic explanations of afterslip, both of which were formulated to explain the deformation occurring over timescales of years rather than the very rapid displacements measured here. The first class of models are those which attribute post-seismic deformation at a point to be due to the integrated effect of the relaxation of a viscoelastic half-space underlying an elastic plate (Thatcher (1984)). The best estimates of asthenospheric and lithospheric viscosities, however, produce a minimum relaxation time on the order of years, which prohibits the deformation rates seen in our data. The other class ascribes the post-seismic deformation to processes occurring along the plate interface itself, usually on or nearby the co-seismic rupture patch (eg, Marone *et al.* (1991)). These are frictional models rather than fracture mechanisms, and are concerned with the friction along the fault interface and the dynamics of earthquake nucleation and propagation. From the basic constitutive laws, inferences about post-seismic deformation are made which have no intrinsic lower time limit of occurrence except for that limited by the frictional processes. The most plausible, therefore, are those mechanisms related to the properties

of the plate interfaces and dislocation surfaces to explain the deformation rather than a process intrinsic to the regional lithospheric structure.

The concept of frictional stability transitions has been used to explain a host of observations regarding the behavior of faults which show afterslip; the constitutive relations and the formulation of the friction laws are detailed in Marone *et al.* (1991) and Scholz (1998); here we suffice to describe the general behavior these laws predict. In this type of model, the friction along a fault is velocity dependent; those regions in which friction decreases with velocity, known as velocity weakening, are unstable and can nucleate and propagate seismic rupture. Regions in which friction increases with velocity are stable and any rupture propagating from elsewhere into this region is rapidly quenched. Between these two behavior types lies a conditionally stable field in which the system is stable under static loading, but can become unstable if given a sufficiently strong transient velocity. This region is thought to be unable to nucleate frictional failure, although rupture fronts can propagate into this type of region from elsewhere. Thus this region probably holds the key to explaining our rapid afterslip. Temperature seems to control the transition from unstable to metastable frictional properties (Marone and Scholz (1988)), and as down-dip temperatures can be modelled from convergence rate and plate ages, our ability to determine for Jalisco that the post-seismic faulting occurred downdip of the co-seismic is important for testing these friction-based models.

From a perspective of the subduction zone observations presented here, the frictional properties of the plate interface to a large degree probably depend on the frictional properties of subducted terrigenous and pelagic sediments. The role of sediments in subduction zones has been discussed at length, but there are no clear constraints on how sediments atop the convergent plates are partitioned between accumulation in the accretionary wedge and subduction down the trench. In Cascadia, for example, in which the Juan de Fuca plate carries a sediment load several kilometers thick, MCS data and volumetric analysis indicate that very little of that sediment actually subducts; thrust faults within the accretionary wedge penetrate close to the top of the underlying oceanic crust, and it appears that nearly all of it is scraped

off (Hyndman and Wang (1995a); Davis and Hyndman (1989)). Offshore Jalisco, on the other hand, the Rivera plate has a much lighter sediment load, on the order of 1 Km (Danobeitia *et al.* (1997)), but very little accretionary material is found here, and so the assumption is that most of the sediments are subducted. In general, probably no single subduction-related tectonic process controls the amount of sediment subducted, but instead this is a function of the transpressional stress across the subduction interface, the age of the plate, the convergence rate, etc. Figure 3.20 shows the relative sediment thicknesses atop the convergent oceanic plates at the subduction zones discussed here.

The thermal and chemical processes which the subducted sediments experience also play a role in their mechanical behavior at depth, in that correlations have been established between the observed afterslip and the amount and degree of consolidation of sediments (Williams and Magistrale (1989)). Therefore, again, the plate ages, convergence rates and sediment loads will all determine how sediments at depth behave.

The other significant item about subduction zones is that locked portion of subduction zones rarely extends to the surface, and for some the shallowest few kilometers of the plate interface are non-seismogenic (Tichelar and Ruff (1993)). At the downdip end, the cutoff of seismicity appears to coincide with a critical temperature, in that for temperatures higher than the critical temperature seismicity ceases.

Unfortunately, we really only have one data set, that from Jalisco, to use here in terms of elucidating a model of the causal properties of rapid afterslip, because only the Jalisco data set has the geometry which allows delineation of the post-seismic faulting. The Sanriku deformation, while of high quality and interesting in its amplitude decay, is not sensitive to the distribution of faulting.

To explain the long term afterslip of intraplate transform events (e.g., afterslip following the 1966 Parkfield event), Marone *et al.* (1991) combined the concept of dynamic friction laws with sediment rheological experiments to propose a model for earthquake afterslip. In this model, a lower region possessing velocity weakening friction underlies an upper region with velocity-strengthening behavior. To explain

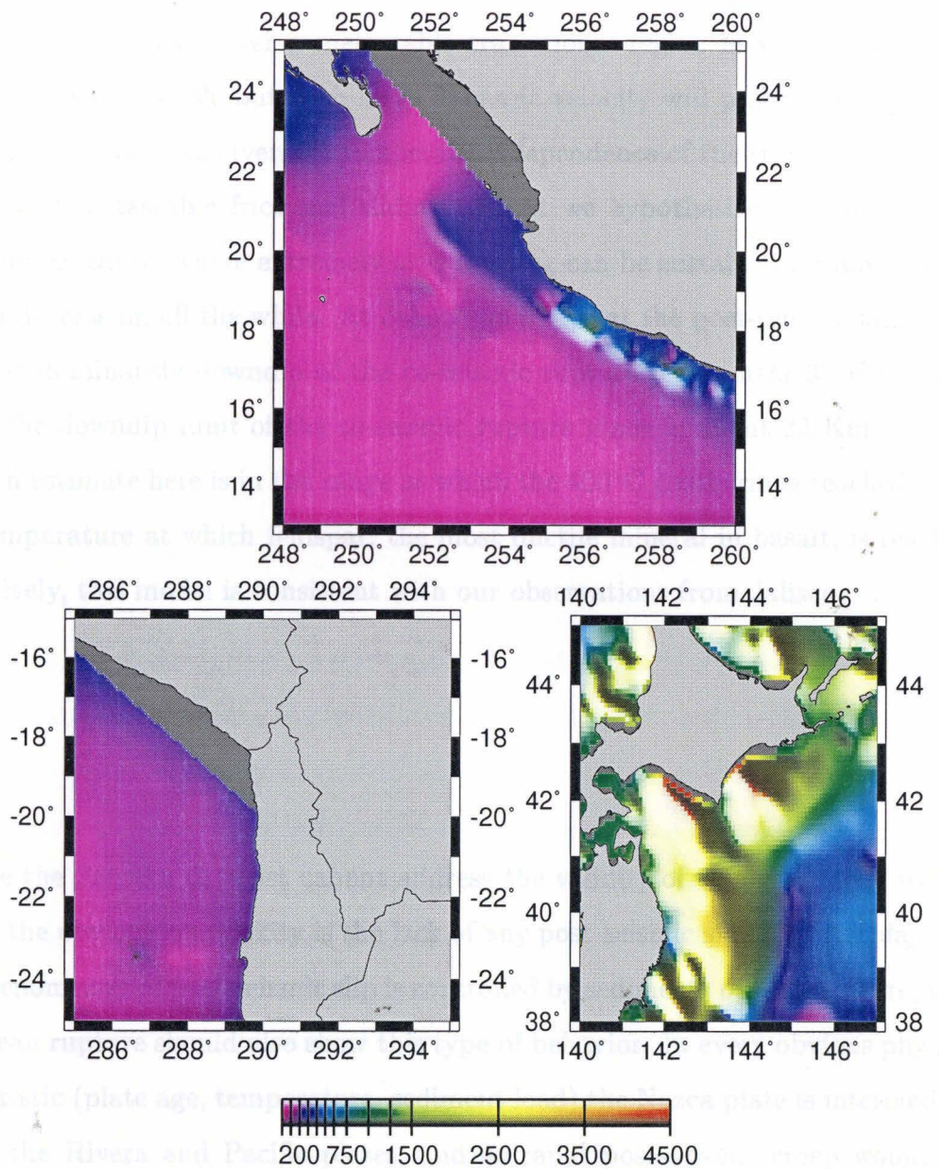

Figure 3.20: Sediment thickness on convergent margins offshore Jalisco, Sanriku and Antofagasta, Chile. In general the offshore sediment thickness is not a good indicator of their mechanical role along the plate interface, since the accretionary wedge thickness is a function of the plate age, the continental deposition rate, and the amount of sediment being subducted (NOAA, 1991).

our data, in particular the Jalisco data, where we have control on the post-seismic faulting location, we would take this model and invert it, putting the tightly bound, velocity-weakening layer over a metastable transitional region in which earthquake nucleation is not possible but with large dynamic velocity will propagate slip. This model is entirely feasible given the temperature dependence of the transition between unstable and metastable frictional sliding. What we hypothesize for Jalisco is an equilibrium situation where extremely slow faulting can be sustained for days on end although decreasing all the while. At Jalisco we find that the post-seismic faulting is located predominantly downdip of the co-seismic rupture plane, near 35 Km depth, whereas the downdip limit of the co-seismic rupture plane is about 22 Km. The 35 Km depth estimate here is in the range at which the 450°C geotherm is reached. This is the temperature at which feldspar, the most ductile mineral in basalt, is reached. Qualitatively, this model is consistent with our observations from Jalisco.

While the Sanriku data set cannot address the validity of this model one way or another, the obvious complexity is the lack of any post-seismic signal at Antofagasta. If the phenomenon of post-seismic slip is controlled by sediments or temperature, then the Chilean rupture should also show this type of behavior. In every obvious physical characteristic (plate age, temperature, sediment load) the Nazca plate is intermediate between the Rivera and Pacific plates, and so rapid post-seismic creep would not appear to be controlled by any one particular physical parameter. For example, the age and convergence rates of the Rivera, Pacific, and Nazca plates are 9, 41, and 132 Ma, and 49, 74 and 76 mm/year, respectively (McCaffrey (1997)). Future modelling of different friction regimes will help find the answer, which may lie in such issues as stress drop during the earthquake or the bulk chemistry of the materials in which it is found. In any event, with the increase in continuous monitoring of subduction zones around the world the answers to these questions will eventually be found.

Chapter 4 Fine Structure of the 410 Km Discontinuity

4.1 Abstract

The 04/14/95 earthquake in western Texas (Mw 5.7) produced a strong topside reflection off the 410 km discontinuity which was recorded on a multitude of seismic arrays throughout the southwestern United States. Data from 394 vertical short-period and 24 broadband instruments provides dense coverage of this event from distances of 11° to 19° and provide a detailed look at sub-continental 410 structure. The salient features of this data set are 1) the strong dependence on wavelength of the 410 km triplication range, 2) the uniform amplitude ratio of the direct P and reflected P410 phases on both short period and broadband recordings throughout the triplication, and 3) the abrupt termination of the short period P410 phase at 13.3°. These features are best modeled by a composite discontinuity in which a sharp velocity jump of 3% is overlain by a linear velocity jump of 3.5% spread over 14 km. The interference of energy turning in the diffuse and sharp portions of this discontinuity structure reproduces both the long and short period triplication range and the step-like behavior of the P410 short period amplitude, which cannot be reproduced with either a simple linearly diffuse or a purely sharp discontinuity. This composite structure produces a triplication range which depends on source frequency and has an apparent depth which depends on observation frequency. Additionally, this is the structure expected from mineralogical arguments for the α-olivine - β-olivine phase transition.

4.2 Introduction

The fine structure of upper mantle discontinuities provides basic constraints on chemical and dynamical models of the mantle. Premier among seismic imaging of these discontinuities is identifying the magnitude, sharpness (radial thickness) and topography (radial variability) associated with the velocity jump. The 410 km discontinuity is generally seismically inferred to have a P velocity change in the vicinity of 5-6% caused by the α olivine-β spinel transition (Neele (1996); Vidale *et al.* (1995); Ringwood (1969)), but the sharpness and extent of topography has remained less clear. Because the wavelength of body phases typically used to study the discontinuities is on the order of the length scale of the discontinuity itself, any conclusive seismic estimation of the fine structure of the 410 is made difficult by the apparent transition impedance and thickness potentially being as much a function of source spectral content as actual structure (Burdick and Helmbeger (1987); Helffrich and Bina (1994)). Reported thicknesses vary by up to a factor of 10, from 35 km under the central Eurasian craton (Priestley *et al.* (1994)) to 2-4 km under oceanic spreading centers in the Indian Ocean (Benz and Vidale (1993)). However, based on unequivocal 1 Hz underside reflections at near-normal incidence and localized topside reflections exhibiting the triplication range of a sharp discontinuity, there has arisen a consensus that the 410 must be, at least locally, less than 5 km thick (Neele (1996); Nakanishi (1988); Benz and Vidale (1993)).

The pressing difficulty with this estimate is that a sharp 410 conflicts with numerous studies of the equilibrium thermodynamic behavior of a primarily olivine mantle chemistry. For any reasonable mantle composition (Anderson (1989)), the $\alpha - \beta$ transition is expected to occur over a few 10's of kilometers in the vicinity of 400 km depth, and as improved laboratory results converge so too does the robustness of this estimate (Bina and Wood (1987); Katsura and Ito (1989)). Besides actual chemical layering in the upper mantle, the seismic conclusion of a sharp jump appears incompatible with anything other than a pure end-member olivine phase transition. Various mechanisms have been proposed to resolve this conflict, including a non-equilibrium,

propagating phase transition (Solomatov and Stevenson (1994)) or a 410 composed of both transforming olivine and chemical differentiation across the discontinuity (Anderson (1989)), but verification of any of these theories depends on identifying or constraining topography on the 410, which also remains unclear. Revenaugh and Jordan (1991) found anti-correlated 410 and 670 topography on the basis of multiple ScS bounces, whereas more recent studies have found slightly positive to no correlation, as inferred from P-to-SV conversions and long period SS precursors (Shearer (1993); Flanagan and Shearer (1998)). From laboratory experiments and thermodynamic calculations, it is expected on the basis of Clapeyron slope magnitudes that the 410 discontinuity should have more topography than the 670 km discontinuity (Bina and Helffrich (1994)), but seismically the opposite has been found (Shearer (1991); Flanagan and Shearer (1998)). In light of thermodynamic arguments for a more diffuse 410 structure, the difficulties introduced by wavelength dependent visibility, the lack of consensus regarding topography on the 410 and the fact that nearly all robust sharpness estimates have come only from oceanic settings, it is premature to conclude that the 410 is globally sharp.

In this paper we analyze a strong topside 410 reflection produced by the 04/14/95 event in western Texas, an event which produced a rare sampling of 410 structure through a continental corridor. We present evidence that the 410 discontinuity under the Southwestern US is probably not completely sharp. It is best modeled as a composite structure containing a sharp P velocity jump of 3% overlain by a gradational 3.5% transition spread over 14 km. Although there is ample thermodynamic evidence as to why the 410 might assume this type of structure, we reach this conclusion on purely seismological grounds by showing that a composite structure of this specific type is required to reproduce the triplication range and amplitude behavior found in the data, and that these features cannot be well modeled by either a simple sharp or linearly diffuse 410. We discuss in detail the mechanism by which such a composite structure reproduces the data, as well as factors unrelated to the 410 structure which might conspire to produce the data set from which our conclusion is drawn, and why we believe alternate explanations of this data are less likely. Finally, we show how

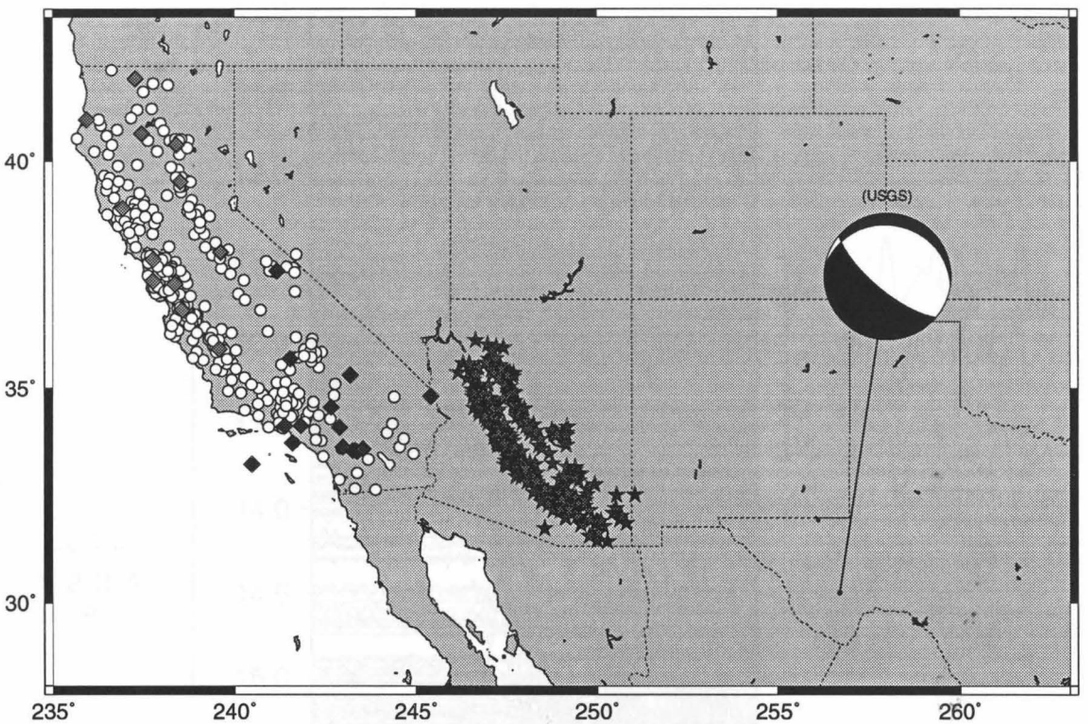

Figure 4.1: The data set recording the 04/14/95 West Texas earthquake (Ml 5.7, (30.24,-103.32,15km)) contains 394 vertical short period recordings from the USGS, Berkeley and Caltech arrays (white circles) and 28 broadband recordings (Diamonds) of which 24 are used in this study. 410 km discontinuity bouncepoints for all stations are shown with stars.

this class of composite discontinuities produces an unstable triplication range which depends on earthquake source spectrum.

4.3 Data

We utilized 394 short period traces from the combined arrays of the Southern and Northern California Seismic Networks and 24 broadband records from the TERRAscope, BDSN, LLNL and IRIS GSN networks which recorded the 14/14/95 Texas event. The source-receiver geometry comprises ray-paths with azimuths varying 24° from stations in southern and northern California. This geometry produces a variable bounce point ranging northwest through Arizona (Figure 4.1). The earthquake occurred along a normal fault with one conjugate plane having strike and dip of 308°

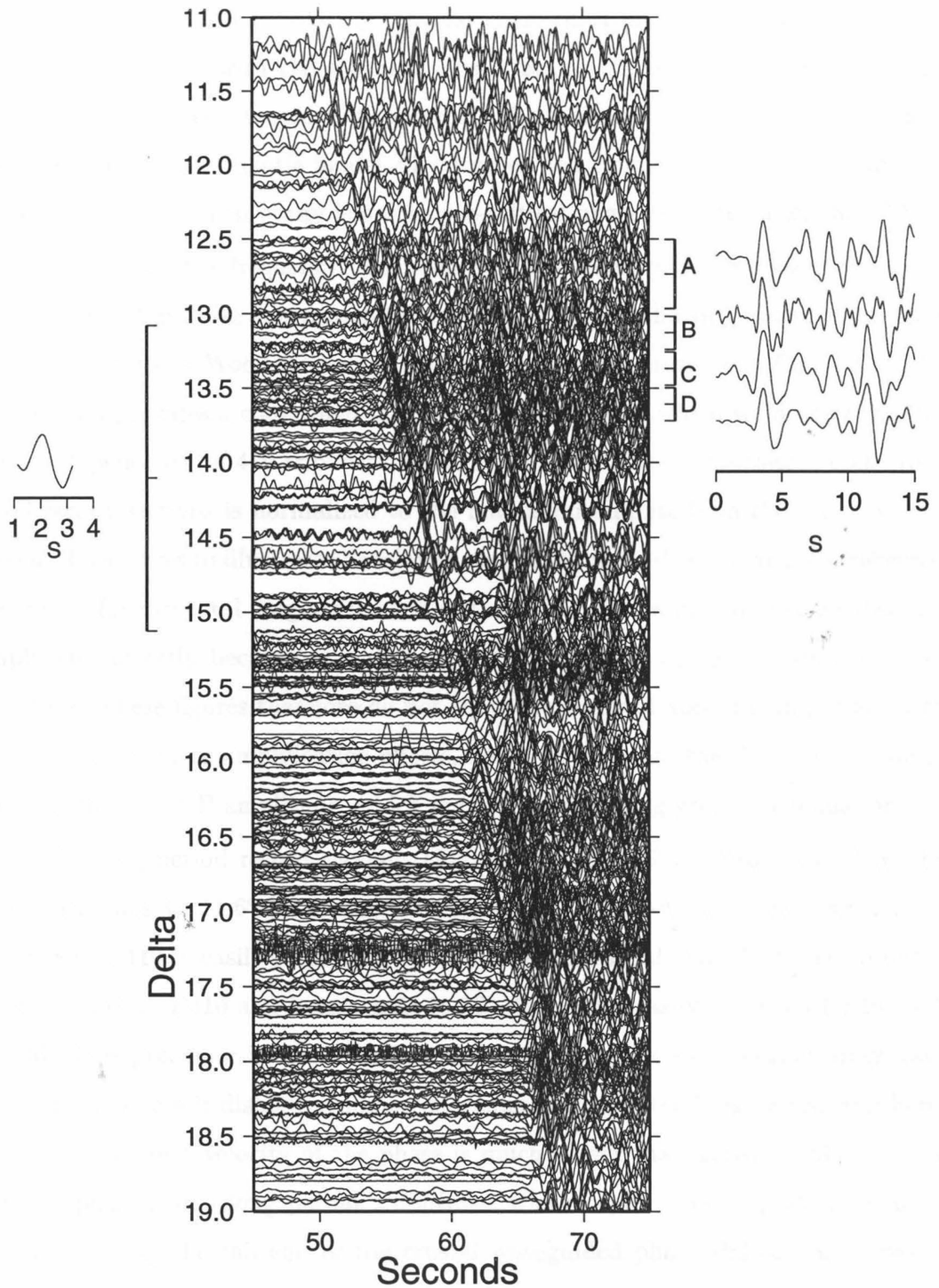

Figure 4.2: Short period vertical data plotted with reduction velocity of 10.5 km/sec. The 394 traces shown in this array are 1-hz lowpass filtered and normalized to the maximum amplitude in the window shown. The 410 reflection is clearly visible out to approximately 13 deg, where it rapidly disappears. This amplitude decrease is a primary constraint in modeling this data set. To the right of the array are the stacks of the data enclosed in the brackets (see text). To the left is the source time function used in generating synthetics; this consists of the stack of the 82 recordings between 13 deg and 15 deg.

and 37° NE (USGS, 1995), placing the west coast short period array well away from the radiation nodes, with the southern most stations (those nearest the source and most diagnostic of 410 structure) approaching the radiative maximum. As the critical distance of the upper mantle model T7 (Burdick and Helmbeger (1987)) is near 14°, most of the focus of this study is on the pre-critical phase arriving closer than 14°.

To investigate the frequency dependence of 410 reflectivity, we present the short period data after 1-Hz low-pass filtering (Fig. 4.2) and the broadband data after convolution with a Wood-Anderson long period (WALP) response (Fig. 4.3). The convolution provides a convenient spectral separation with which to identify the frequency dependence of 410-triplication range. Unless otherwise indicated, each trace in all record sections is normalized to the maximum amplitude in the time window shown. This serves to illustrate the relative amplitude of the direct P and 410-reflected arrivals, a fundamental diagnostic of this study. We choose not to analyze absolute amplitudes directly because of the strong dependence on the near-surface receiver structure. These figures therefore do not show the decay of absolute amplitude with distance or local site amplification effects, however, and cast the P410 amplitude in terms of the direct P amplitude, which may be experiencing greater attenuation.

In the long period record sections (Fig. 4.3), it is straightforward to follow the 410 phase back to 11.6° by tracing the phase with constant slowness inward from 14°, where P410 is easily identified. At 12.6° an additional arrival emerges roughly 4 seconds before P410 and is traceable to 10°, but is not easily mistaken for the 410 arrival. This precursor is also observed in the stacks of the short period array data (see below), where it displays a similar moveout to that of the long period seen here. Since the apparent velocity of the phase is much slower than apparent 410 velocity and the phase shows long period amplitudes which rapidly decrease with distance, it is most likely the tail end of the crustal waveguided phase Pnl and is therefore unrelated to 410 structure. However, it does appear to interfere with the 410 arrival at ranges between 14° and 16° in that there is a discernible phase shift in P410 through this range where the phases come together. Towards 16° the amplitude of Pnl appears to be sufficiently small to not perturb the P410 phase while near 14° Pnl

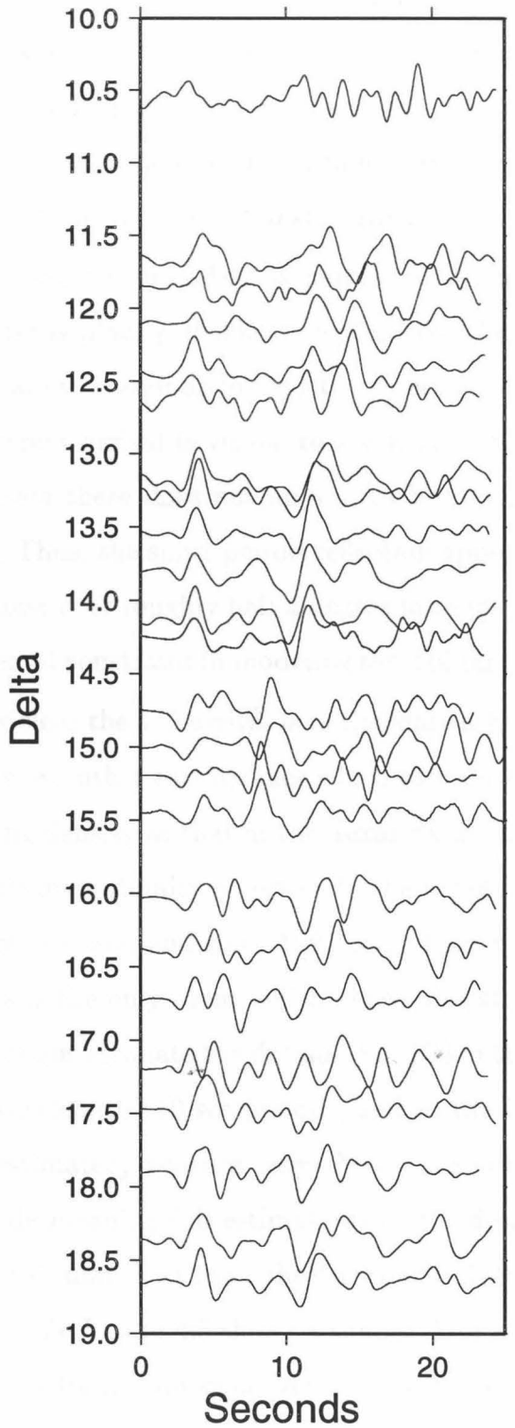

Figure 4.3: Wood-Anderson convolved broadband recordings. The P410 phase is visible out to 11.5 deg, or 2 deg further back than on the corresponding short period data. This is indicative of the short period triplication range being controlled by fine structure to which the longer period energy is insensitive.

does contribute. At still closer distances diagnostic of 410 structure (12°-14°), the precursor is sufficiently ahead of the P410 arrival that interference between the two phases is not an issue. The longer period energy is not particularly sensitive to fine structure of the 410 discontinuity, and so this data is primarily useful for constraining the total velocity jump across composite 410 structures.

The more diagnostic short period data is plotted with time reduced at 10.5 s/° (Fig. 4.2). The 410 phase is plainly visible emerging from the direct P at about 17° and by 14° is approximately 7 seconds behind the direct P. A simple estimation by eye suggests that a coherent arrival is visible to a distance of at least 13.5°, but not much beyond 13.0°, where there does not appear to be coherent energy above the background noise level. Thus, the short period reflection appears to stay strong until it disappears into the noise over roughly half a degree in range. This rapid amplitude loss provides a fundamental constraint in modeling the 410 reflectivity characteristics.

To demonstrate how clear the 410 arrival is in this data set, it is useful to compare the data with two of the few other earthquakes which contain a comparable short period instrument recording density as that in the Texas data. In general, events which produce a topside mantle discontinuity reflection in the range needed to diagnose discontinuity fine structure are rare, and since 1991 there have been only 6 candidates, of which the Texas data is the only event which allows fine structure estimation. As mentioned above, one cannot estimate the details of a 10 km thick structure by using a wave with a 90 km wavelength (10 sec period), and so the importance of regional events cannot be overestimated, because only these have sufficient high frequency energy which can provide meaning full estimations of the detailed structure can be made. Figure 4.4 shows similar data from the October 6, 1996, earthquake offshore Vancouver Island, BC, while Figure 4.5 shows a similar data set from the August 28, 1995, event near the tip of Baja California, Mexico. Both events are normal faulting events. As is typical for these types of data, a surface reflected phase, *pP,* appears 6-8 seconds after the first arrival, which, at 12° distance, is right where the 410 arrival is expected. Although the *pP* is easily identifiable from the lack of moveout, it is not a clean, sharp arrival and tends to be scattered over a couple wavelengths in its arrival

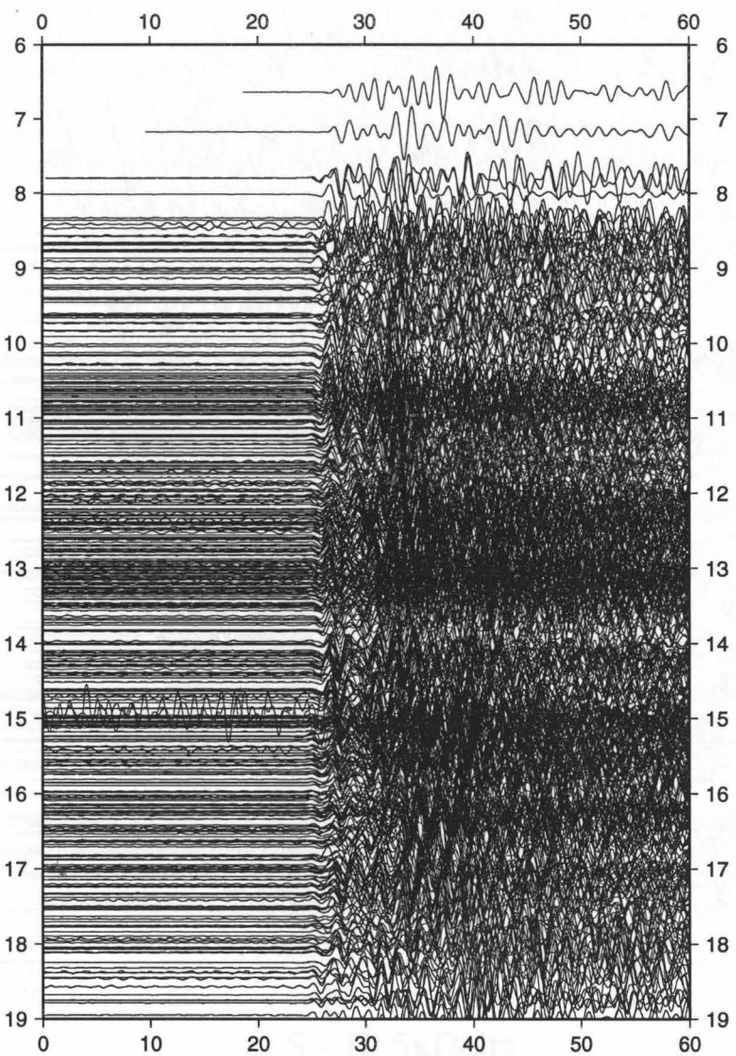

Figure 4.4: Vertical Short Period Data from the 10/06/96 Vancouver Island Event. The data is bandpass filtered between 2 and 0.5 seconds, and aligned on the first arriving P energy. Like the Texas data, this event has a normal fault mechanism but is located sufficiently deep that the surface reflected phase, pP arrives right on top of where the 410 arrival is expected. The interference renders the data useless for inferring 410 structure. Plotting the data at a reduced velocity does not increase the coherence of any of the discernible phases.

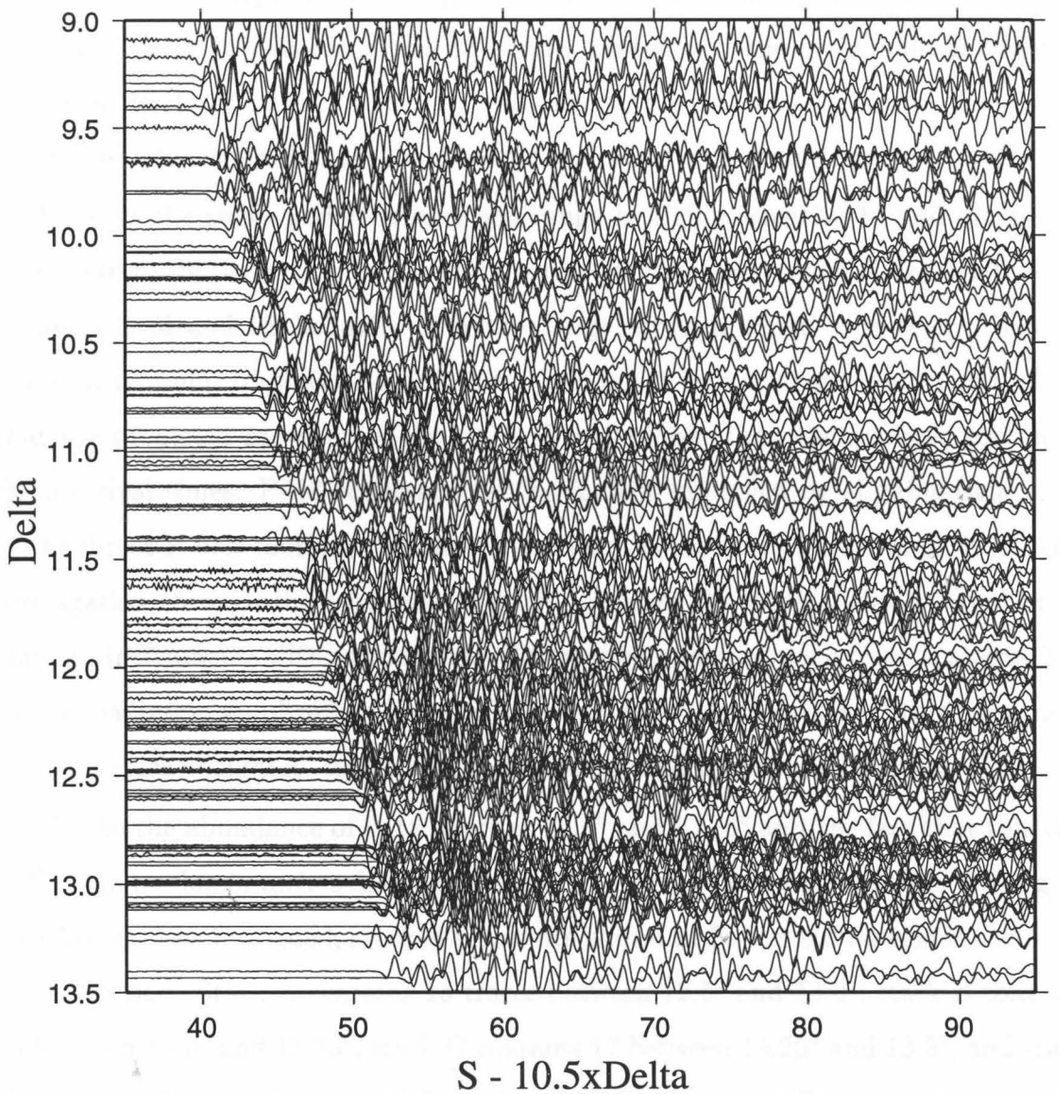

Figure 4.5: Vertical Short Period Data from 8/28/95 Baja California Event. The data is low pass filtered below 2 hz. Like the Texas data, this event has a normal fault mechanism but is located sufficiently deep that the surface reflected phase, pP arrives right on top of where the 410 arrival is expected. The interference renders the data useless for inferring 410 structure. The record section range is truncated to 13.5° because the Northern California Seismic Array failed to trigger and record the event.

time and therefore effectively swamps any 410 arrival within a degree or two of this range. However, identifying the triplication range to within a degree is crucial for identifying 410 sharpness, and so *pP* usually prohibits making any inference of 410 structure. *pP* is also visible in the Baja data, except here the event was shallower so the phase is closer to the direct P. In any event, the effect is the same. The Texas event was sufficiently shallow that the surface reflection is indiscernible from *P*.

Because the short period triplication range is highly sensitive to and diagnostic of 410 structure, it is crucial to tightly constrain the exact range of the P410 short period arrival and its behavior over the range through which it is seen. To that effect, it is useful to stack the data after binning it into segments sufficiently short that the predicted moveout of the P410 phase is lower than the intrinsic scatter in P410 arrival times. P410 coherence can be further improved by aligning each trace to the direct-P first motion; this effectively removes the static delays associated with propagation through the receiver-side crust. Because the vertical short period array employs instruments with substantially different gain factors, each trace is normalized by the maximum amplitude in the stack window before being stacked; this essentially avoids a stack 'weighted' in favor of instruments with higher gain factors.

Due to the abundance of data between 12.5° and 13.75° and the fact that this end of the triplication branch is diagnostic of discontinuity structure, we divide this region into 4 bins. The P-aligned, stacked traces are shown in Figure 4.2 alongside the main record section. Stack A contains 18 traces between 12.5° and 13.0°; stack B contains 15 between 13.0° and 13.25°; stack C contains 17 between 13.25° and 13.5°, and stack D contains 22 traces between 13.5° and 13.75°. Stacks C and D essentially duplicate what can be clearly seen by eye in the unstacked data- the direct P and reflected P410 phases dominate the stack and have comparable magnitudes. The spectrum of both arrivals is broadened due to the scatter in the large number of waveforms in the stack, but stacks with a smaller number of traces in this range reproduce the higher frequency (as well as dominating amplitude) of the arrivals seen in the unstacked data. Neither stacks A nor B show a P410 arrival clearly discernible above the noise. Particularly striking is the rapid disappearance of P410 between stacks C and B - in

the former stack it is the largest arrival while in the latter there is no positive-swing P410 energy visible above noise, despite the two traces having an average separation of only 28 km. The observable down-swing in stack B is most likely the vestigial P410 phase with a much lower amplitude. Stack A shows neither a strong P arrival nor a P410 phase where it should be observed, and has a high coda amplitude relative to direct P. This is most likely due to shadowing of direct P from the mantle low velocity zone (LeFevre and Helmberger, 1989) and crustal reverberations; the gradual lessening of direct P amplitude is also observed in the unstacked data in Figure 4.2. However, since the 410 phase is less affected by lid structure, it would still appear in (if not dominate) the stack if indeed energy were returning from the 410 at this range and the lack of a strong direct P phase in stack A would not preclude the observation of P410. There is some hint of an arrival approximately 1.5 seconds behind where one would expect the P410 phase to be arriving in stack A, but the amplitude of this arrival is not much above the coda, unlike in stacks C and D. One can also observe the P410 precursor observed in the long period data and discussed above; because of the distinctly slower moveout and decreasing amplitude, we believe this is the crustal phase P_{nl}. Given the questionable P410 signal on stack B, only the late and noise-saturated hint on stack A, and that the P410 arrival is not observable past 13.2° in the unstacked data, a primary constraint in modeling 410 reflectivity therefore is that the P410 arrival should not be strong at distances closer than approximately 13.2°.

It is instructive to point out how different the Texas short period P410 behavior is from other samples of topside reflections which have been used to infer a sharp 410, particularly the numerous Gulf of California events recorded on west coast networks. When it is seen, these events show a P410 arrival as far in as 10° which exhibits a gradual amplitude decay with closer distances, rendering them suitable for modeling with a sharp 410 (Neele (1996); Walck (1984)). The abrupt P410 termination shown in the Texas data, however, and the discrepancy of over three degrees in the short period triplication range between this and Baja events is highly suggestive of a P410 structure which is not necessarily sharp and displays regional variation.

4.4 Synthetics

From a modeling standpoint, the key features to reproduce are the frequency dependence of the triplication range, the constant P410/P amplitude ratio, and the abrupt short period cut off at 13.3°. The point of the synthetics is not to match every crustal reverberation associated with the source, which contains P, pP, sP, etc., but rather to model the reflective characteristics of the 410 km discontinuity by reproducing the basic behavior of the data. We use Generalized Ray Theory (Helmberger (1983)) to calculate synthetics for a host of one-dimensional velocity structures based on a modified version of the model T7 (Burdick and Helmbeger (1987)) (Fig. 4.6a which was derived from Californian earthquakes recorded across the U.S., including stations in Texas. This model adequately fits the differential travel times of the P, and 410 reflected phases, although it should be noted that the '410 km' discontinuity actually occurs at 393 km depth in the original model. Since the fine structure of the discontinuity affects triplication range much more strongly than its absolute depth, we do not perturb the absolute depth of the '410' in this model but continue to refer to the discontinuity as the '410' since that depth appears by recent estimations to be its rough average depth (Shearer (1991); Shearer (1993)). The Cagniard-de Hoop formalism includes density and shear structure only through their influence on the coefficients of reflection and transmission. The waveforms presented in this paper are therefore much more sensitive to the P-velocity structure than to density or shear structure (Gilbert and Helmberger, 1972).

The source time function used in the synthetics is shown in Figure 4.2; it consists of the first 2.4 seconds of the 82 short period waveforms from 13.5 to 15.5 lined up on the P arrival and stacked. While this source has a slightly longer period spectrum due to the stacking, the slight source red-shift will not seriously bias the reflectivity results for linear velocity models and is found to give substantially the same results as individual traces for the composite (non-linear) velocity models.

Due to the precedent set by other studies which have shown the 410 to be sharp, it is appropriate to first evaluate the suitability of models containing a sharp 410.

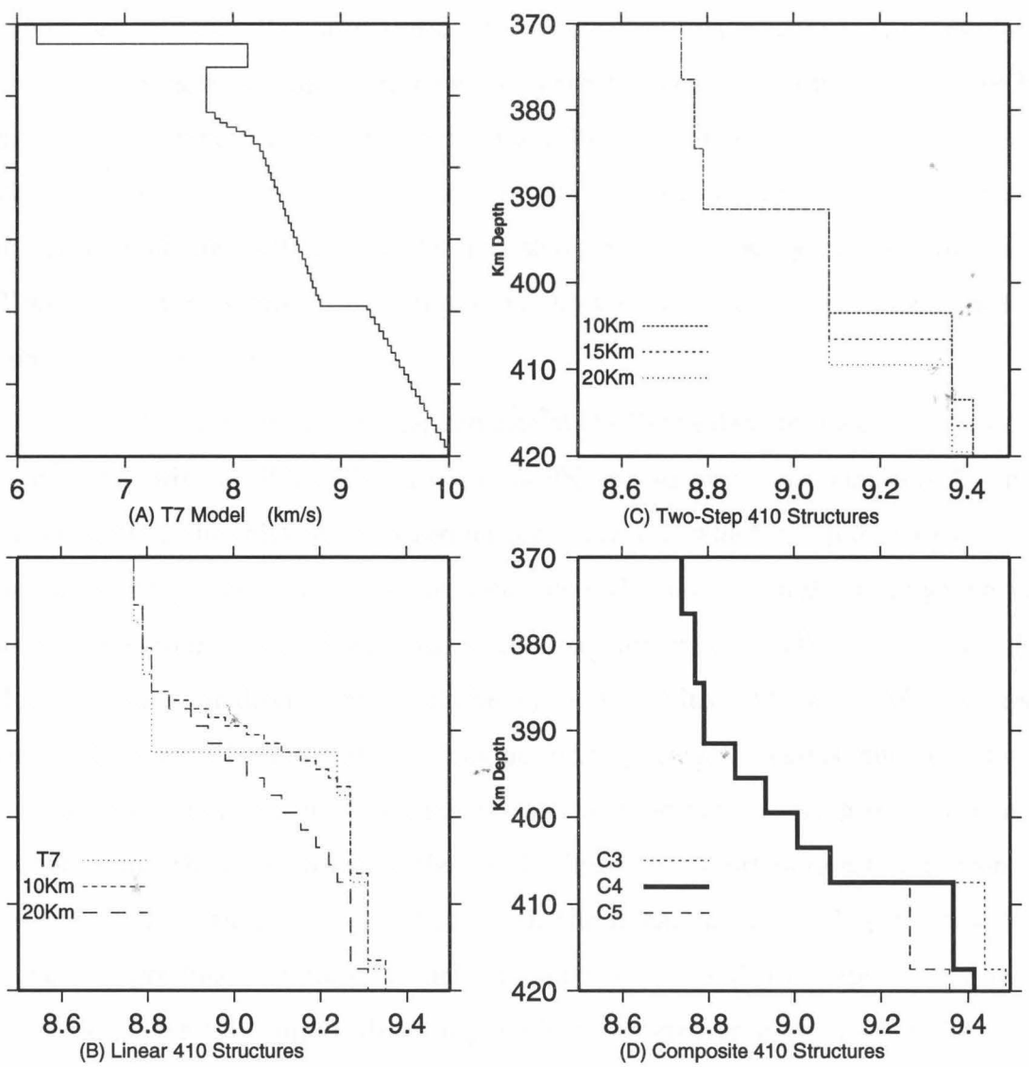

Figure 4.6: A) The upper mantle P-velocity model T7, derived for California events recorded across the western US, including stations in Texas. B) Linear 410 discontinuity gradients with a 5.5% velocity jump. C) Double 410 structures. D) Composite 410 structures consisting of a gradient overlying a sharp offset. The preferred model is labelled C4. Short period record sections for the models shown in B, C and D are shown in Figures 5, 7, and 8, respectively. Long period synthetics appropriate for Figure 4.3 appear in Figure 4.8.

We then gradually increase the thickness of the 410 discontinuity to explore the suitability of linearly diffuse structures. Physically, for the same incidence angle and frequency of energy, the effect of thickening the discontinuity is equivalent to lowering the relative impedance at that frequency across the discontinuity. Since the apparent impedance scales roughly with wavelength for discontinuity thicknesses comparable to the wavelength of the incident energy, increasing the discontinuity thickness preferentially lowers the short period reflectivity relative to the longer period energy. Figures 4.7a-c show short period synthetic record sections for the three linear discontinuity structures shown in Figure 4.6b, which have thicknesses of 0, 10 and 20 km. It is evident in these profiles how the thickness of the transition controls the die-off rate of the P410 amplitude. The sharp model is clearly inappropriate for the Texas data; the synthetic P410 phase on short record section is strong back to 11°, contrary to the data.

Taken alone, the frequency dependence of the Texas data triplication range can be reproduced with a diffuse discontinuity of 6% spread over approximately 20 km; the uncertainty in the thickness is based on the criteria by which one judges exactly where on the short period synthetics the decaying P410 phase would no longer be visible above background noise. By setting some detection criteria, a frequency-dependent 3 degree triplication discrepancy could be reproduced with a diffuse model. As is readily seen in Figures 4.8a and 4.8b, the long period triplication range is much less modified by the discontinuity thickness than is the short period, allowing one to identify a discontinuity thickness which preferentially limits the short period triplication range over the long period. The drawback with the linear models of Figure 4.6a is that none can produce the step-like behavior of the Texas P410 amplitude, where the reflected phase has amplitudes comparable to or greater than that of the direct P throughout the range where P410 appears. Instead, the synthetics for any linearly diffuse structure show a gradual amplitude decay with range relative to direct P but cannot produce an abrupt P410 termination. The class of linear discontinuities (particularly sharp ones) is suitable for some studies of the Gulf of California events but is inadequate for the Texas data.

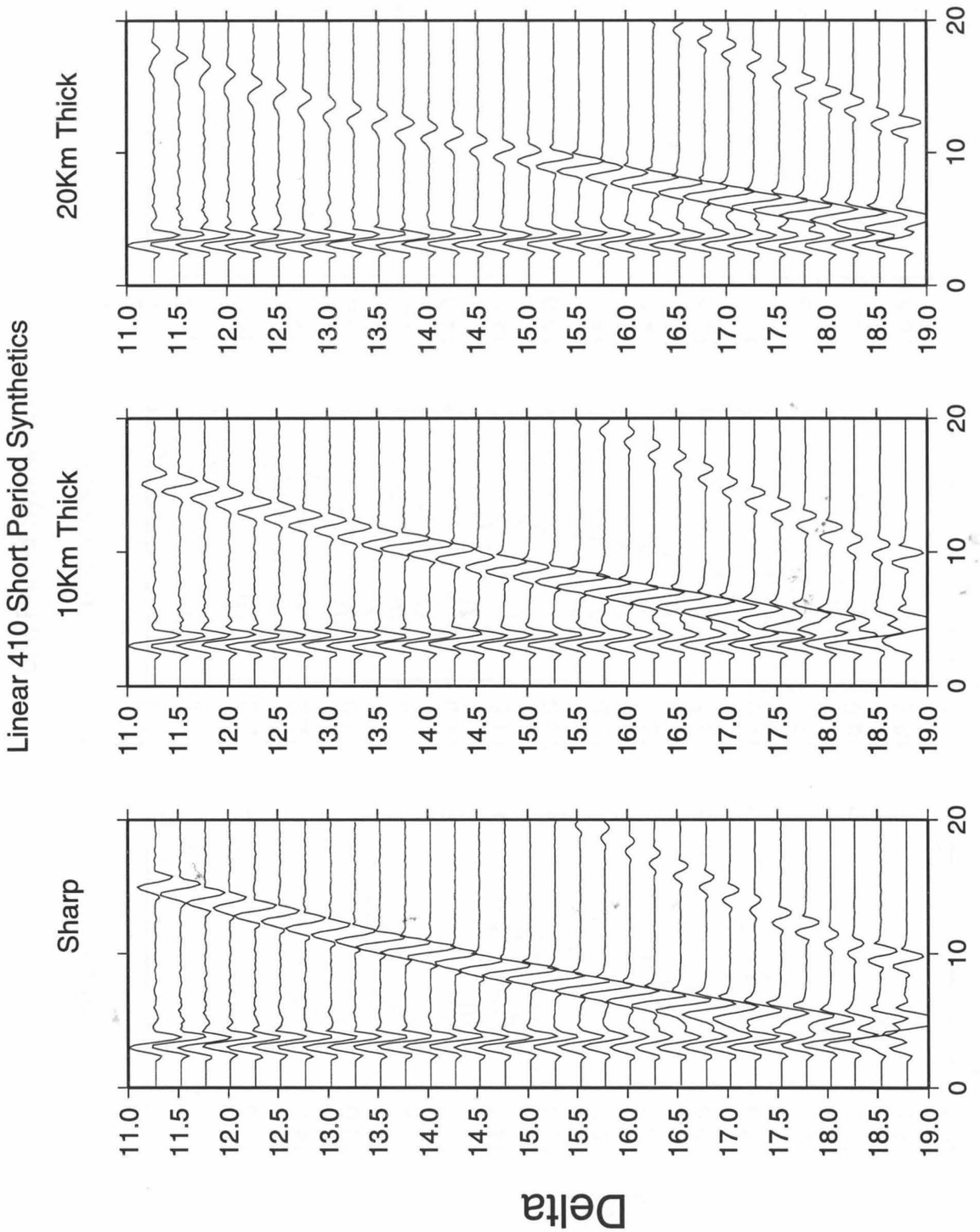

Figure 4.7: Short period synthetics for linear 410 gradients. A) A sharp offset causes the 410 reflected phase to appear strongly as far back as 11 deg, which is clearly inappropriate for the Texas data. Increasing the thickness to 10 km (B) or 20 km (C) lowers the overall short period impedance preferentially over the long period (Fig. 6) but cannot produce the very rapid cutoff of P410 amplitude seen in the data.

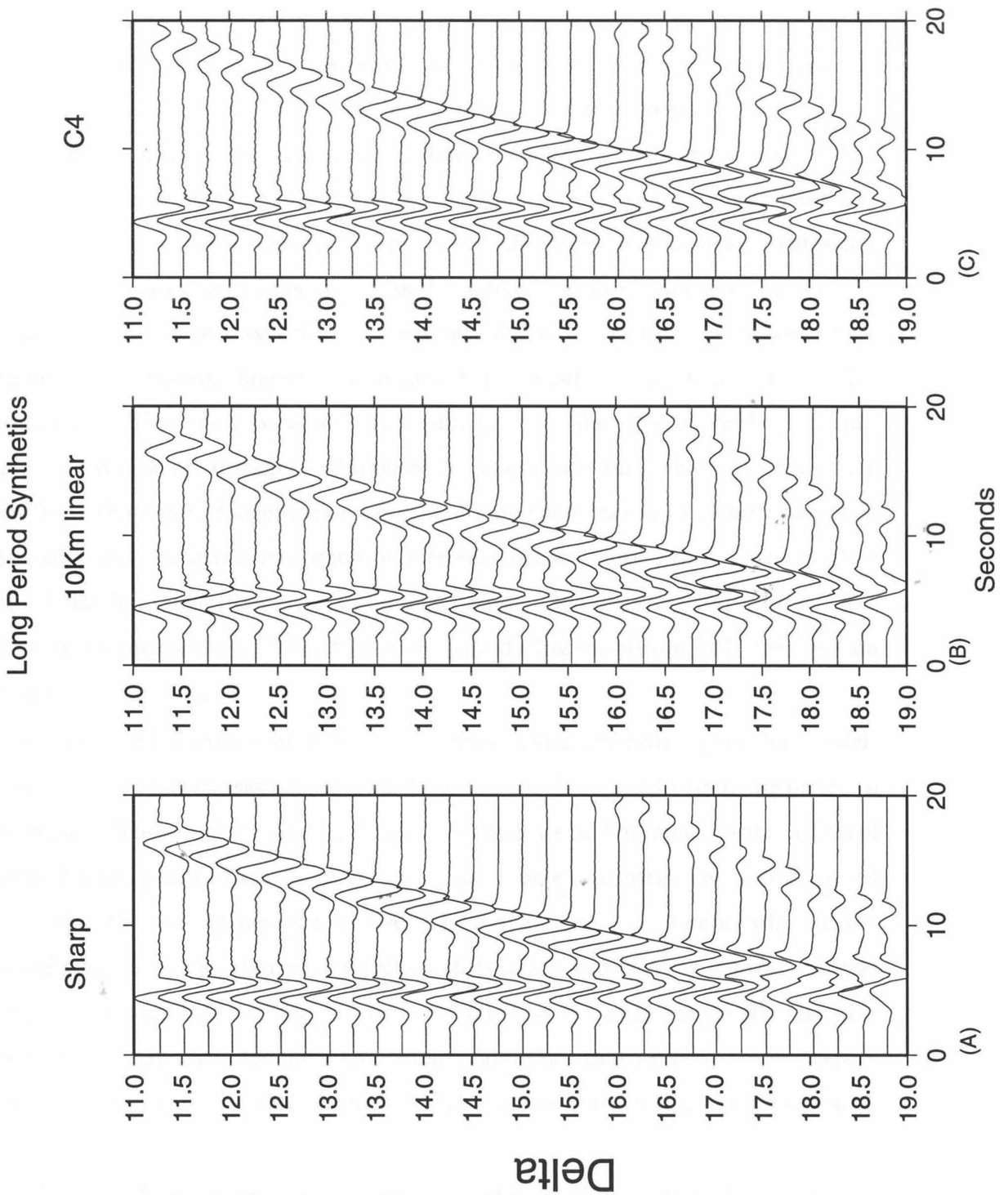

Figure 4.8: Long period synthetics for A) a sharp 410; B) a 10 Km thick linear gradient, and C) our preferred composite model, C4 (Fig. 4d). The long period energy averages over discontinuity fine structure and therefore has a much more stable triplication range which depends primarily on the net jump across discontinuity. Therefore, it is primarily of use in quantifying total velocity jump across the 410.

A nonlinear decay of P410 amplitude with distance can be produced by introducing fine structure into the discontinuity, which allows energy reflected from discontinuity substructures to interfere. The type of interference depends on the wavelength, angle of incidence, and physical dimensions of the 410 substructures. The reflection of high incidence-angle (greater source-receiver distance) energy interferes constructively, essentially because energy traversing different 410 substructures has closer travel times at larger distances. As the source-receiver distances lessens and the separate substructure travel times increasingly differ, the two energy packets (containing the same source function) separate in time, causing a transition to destructive interference. This effect is capable of producing rapid decrease of the P410 amplitude over very short distances. Therefore, to find a structure which can reproduce the Texas short period triplication range and amplitude means to identify the class of discontinuity substructures whose interference is constructive throughout most of the triplication range (thereby maintaining a strong, non-decaying P410 arrival) but which turns destructive near 13.2° (thereby reproducing the abrupt P410 termination identified in the data).

We explored a variety of 410 substructures before narrowing plausible models down to two simple classes between which we feel the data has the resolving power to distinguish. These include double, sharp discontinuities and different permutations of partly diffuse, partly sharp substructures. The double discontinuities were explored by varying the spacing between and velocity change across the jumps, while in the second class of models different transition thicknesses and velocity contrasts across sharp jumps were tested. Figures 4.6c and 4.6d show the most seismically plausible discontinuity structures for the double-jump and diffuse-sharp substructures, respectively, and their corresponding short period profiles are found in Figures 4.9 and 4.10.

The class of structures containing two distinct steps (Fig. 4.6c) produces the transition to destructive interference at a distance which depends more on the spacing between the two jumps then the actual velocity contrast across the jump. With a separation of 20 km (Fig. 4.9a), the P410 amplitude starts to drop off around 14.75°

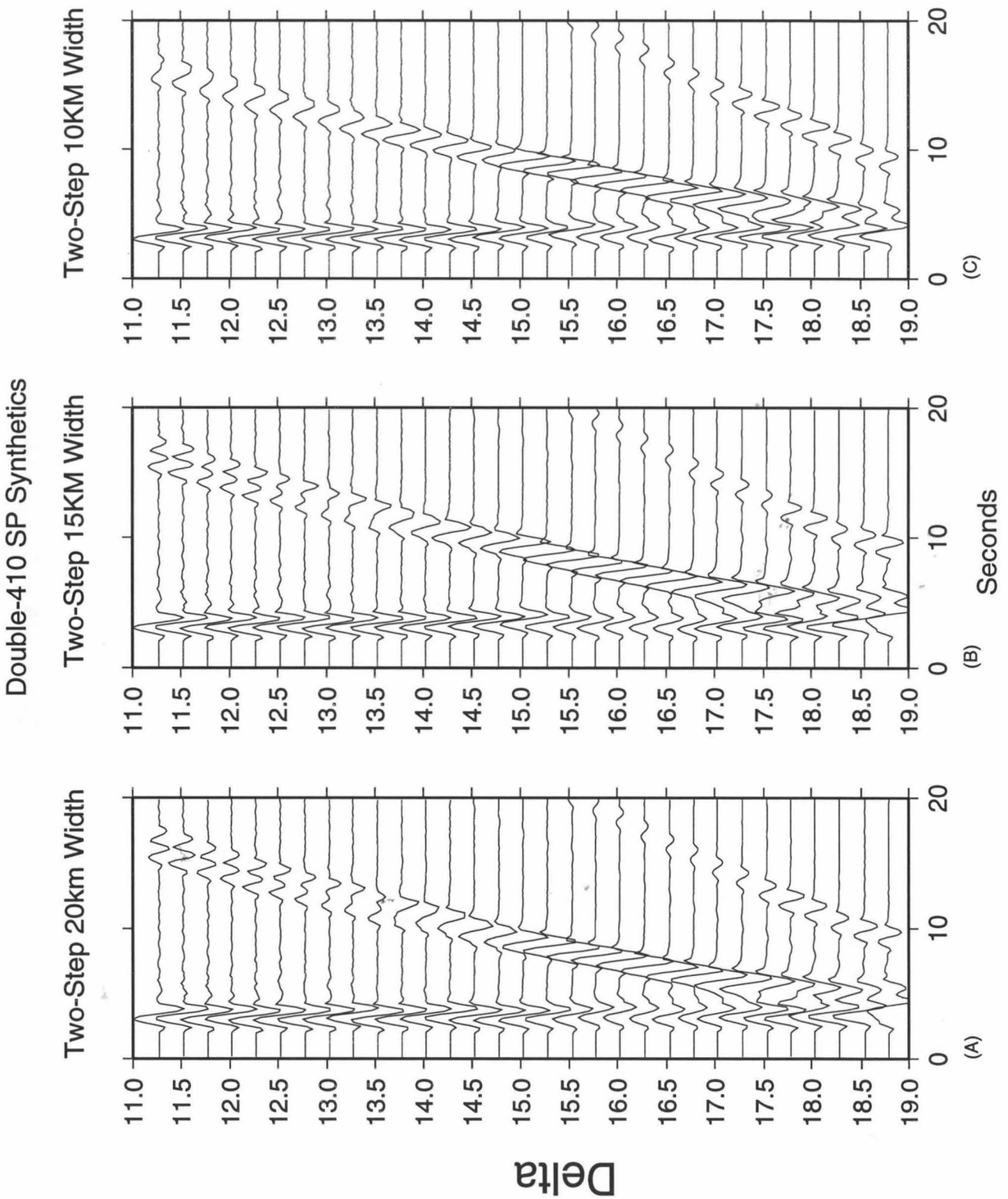

Figure 4.9: Short period synthetics with 20, 15 and 10 km thicknesses corresponding to Fig. 4c. These models can produce rapid decay of P410, with an onset controlled by the spacing between the velocity jumps. However, these models produce a broadening and splitting of the P410 phase not observed in the data.

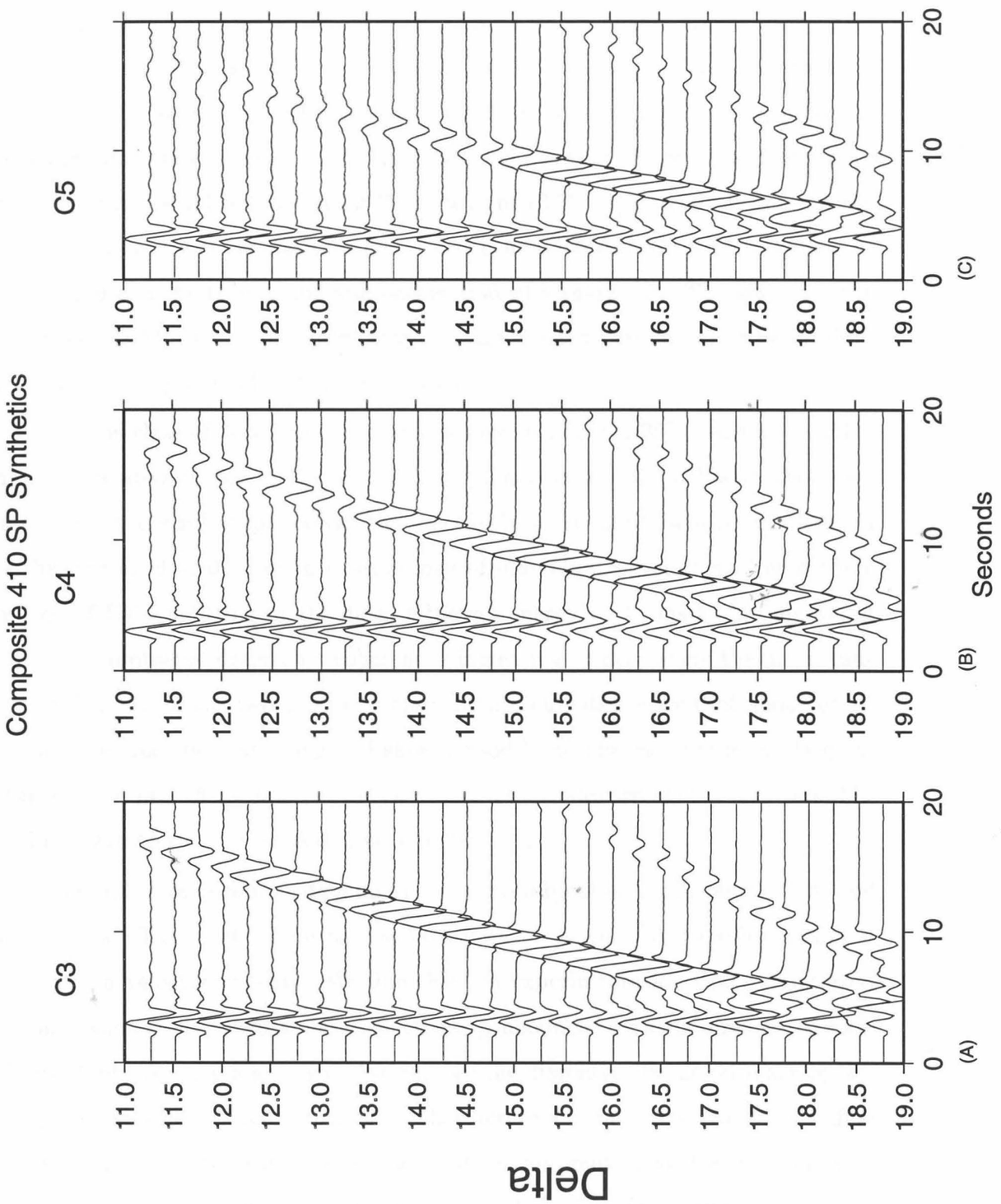

Figure 4.10: Short period synthetics for composite discontinuity models consisting of a fixed gradient with a variable sharp step (see Fig. 4d). The gradient dimensions were found by trial and error to maximize the interference of energy turning in this portion of the model with energy returning from the sharp region of the 410. The best fit to the data is achieved by (C4), which contains a 3% velocity jump over 15 Km. This produces a 56% decrease of P410/P amplitudes ratio over .5 deg and maintains a strong P410 amplitude at further distances.

and progressively broadens its shape until it splits into a double arrival near 13.5°. Inwards of 13.5° the arrival is clearly split and near 13° has roughly half the amplitude of direct P but rebounds slightly inwards of 12.5°. A 15 km separation (7b) produces nearly the same profile except the P410 broadening begins a degree closer in distance (13.75°) and phase splits apart at 12.75° instead of 13.75°. Progressively moving the double discontinuity closer together (Fig. 4.9c) causes the discontinuity to appear as a single step and the triplication approaches that of a sharp 410. Therefore, we can discard double 410 structures which have spacing less than 10 km, as these produce a triplication range extending too far inwards.

While this class of two-step discontinuities can produce a 35% decrease in P410 amplitude relative to direct P over a relatively narrow range (.5°) with the onset determined by the sub-step spacing, the spectral broadening of P410 is not observed in either the stacked data or in observations of individual waveforms. Nor is there any sign of P410 splitting in the data, although energy with this amplitude might be difficult to observe despite its coherence. Increasing or decreasing the magnitude of the either one of the two jumps to more than a cumulative total of about 6% is not viable because both the long and short period P410 phases become too large at distances near 14°- 15°, where both P and P410 amplitudes are readily ascertainable. For these reasons we rule out a double 410 structure.

The second class of composite models contain combinations of linearly diffuse and sharp offsets. The most viable models are those in which a sharp substructure is overlain by a velocity gradient. We find through experimentation that the interference phenomenon described above is much less pronounced for structures which have a sharp offset overlying a gradient. We explore the discontinuity model space by adjusting the percentage jump across each substructure and the thickness of the diffuse portion, keeping the total jump over the whole discontinuity near 6% in accordance with the amplitude constraints provided by the data at further distances. Increasing the jump across the sharp portion of the discontinuity serves to extend the triplication range and lessen the overall effect of the interference (Fig. 4.10a-c), as does thinning the diffuse portion of the non-sharp substructure. In contrast, lowering the

sharp offset and thickening the diffuse part both decreases the triplication range and increases the interference such that the P410 amplitude decrease behaves much less linearly. Given these tradeoffs, our preferred model is shown in Fig. 4.6d (labeled C4), which consists of a gradient of 3.5% spread over 14 km directly overlying an additional sharp discontinuity of 3%. The short period synthetics for this model are shown in Fig. 4.10b. This model produces a 46% loss of P410 amplitude relative to direct P over .25° and 56% over 1.5°, and additionally does not produce the strong splitting or spectral broadening of the double-discontinuity models. There is a slight rebound of the amplitude near 12.75° but only by about 10%. Intriguingly, this rebound occurs at the same distance as the stack (A) which shows the hint of P410 re-emergence, while the lowest synthetic amplitude at 13.25° corresponds in distance to the stack (B) which has no P410 arrival. Furthermore, at and beyond 13.5° the synthetic P410 has nearly constant amplitude relative to direct P. This model, therefore, reproduces what we identify to be the most important aspects of the Texas short period data set and is unquestionably more appropriate than a sharp or linearly diffuse 410 discontinuity structure. The long period synthetics appropriate for this model are shown in Figure 4.8c.

4.5 Interpretation

The composite model advocated in this study inherently predicts a highly frequency dependent triplication whose range and P410 amplitude depend not only on the spectral band of observation but the source time function as well. Via the interference phenomenon described above, two earthquakes with comparable source-receiver raypaths, magnitudes and mechanisms but different sources would show different triplications despite sampling the same region along the 410 discontinuity. This source dependence might explain the variable visibility of topside 410 reflections; in one of the most complete studies, Walck (1984) found observable P410 arrivals in roughly half of the Gulf of California events recorded in Pasadena which sampled similar regions of the 410 discontinuity. This structure also implicitly generates an ambiguous

depth and reflection coefficient which depends on the frequency of observed energy. At longer periods the discontinuity will appear shallower and with a greater net velocity jump because energy is effectively turned by both the diffuse and sharp portions of the structure, whereas shorter period energy (1Hz) will preferentially sample only the sharper portion located 10-15 km deeper than the top of the diffuse portion (Burdick and Helmbeger (1987); Helffrich and Bina (1994)).

Although our analysis does not allow us to distinguish between different petrologic models, a 410 km discontinuity structure of the type advocated here could be produced by either a single or multi-component phase transition. In the former, our type of composite 410 phase change is theoretically expected from equilibrium thermodynamic calculations of the $\alpha - \beta$ yield profiles. These show that most of the transformation occurs in a narrow interval near the boundary of the phase loop (Helffrich and Wood (1996); Stixrude (1997)), effectively producing a gradient which progressively steepens into a sharp offset. In the latter, the $\alpha - \beta$ olivine phase change superimposed on the broader pyroxene transitions could produce a composite velocity discontinuity marked by linear gradients and sharp offsets (Anderson (1989)). In either of these cases strong regional variation in 410 triplication behavior is expected given the strong dependence on temperature and chemistry of such a composite discontinuity.

Since the sharp portion of this study's composite structure will always reflect short period energy, it is not inconsistent with previous studies which have inferred a sharp 410 under oceanic spreading centers (Walck (1984); Nakanishi (1988); Neele (1996)), the central Indian ocean (Benz and Vidale (1993)), and Basin and Range (Vidale *et al.* (1995)), particularly since the P'P'-precursor observations do not provide discontinuity reflection coefficients. The 410 discontinuity in the majority of previous studies underlies oceanic environments and there is a body of evidence suggesting that the thermal and chemical differences between oceans and continental cratons extend into the transition zone (Gossler and Kind (1996), Polet and Anderson (1995); Jordan (1975); Sipkin and Jordan (1976)), although a consensus on this subject has not yet been achieved (Flanagan and Shearer (1998)). Gossler and Kind (1996) find a

positive correlation of differential travel times between SS precursors and continents and oceans, from which they infer that the sub-continental transition zone is on average 14 km thicker than sub-oceanic. The opposite sign of the Clapeyron slopes for the phase changes usually associated with the 410 and 660 km discontinuities (Helffrich and Bina (1994)) allows this result to be most easily explained by cooler sub-continental transition zone temperatures of on average 100 K. Regional variation on a much shorter lateral scale length has also been documented by Dueker and Sheehan (1997), as well as in high resolution regional tomography models (Humphreys and Dueker (1994)). Given that the 410 bounce points of this study lie within a continental corridor adjacent to the stable (and presumably cool) Colorado Plateau, and that the only other study of comparable resolution to this one found a 35km thick 410 transition beneath Eurasia (Priestley *et al.* (1994)), there is adequate reason to think that sub-continental 410 structure should differ in its overall form from sub-oceanic environments.

4.6 Discussion and Conclusions

Perhaps the largest unknown in our model formulation is our inability to quantitatively assess the potential impact on the P410/P amplitude ratio of differential attenuation along the two paths under the tectonically active Western United States. Systematically greater attenuation of direct P caused by relatively lower Q along shallower paths would keep the recorded P410/P ratio artificially high throughout the array and could potentially mask a linear drop-off of P410 amplitude. However, such attenuation would not produce the abrupt P410 cutoff, which is the primary constraint in modeling the data. Therefore, the ultimate effect of not modeling attenuation would be a mis-appraisal of the total velocity change across a composite 410 but would not alter the result that such a composite structure is required to produce the abrupt termination of P410.

The mantle low velocity zone (LVZ) could also have a significant impact on the P410/P amplitude ratio on both a regional and local scale. Profiles of explosion data

from NTS recorded in west Texas indicates that P emergence from the shadow zone occurs near 12° (Helmberger, 1978), thus causing any diffracted arrivals detected here to be lowered in frequency and amplitude. We argue that the P410/P ratio drops off quickly with decreasing distance; therefore, if the shadow zone is heavily impacting the ratio by lowering the P amplitude, then the P410 amplitude must be *decreasing* even faster so as to still lower the ratio as observed. Thus, the main observational constraint is only bolstered by the regional P interaction with the LVZ.

It is also possible that strong lateral variation in the LVZ is perturbing the P410/P ratio across the array, in particular because energy arriving at closer stations misses the Colorado Plateau while that arriving at further stations traverses it. While we can't rule this possibility out, a fan plot (time vs azimuth) of the same short period data shows substantially the same behavior of the P410/P ratio as the bounce points move across the margin of the Colorado Plateau, implying that azimuth (and therefore LVZ lateral variation) is not the cause of the ratio decrease and pointing to the 410 km discontinuity as the source of the phenomenon.

Finally, another possible interpretation of the frequency dependence of triplication range seen in the data is that the 410 under the Colorado Plateau is in fact sharp but is strongly laterally varying in a two-dimensional sense, causing wavelength-dependent defocusing. Given the transitional nature of the surface tectonics, the above arguments for petrologic differences extending into the upper mantle, and SS-precursor studies which show variable depths of upper mantle discontinuities (Flanagan and Shearer (1998)), this is a distinct possibility. However, it is also quantitatively untestable without additional, orthogonal ray-paths recorded on arrays with station density comparable to that presented here.

Ultimately, for the data analyzed in this study, the 1-D, composite model suffices to explain the gross features of both the short and long period P410 reflection without needing to invoke a more complicated structure. That the model possesses the basic velocity structure expected from petrologic arguments makes it all the more compelling. It is ominous, however, that only the extremely high station density allows identification of this structure and suggests that the true 410 structure can be easily

dden by limitations in either observation density or spectrum.

4.7 Acknowledgments

This research was supported by National Science Foundation grant # NSF EAR-9316441 California Institute of Technology, Seismological Laboratory Contribution #6201.

Chapter 5 The Broadband Structure of the East Pacific Rise Axis

5.1 Abstract

We model whole seismograms containing triplicated S, SS, and SSS to infer systematic variations in upper mantle structure along the East Pacific Rise. Recordings on west coast broadband arrays of five transform events form a continuous record section from 8° to 82°. We find that there is no discernible variation in Transition Zone structure over great distances (~1000 Km) orthogonal to the ridge axis, which implies that the East Pacific Rise is not supplied directly with local lower mantle material. In the shallowest mantle, there is evidence of systematic growth of a high velocity zone, or Lid, with distance from the ridge axis. Along the EPR crest, the 1-D model Tectonic North America (Grand and Helmberger (1984)) modified with a 7 Km thick crust accurately predicts the relative arrival times of the individual triplication branches, but increasingly off-axis energy requires a progressive thickening of the Lid, culminating in a 3.5% velocity increase over 150 Km laterally within the upper 70 Km of the mantle. For raypaths near the Gulf of California, there is no correlation of the lateral boundaries of this Lid with the Baja peninsula, indicating that the surface expression of the peninsula is not simply related to the uppermost mantle velocity immediately below it. For raypaths lying far offshore, the Lid influences the relative amplitudes of the triplicated multiple S phases. Together these show that the Lid forms rapidly near the ridge axis but continues to evolve outside of the immediate vicinity of the axis.

5.2 Introduction

The details of mass transport near oceanic spreading centers has formed a central geodynamic constraint on the scale of mantle convection and mantle layering. Geochemical models of how melt is transported from the distributed production region to the narrow zone of crustal formation along the ridge axis have proved inconclusive, and whether mid-ocean ridges comprise the surface expression of whole mantle convection remains particularly undetermined. However, competeing models of material transport to oceanic ridges should be seismically testable, because systematic lateral variations in temperature will be reflected by variation in discontinuity depth. A lower mantle upwelling into a purely peridotite upper mantle, for instance, can produce a lateral temperature variation away from the ridge axis on the order of 600°/1000 Km, which in turn will cause a thickening in transition zone thickness on the order of several tens of Km (Anderson (1989)). Other recent calculations indicate that the 410 phase change, for example, should increase in thickness 15 km for a temperature change of 215-245 $C°$, while estimates of the relevant Clapeyron slopes indicate several radial shifts on the order of 10 Km as well Helffrich and Bina (1994). If spreading centers are active features which overlye the upwellings of whole mantle convection, discontinuity depth variations near the ridge crests will be easily discernible because the interference of the triplication branches are sensitive to transition zone structure. As shown in Figure 5.1, at given ranges, each particular S multiple is triplicated by reflections from upper mantle velocity discontinuities. The discrete sub-phases of each triplicated arrival show an average velocity at that turning depth and can therefore be modeled to infer the details of transition zone structure. For triplicated multiple S , the time separation of the individual branches is correspondingly greater by a factor equal to the multiple, e.g., 2 for SS , 3 for SSS , and so on, rendering the discrete sub-phases much easier to identify.

The East Pacific Rise (EPR) is uniquely suited for constraining mantle discontinuity depths due to the abundant seismic coverage of the western United States. Dense deployments of broadband seismometers stretch from the Mexican to Canadian

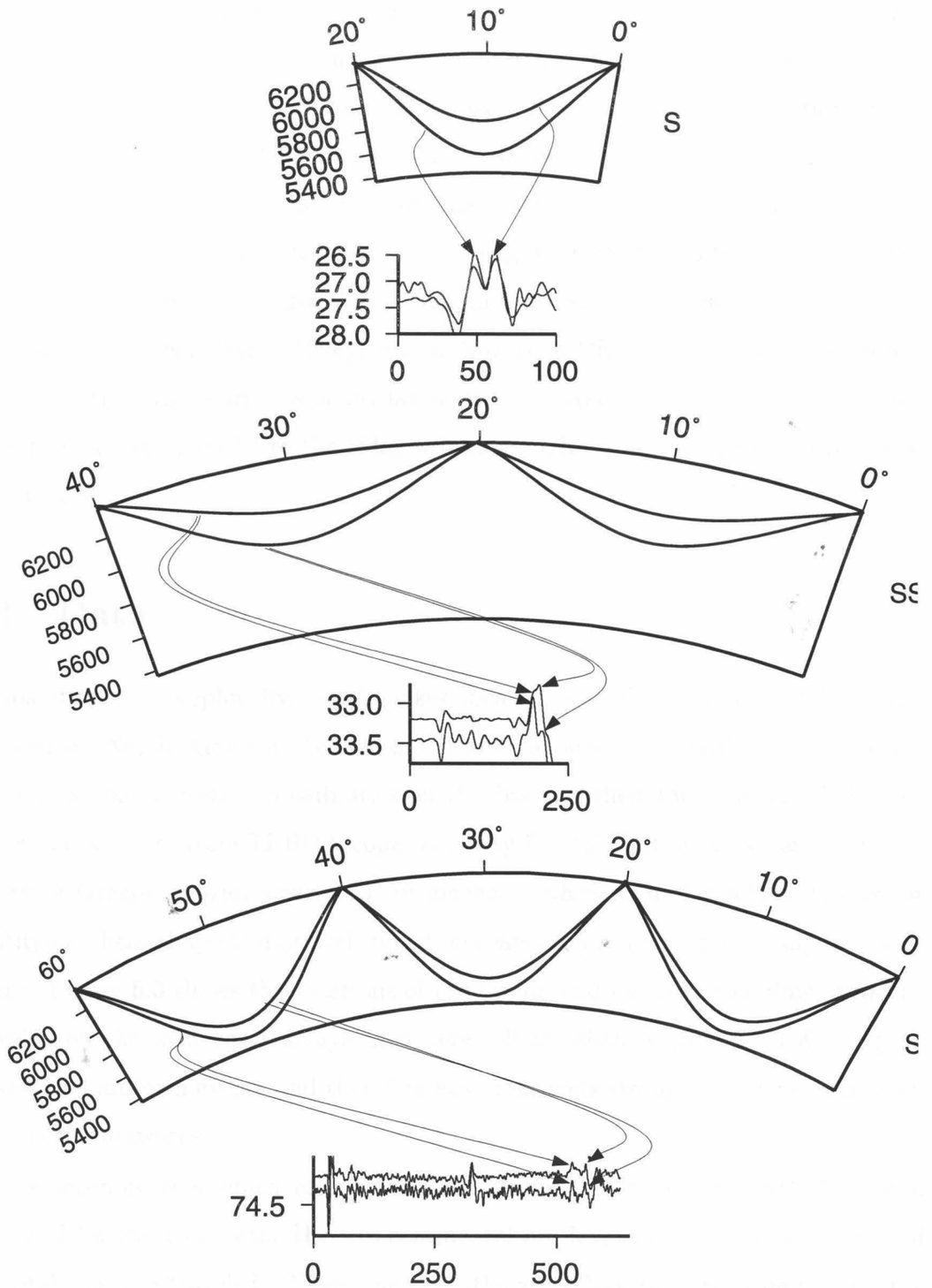

Figure 5.1: Schematic of raypaths appropriate for the various triplicated multiple-S phases discussed here. We refer to the branches as single arrivals but in fact they are formed by the two geometric arrivals. For the model Tectonic North America, the S phase is composed of branches A (rays turning in the Lid) and C (rays turning in the vicinity of the 410 Km discontinuity), which cross near 18°, while branches C-D and E-F(rays turning near and below the 670 Km discontinuity) cross near 22°. For *SS* and *SSS* the crossings are double and triple, respectively, of that for *S* .

borders, and seismic energy traversing north-south directions generate single source record sections with extensive and identifiable phase move out which allow unambiguous identification of the discrete sub-phases. Systematic lateral variation in the upper mantle near the East Pacific rise should be readily identifiable with a judicious choice of events with raypaths which propagate at different average distances from the ridge axes. These individual raypaths propagating parallel to the ridge will have high resolution of ridge-orthogonal variation, in contrast to tomographic images of the East Pacific Rise (eg, Grand (1994)), which show the EPR as a broad, slow region but cannot constrain the sharpness of any lateral velocity gradients. These individual raypaths propagating parallel to the ridge will have high resolution of ridge-orthogonal variation.

5.3 Data

In this study we employ five earthquakes located near the East Pacific Rise and recorded on North American broadband seismic arrays. The earthquakes were selected from the abundant possibilities on the basis of their location and SNR. For each event, stations from TERRAscope, Berkeley Digital Seismic Array, and the University of Oregon provide nearly 13° of moveout, which is highly advantageous for identifying phase shape and arrival time discrepancies for energy containing the same source. Figure 5.3 shows the locations of the events and the corresponding raypaths recorded on the west coast arrays used here; all are shallow (about 10 Km depth) strike-slip transform events and therefore have relatively strong shear wave radiation towards the networks.

The seismometers which record the data are located near the North American coast and for most raypaths the sub-continental arc length is a small percentage of the total distance traveled. Where the raypaths are sub-oceanic they lie nearest the ridge axis for the closer events and propagate progressively further from the axis for the more distant events. However, the great circle path for the raypaths from the most distant event (at ranges 70° -82°) actually crosses the ridge about a third of

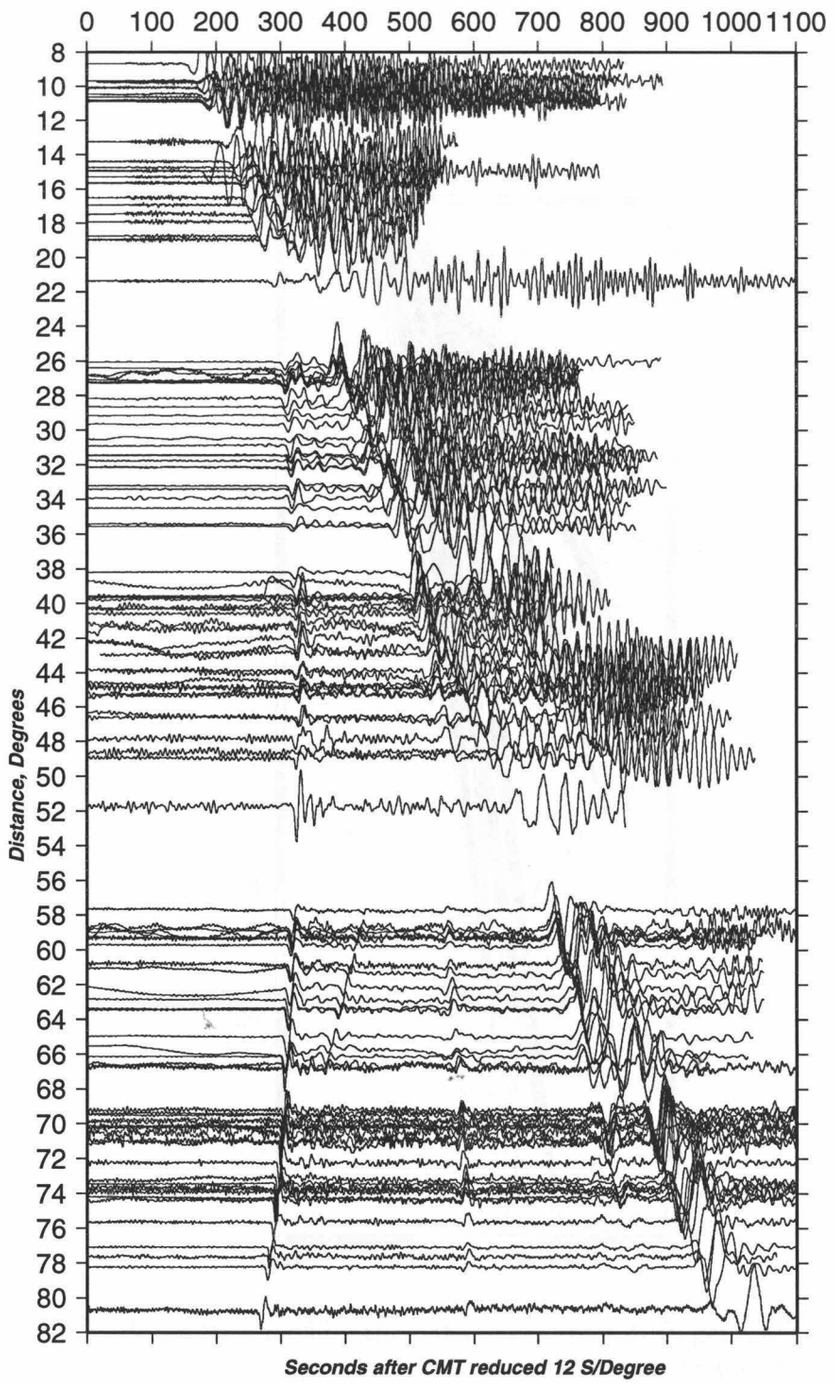

Figure 5.2: Transverse component of the five events whose locations are shown in 5.3 recorded on broadband arrays of the western United States. Clearly shown is S , SS , SSS , and $SSSS$ emerging near 80° distance. Each trace is normalized to the maximum amplitude of the particular trace in the window shown.

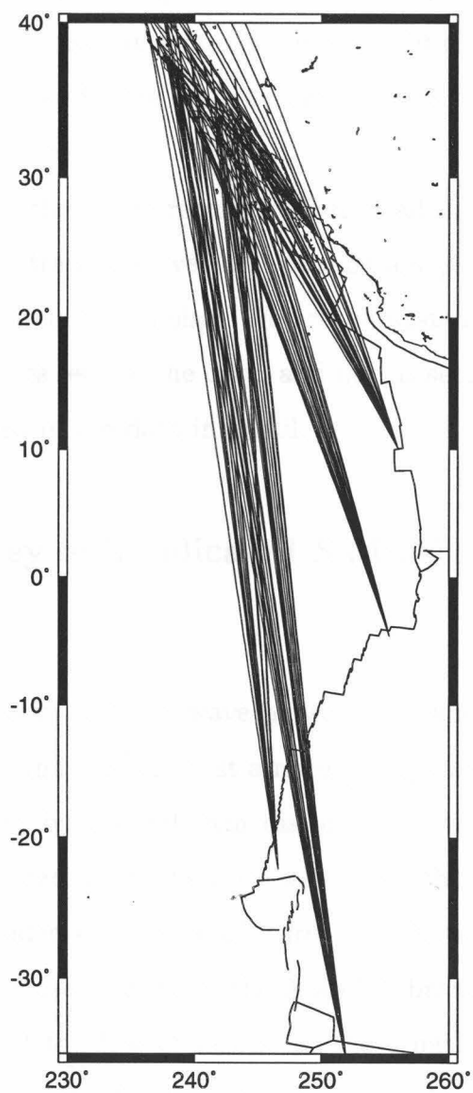

Figure 5.3: Paths traversed by the data of Figure 5.2. In general the energy stays near the East Pacific Rise ridge crest, and where they do deviate the paths still remain under relatively young oceanic crust.

the way along their paths before propagating out under the open oceans. The closest event, located in the Gulf of California, travels under the Baja California Peninsula as well as under the Gulf of California. The event located along the Cocos-Pacific spreading center (corresponding to the data ranging from 25° through 36°) travels very close to the ridge axis, in fact, the raypaths fanning out from this event to the Calfornia networks straddle the ridge axis and it is in these records where we see the strongest lateral variation.

Figure 5.2 shows the entire record section of all data used in the present study. The data shown are transverse velocity records low-pass filtered below five seconds to remove the high frequency noise. We are interested in the triplicated arrivals of the various S multiples seen in the data, and in this section we therefore describe the triplications observed in the data in detail.

5.3.1 A Survey of Triplicated S Multiples

Direct S

Figure 5.4 is a blow-up of the S wave between 12° and 22°. Unlike triplications in direct P which are found near the first arriving energy on seismograms, the transverse S triplication caused by the 410 Km discontinuity is hard to identify due to the fact that S only emerges from the Love wave near the crossover of S and S_{410} near 17°; in fact, the sudden emergence of S from the Love wave near 16° is due to the rapid amplitude increase of S when the A and C branches cross and constructively interfere. Because of the low Q values for these paths throughout the uppermost mantle under the East Pacific Rise, the phase, which at this point is composed of a superposition of energy turning near 300 Km depth with a topside reflection off the 410 Km discontinuity, has little high frequency energy and is therefore not separable into its distinct sub-phases. The S phase is first observable emerging from the Love wave on station CMB (14.75°) but are not fully separated until 16.5° (ORV). Station MIN S is clearly out front and shows a shoulder, but by and large the individual triplicated branch resolution here is not that good.

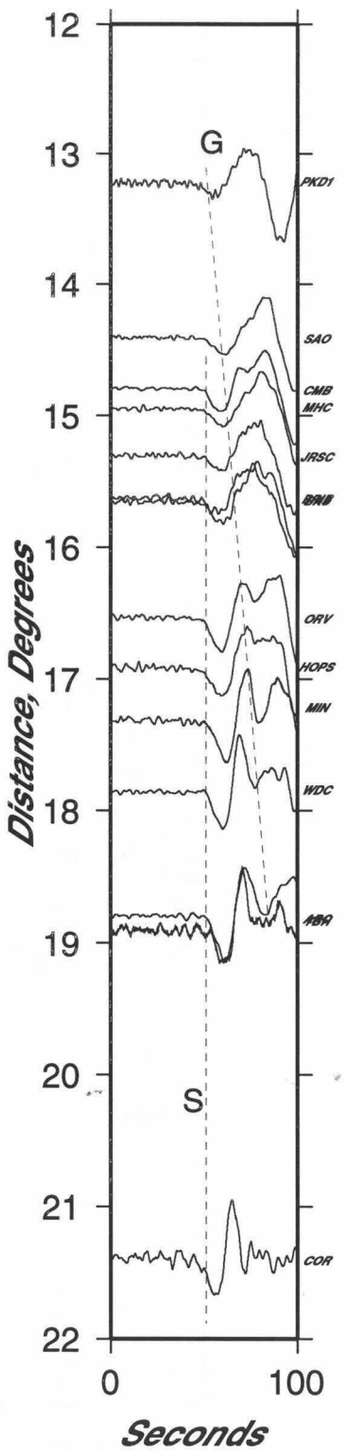

Figure 5.4: Emergence of S from the Oceanic path Love (G) wave. The rapid emergence of S is due to the crossing of the A and C branches of the 410 Km discontinuity triplication. Note the higher frequency energy in the first downswing of stations ORV and CMB relative to the surrounding stations SAO, MHC and JRSC. Both ORV and CMB lie along the Eastern edge of the BDSN, suggesting lateral variation in the uppermost mantle between paths arriving at either side of California.

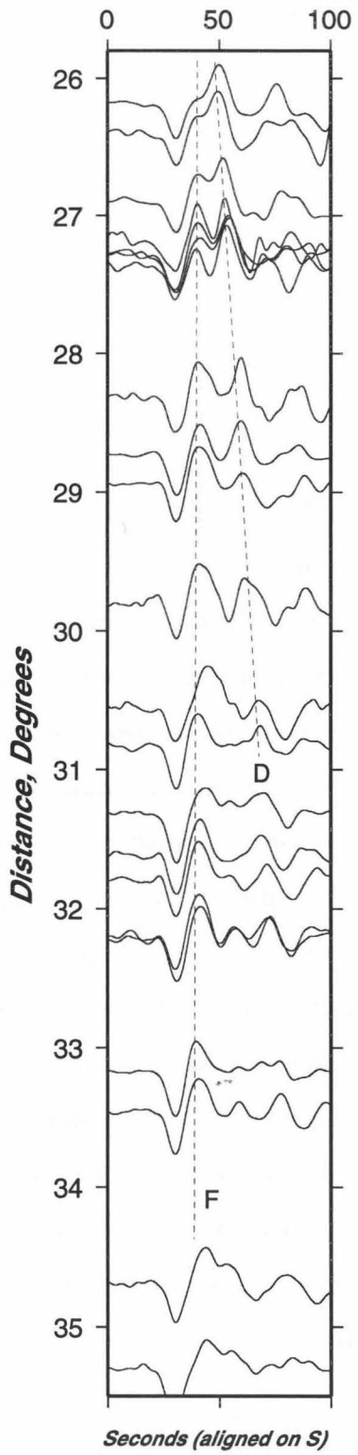

Figure 5.5: Moveout of the D and F branches of S . At these ranges the first arriving energy bottoms below the 670 Km discontinuity so that the D branch, which turns near the 670 arrives after the F branch. Although the data do not extend in sufficiently far to observe the crossing, by extraplolating the identifiable phases at these ranges indicates that the two branches cross near 22°.

Further out in the record section (Figure 5.5) the D (670 turning energy) and F (sub-670 turning rays) branches and moveout between them is readily visible. Branch D is observed near 29° roughly 25 seconds behind the first arriving F branch, which bottoms below the 670. The D phase is dying out and becomes difficult to identify with certainty beyond 31°. In the range between 26° and 31°, it is easily observed how the D branch lags in time and contains decreasing energy relative to the first arriving F branch.

SS

In contrast to the *S* triplication, both the forward and back branches of *SS* triplications from the 410 and 670 discontinuities are observed. Due to the symmetry described above, the individual branches of the triplicated arrival have twice the time separation for *SS* as for *S* , and three times for *SSS* . Besides identifying the actual branches and their moveout within the *SS* phase, a telltale feature of these triplications is how the amplitude of *SS* increases or decreases with range due to the interference of crossing branches. When assessing *SS* amplitudes, it is useful to compare the amplitude to that of *S* , which is bottoming well below the depths at which interference with upper mantle discontinuities occurs and therefore is stable and only slowly changing. As can be seen from Figures 5.6 and 5.7, in which the seismograms are plotted with the maximum amplitude in the window shown normalized to .5 inches, the relative amplitude of *SS* to *S* at 36° through 38° is large due to the crossing of the AB and CD branches. From 39° through 42° the amplitude of *SS* decreases as the two branches move apart, and then rather than decaying further with range, beyond 42° the amplitude rises slightly at 44° as the CD and EF branches cross. Beyond 45° the amplitude then drops off again quickly as these two phases move apart.

Figure 5.6 shows the onset of *SS* where the data first allow its identification away from the Love wave. As based on the 1-D model TNA (derived for EPR events recorded in western North America (Grand and Helmberger (1984)), *SS* at this point (26°) consists of energy which turned within the upper 300 Km. The C branch in

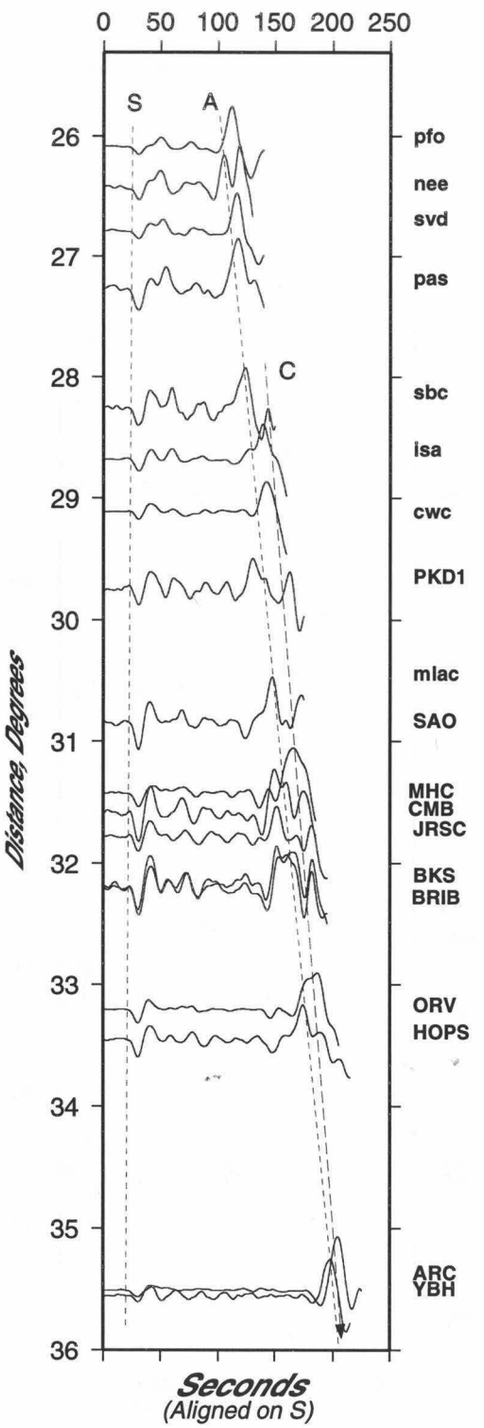

Figure 5.6: Moveout of A and C branches of *SS* . The stability of *SS* is poor, but indicates systematic lateral variation in the uppermost mantle. Stations with early arriving A branch, such as pfo, svd, isa, mlac, and CMB, all lie inland and have propagation paths which come north along paths closer to the East Pacific Rise. Those stations in which A arrives later, such as rpv, SNC, sbc, SAO, MHC, BKS and BRIB, all lie near or along the coast. Particularly striking is the relative misfit between MHC and CMB, which lie at essentially the same latitude but clearly show a major shift in the first arriving *SS* energy.

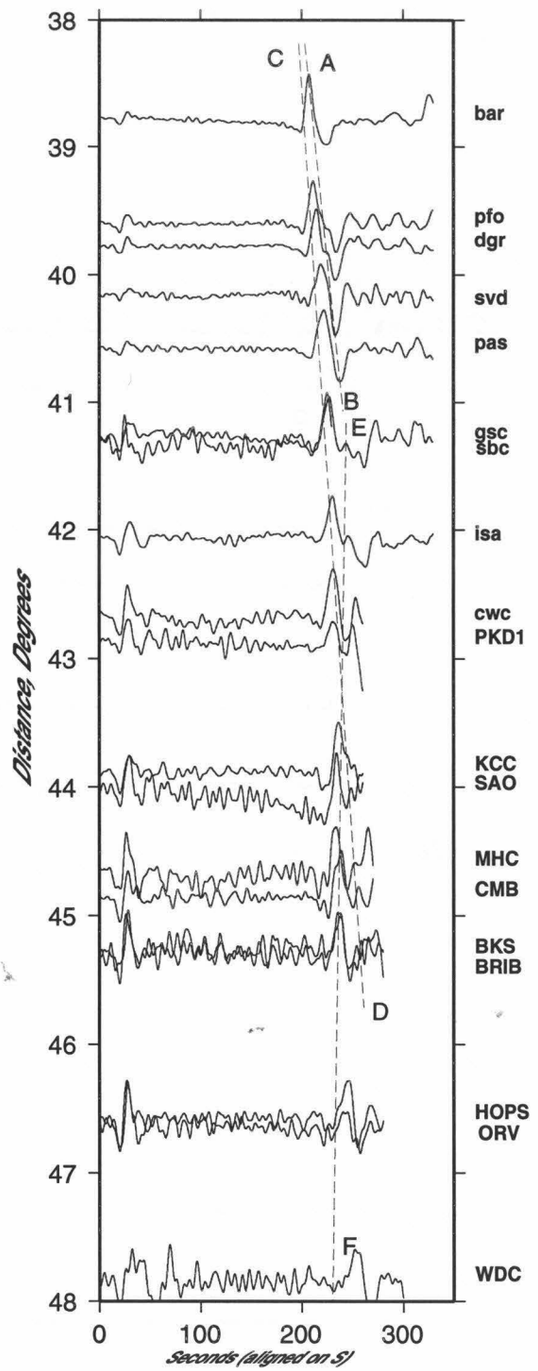

Figure 5.7: Moveout of A and C branches of *SS* . *SS* is large at 36° through 43° due to the crossing of the LID and 410 branches, which constructively interfere in this range. The 410 and 670 branches cross near 44°.

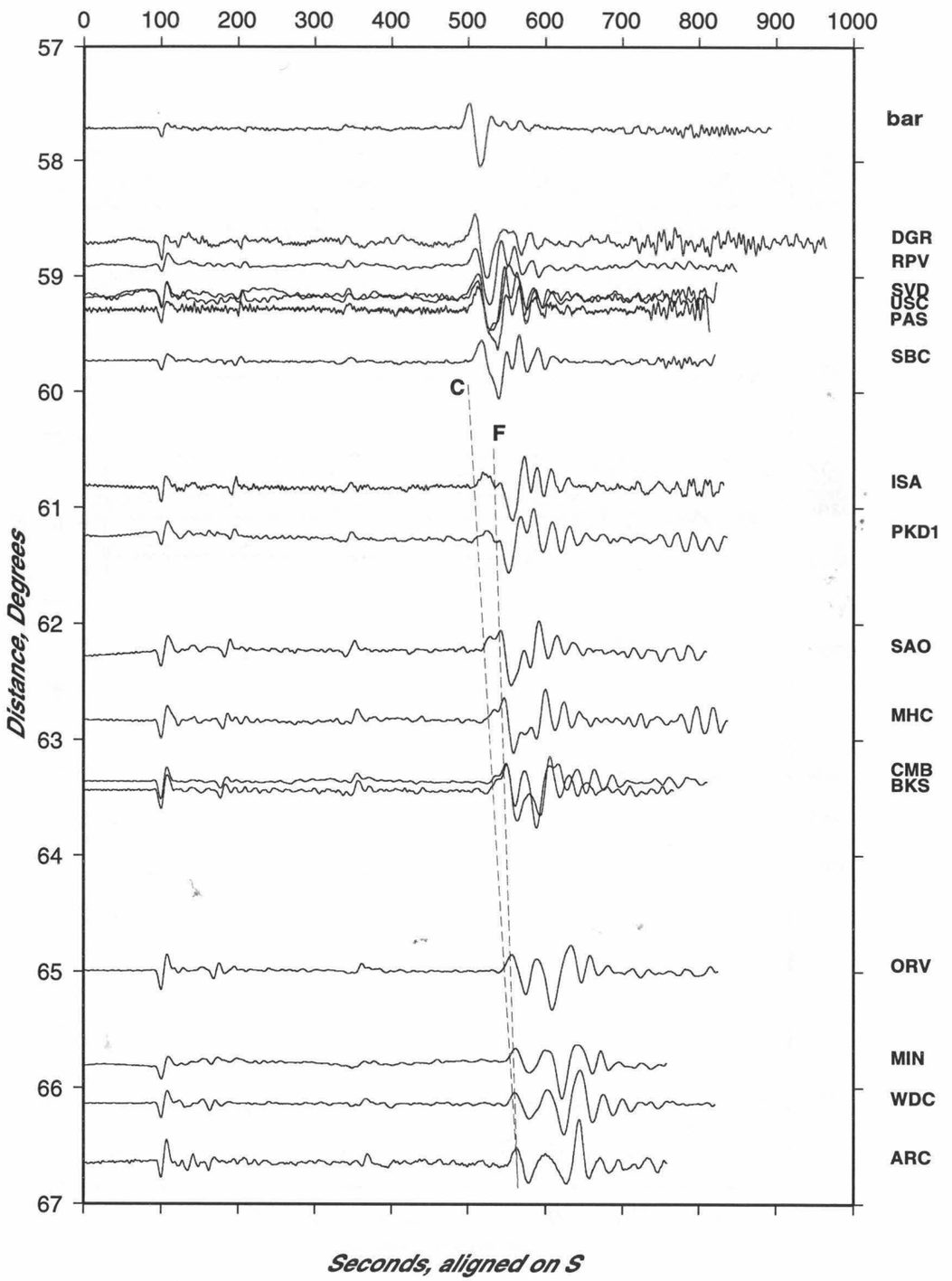

Figure 5.8: C and F branches of *SSS* cross near 54° and are fully separated from the G phase by 57°.

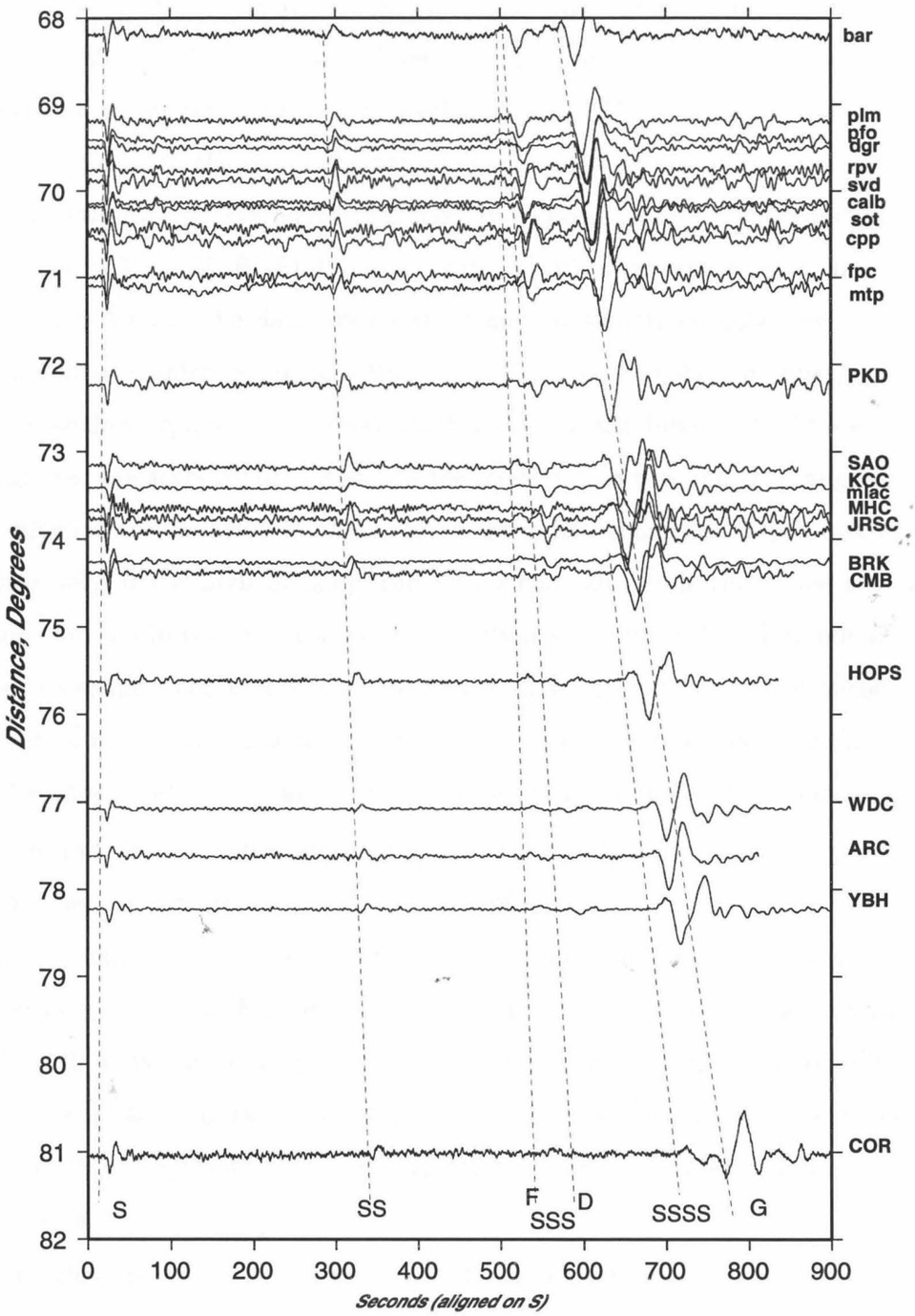

Figure 5.9: Moveout of F and D branches of *SSS* . The very low background noise of the BDSN array allows discerning the 670 triplicated phase out to 82°. *SSSS* is observed emerging from the oceanic G phase at the last trace at 81°.

theory should not begin to develop until 28°, and this is borne out by the data. There is a fairly high frequency pulse seen on station SBC (28.2°) following roughly 25 s behind the obvious A-branch arrival here, and on ISA (28.6°) a well developed shoulder is evident on the relatively late *SS* packet. Station SAO also shows a developed pulse and beyond 31.5° the phase has become sufficiently strong to rival the A branch. By 32° the two pulses have merged sufficiently to produce a broad, double peaked pulse (MHC, CMB, BRIB, BKS). By 35.5° (ARC,YBH), where the A and C branches cross, the pulses seen in the data are coherent and constructively interfere to produce an *SS* amplitude which far exceeds that of *S* . Because the coherent superposition of the two branches produces an arrival which often has the largest amplitude on the seismograms, the stability of this amplitude relative to *S* through this range can be used to infer lateral variation in the upper mantle discontinuities' depth or composition. Conversely, if the high *SS* amplitude stays constant while the whole arrival packet moves around in time from where the synthetics predict it, but does not significantly alter its shape, then this is most likely indicative of lateral variation through regions traversed in similar amounts by both branches of the triplication. For *SS* , this region is the uppermost mantle and lithosphere beneath the midpoint bounce (Figure 5.1).

Overall, there is substantial complexity to the waveforms in this region, but where resolvable the perturbations take the form of instability in the A branch arrival rather than the entire triplicated ensemble, and in particular the 410 energy (C branch) appears quite stable (Figure 5.6, 28°-35°). As is discussed later, the variability in the A branch arrival is entirely a function of the raypaths, with more westerly raypaths consistently arriving faster than those to the east, and so most of the *SS* complexity here is easily explained by lateral variation in the uppermost mantle near the Baja Peninsula.

Further out in distance (Figure 5.7), the forward branch (B) of the 410 triplication is visible as a shoulder decaying on the right side of the *SS* phase between 39° and 41°. This shoulder is particularly evident on stations PFO and DGR. The amplitude of *SS* also drops off accordingly, as seen relative to *S* . Near 41° it is difficult to distinguish between the dying B branch of the 410 and the growing E branch of the

670, as their expected arrival times are simultaneous. In the range between 41° and 43° the back branch of the 670 (E) is growing in amplitude and moving forward to cross the CD branch near 44°. ISA (42°) shows a well developed E branch which is not apparent on PKD1 or CWC, but near 44° KCC has a much larger *SS* amplitude and SAO also. The TNA-predicted crossing distance at 44° of the CD and EF branches is borne out by the data; the sustained strong amplitudes of *SS* relative to *S* in stations KCC (43.9°) and SAO (44.0°) certainly suggest as much, whereas the group of stations near 45° the *SS* amplitude is much less. Very rapidly, as these branches move apart, the amplitude of *SS* drops off as the interference of the branches loses its coherence. By 48° *SS* is composed primarily of energy turning below the 670 and therefore has an amplitude no larger than *S* .

SSS

Because of the $\pi/2$ phase shifts of the multiple S waveforms which occur with each surface bounce (Choy and Richards (1975)), the *SSS* waveform has negative polarity of the *S* and therefore the first swing is up in Figure 5.9. *SSS* pulls away from the Love wave near 63° but is not fully separated until beyond 66°. Figure 5.8 shows this process in detail; inwards of 60° *SSS* has not yet pulled away from the G phase and there is little change in the surface waveform shape between 57° (BAR, DGR, etc.) and 59.7°(SBC). Beyond 60° the first arriving branch of the triplicated *SSS* , C, emerges as evidenced by the altered and double pulse shape of the positive first swing of ISA (60.8°) consisting of the C branch followed by the growing E (670 reflection) branch. The E branch steadily grows and moves forward to merge with the C branch by 65° (ORV). At this point *SSS* is entirely separated from the oceanic G phase, and in the range of 65.3° through 67° the triplicated *SSS* is entirely contained in the first pulse of what appears to be the surface wave train. The oceanic G phase itself through this range undergoes a dramatic degeneration as the wave becomes dispersed by the continental crust.

A gap in the record section exists between 66° and 68°, but by 68° the F and D branches of the triplicated *SSS* have pulled apart. Due to the low noise of the seis-

mograms beyond 70° the phases are readily visible out to 81°, and the first arriving F branch and second D branch are clearly visible. Unlike the usually studied teleseismic phases arriving out at 70° or so, these phases have spent all of their propagation path within the upper mantle and are therefore very diagnostic of the average velocity structure within this region. Furthermore, as seen in Figure 5.3, these phases have also traversed paths which stay close to the East Pacific Rise and therefore should reflect an average ridge crest velocity structure. By examining events whose propagation paths stray widely from the ridge crest, it should be possible to constrain systematic variations in the velocity structure associated with the ridge crest.

To summarize the observations above, in S we identify the triplication due to the 670 km discontinuity and find that the arrival times and amplitudes of both the D and F branches appear to be stable. For SS , we can identify both the forward and back branches of both the 410 and 670 Km discontinuities, but find that the SS triplication is very unstable. As the modeling will show, we ascribe this to strong lateral variation in the uppermost mantle near the Baja California Peninsula. In SSS we identify the D and F branches of the 670 Km discontinuity and can identify the individual branches long after they move apart.

5.4 Modeling

5.4.1 F-K Synthetics

Due to the precedent set by the study of East Pacific Rise events recorded in North America conducted by Grand and Helmberger (1984), it is appropriate to first model the various triplication features with TNA to assess overall timing and phase arrival. We then modify TNA to achieve a better fit to the data at all ranges. Because at teleseismic distances the first arriving S bottoms deep in the lower mantle, the upper mantle model TNA is overlaid on PREM-like (Dziewonski and Anderson (1981)) velocity structure below 400 Km depth. The model is shown in Figure 5.10. We calculate frequency-wavenumber (FK) Green's functions which we use to generate

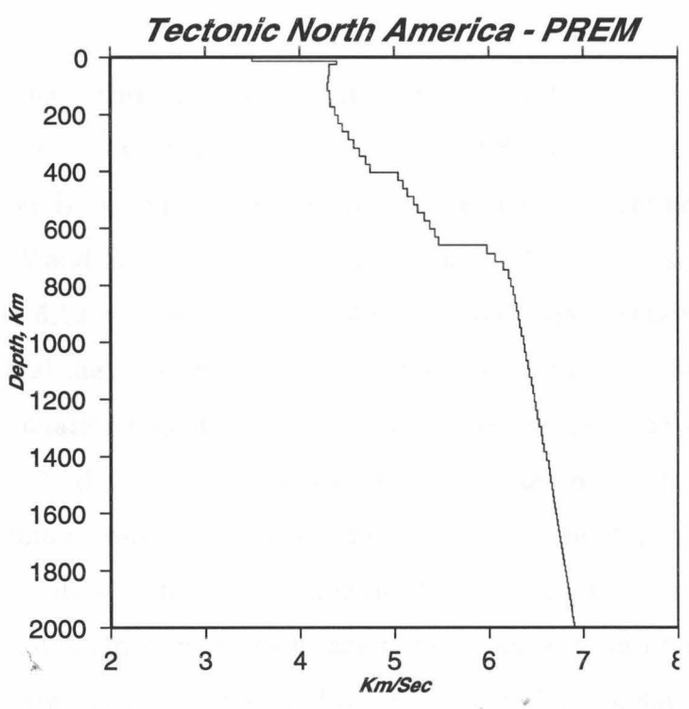

Figure 5.10: The shear wave model used in the F-K synthetics. This model consists of the upper mantle model Tectonic North America with a 10 Km thick crust, which was derived from East Pacific Rise events recorded in Western North America (Grand and Helmberger (1984)), overlain on a PREM-like model modified to keep velocity continuity with depth (Dziewonski and Anderson (1981)).

synthetics. In all computed seismograms shown, the source is placed at 10 Km depth and the velocity records are convolved with a 1,1,1 s trapezoid, which provides a reasonable simulation of upper mantle attenuation.

Because the hardest data to fit with the 1D synthetics are the *SS* triplications, we save those for last after discussing the *SSS* and *S* fits, as the misfit of *SS* will lead naturally into the subsequent discussion.

SSS

Teleseismic locations of these EPR events are not sufficiently reliable to justify using absolute travel times, so we use the differential *S* - *SSS* time to plot the data and synthetics, which ends up constraining the relative velocity changes between the bottoming depths of *S* and *SSS* . Figure 5.11 shows the TNA synthetics overlaid on the data, while Figure 5.12 is an enlargement of the clustered data between 69°-71° and 73°-74.5°. In general the fit is quite good, with the most notable misfit caused by the upper mantle attenuation higher in the synthetics than the data. *SS* is slightly early over ranges from 69° through 72°, whereas there is almost no misfit beyond 74° in terms of the maximum amplitude arrival time. *SSS* maximum amplitude throughout the range is slightly delayed from the synthetics by about 2 s on average throughout the entire range, although some stations are notably worse than others. KCC, gsc, HOPS, and YBH are the most extreme (Figure 5.13), with the delay closer to 5 seconds. Stations PKD1 and MWC are closer to 2 s delay, which is near our ability to pick the arrival times.

The greatest misfit involves the small precursor to the *SSS* pulse seen from 69° through 71°. The synthetics do not show this phase until the range exceeds 73°, but in the data it is clearly developed by 69°. At these ranges the first arriving energy bottoms in the lower mantle (branch F), with the secondary arrival caused by the 670 Km discontinuity. Though not perfect, in general the *SSS* fit with standard TNA is quite good and the small regions of E-F branch misfit can be caused by average velocity variations which are less than 1% deviation from TNA. For example, for the station with the greatest misfit in *SSS* arrival timing, KCC, the roughly 10

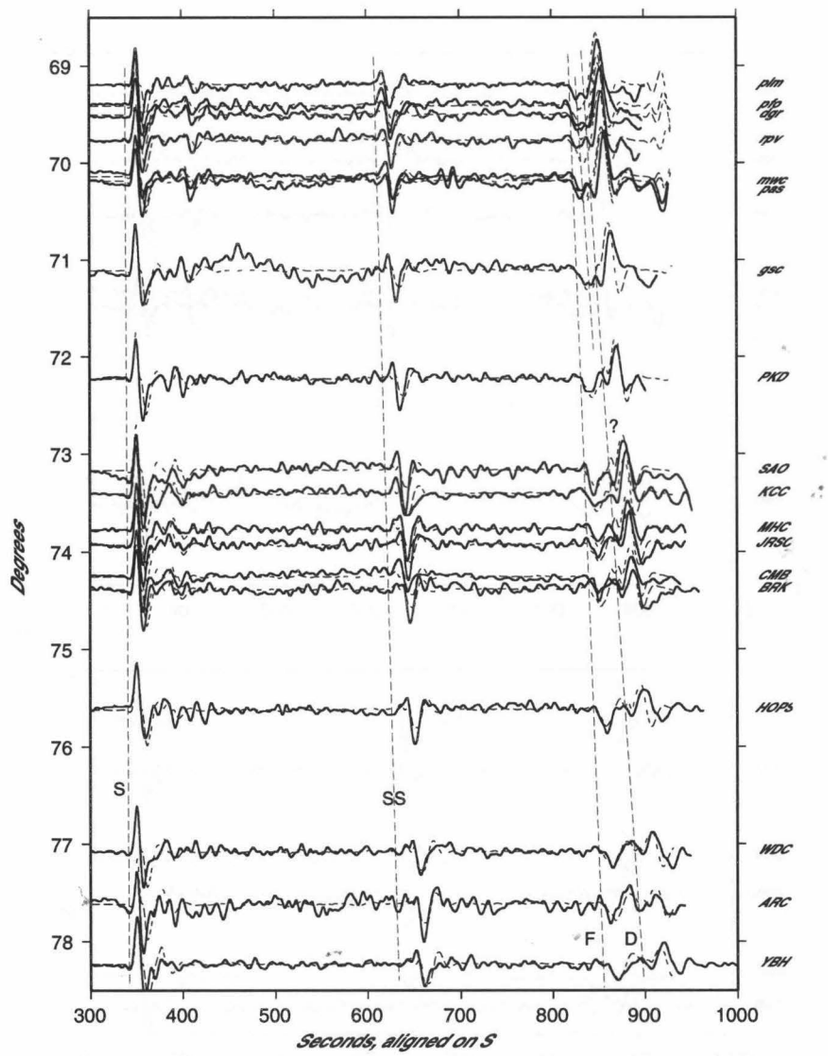

Figure 5.11: The D and F branches of *SSS* (Solid Black line) compared with FK synthetics based on Tectonic North America. All traces are normalized to the maximum amplitude shown in the window and aligned on the *S* arrival time. Generally the fit is good, particularly the *S* - *SS* differential time. The *SSS* arrivals are systematically behind the synthetics by several seconds, but this is over a differential travel time of 500+ seconds and therefore represents an average velocity anomaly of well under 1% from the average predicted by TNA. Blow-ups of ranges 69°-71° and 73°-74.5° are shown in Figure 5.12.

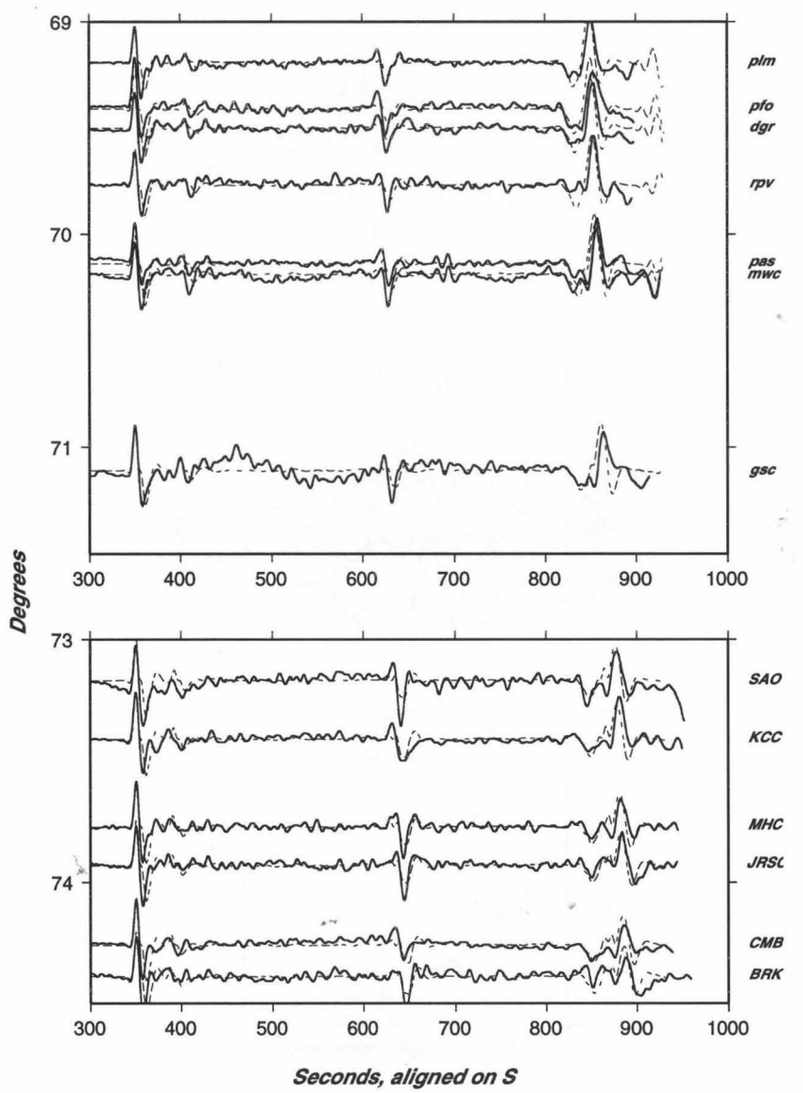

Figure 5.12: Enlargement of Figure 5.11. The D and F branches of *SSS* (solid black line) compared with FK synthetics based on Tectonic North America. All traces are normalized to the maximum amplitude shown in the window and aligned on the *S* arrival time. The systematic lateness of the largest *SSS* pulse represents a small deviation from TNA in terms of the diferential travel time.

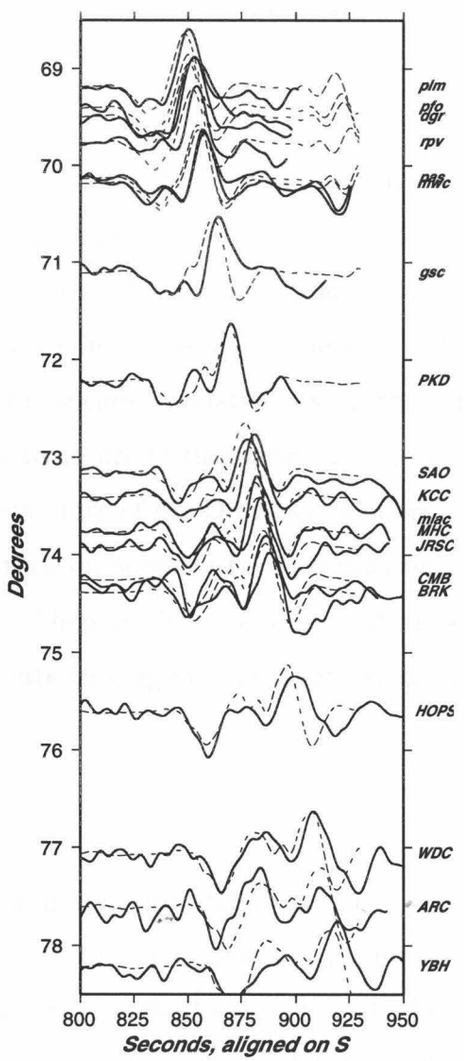

Figure 5.13: Blowup of *SSS* data and synthetics shown in Figure 5.11. The *SSS* arrivals are systematically behind the synthetics by roughly 2 seconds, but the scatter in this lateness varies from none (stations PKD) to 5-6 seconds (KCC, gsc, SAO). This timing misfit is over a differential travel time of 500+ seconds and therefore represents an average velocity anomaly of well under 1% from the average predicted by TNA.

second delay occurs over a 550 second differential travel time, so the average velocity variation from the model is in fact low. However, as subsequent discussion will show, we can largely account for this arrival with the addition of a Lid and more realistic attenuation structure of the paths through the EPR.

S

We are constrained to only model the forward branch of the 670 Km discontinuity triplication because at distances closer than 26° the Love wave overwhelms the triplicated body waves. The data for the F-D branches of the 670 triplication with synthetics overlaid are shown in Figure 5.14. Beyond 27° the timing and relative amplitudes of the F and D branches fit relatively well; the scatter between waveforms is most likely due to local structure in that there are no obvious trends in the misfit through the data. The decay rate of the D branch is appropriate in that it over- and underestimates the amplitude on adjacent traces, indicating that in an average sense the decay is well modeled. The data is more heavily attenuated than the synthetics, but the overall fit is adequate to suggest over these raypaths as well the East Pacific Rise is TNA-like.

SS

Triplicated *SS* is by far the most complicated and least easily modeled phase of the waves discussed here. Specifically, the phase traversing the uppermost mantle, the AB branch, is severely scattered, while the back branch of the 410 and both branches of the 670 triplication are reasonably well modeled. At further ranges the CD-EF crossover of the 670 is well modeled in terms of timing and amplitudes, but the *SS* packet appears quite variable at closer distances of 25°-36°. As discussed in Figure 5.6, the *SS* packet of 410-triplicated branches moves around extensively relative to the synthetics. This is the by far the largest misfit in the data set. Closer inspection, however, reveals that this uppermost mantle traversing phase appears on some traces to arrive extremely early, in some cases by as much as 15-20 seconds (rpv, sncc, sbc, PKD1, SAO, MHC, JRSC, BRIB, BKS, and HOPS) while on the rest (pfo, nee, svd,

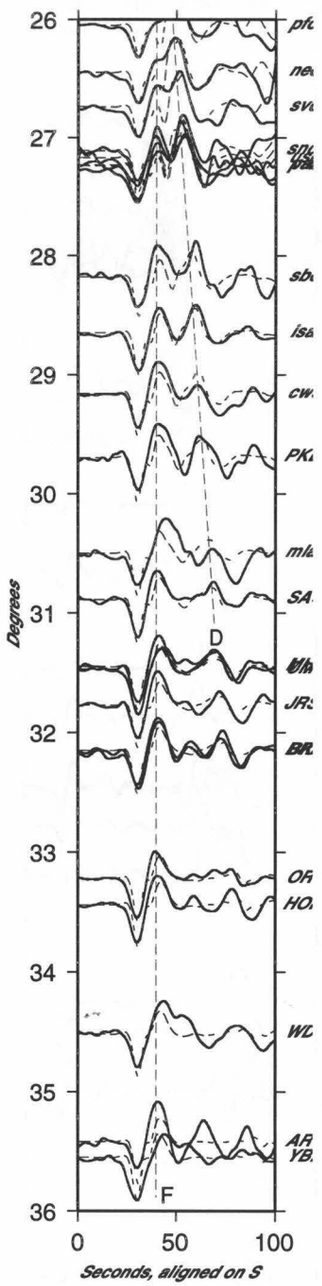

Figure 5.14: in the F-K synthetics. This model consists of the upper mantle model Tectonic North America, which was derived from East Pacific Rise events recorded in Western North America (Grand and Helmberger (1984)), overlain on a PREM-like model modified to keep continuity and travel time (Dziewonski and Anderson (1981)).

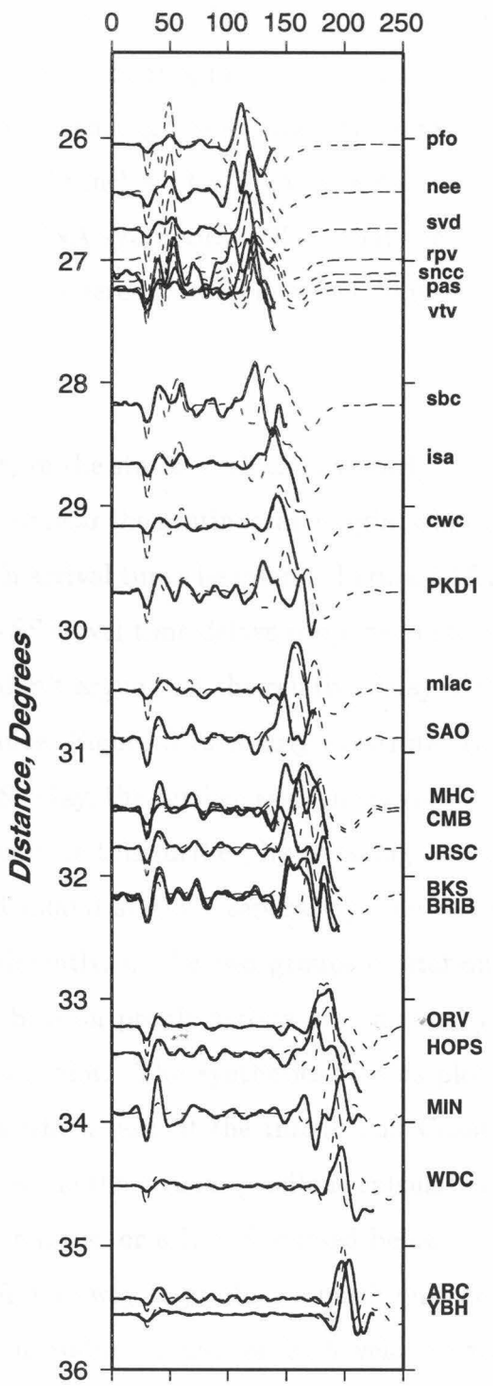

Figure 5.15: Data and Synthetics of *SS* 410 triplication, back branch. In general the fit is poor, both in timing and amplitude of the *SS* ensemble. The D and F branches of the *S* triplication are well modelled, suggesting strong variation in the upper mantle where *SS* travels. The sites which fit the worst lie along the coast and consistently have the fastest arriving energy.

isa, cwc, CMB, and ORV) the fit is good. Furthermore, on all of the traces the 410 arrival (C) is stable across the traces whose A branch is variable. This is a telltale signature of lateral variation occurring in the uppermost mantle at depths sampled by the A branch, but not extending deeper into the mantle. By 36° (stations YBH, ARC), where the A and C branches of a TNA-type 410 triplication are expected to cross, the data match the TNA synthetics well, in that the *SS* pulse is very large and simple in shape, indicating coherency and constructive interference.

Evidence for a Lid

One obvious commonality of the stations which have early A branch arrivals in Figure 5.15 is that they all lie on or near the continental margin, while all of the stations which have well fitting A branch arrival times lie inland. Figure 5.16 makes this clear; this is the contouring of the *S* -*SS* travel time delays projected onto the midpoint bounce of the raypaths. While we don't argue that the relative delay of the A branch all occurrs at the *SS* midpoint bounce, Figure 5.16 clearly illustrates the east-west geographic dependence of the *S* - *SS* delay, the further west the raypaths traverse, the faster the A branch arrives. To illustrate this further, by breaking out the coastal stations and plotting the coastal and inland stations separately, one can see that the A phases line up nicely, albeit differently, in the two groups of stations. In Figure 5.17, the A branch of the Inland Station profile arrives systematically 10-15 seconds behind that of the coastal station plot. The synthetics in this plot are devived from two different velocity models which best fit the Inland and Coastal stations; the Inland profile is standard TNA while the coastal profile is calculated with the addition of a high velocity uppermost mantle, or a Lid, discussed below.

A very simple and effective way to produce a much quicker first arriving A branch in the triplication is to introduce a Lid, or high velocity zone overlying a deeper low-velocity zone, into the model. The effect is two-fold. First, the high velocity layer serves to speed up the entire model, but preferentially advances the shallowest bottoming energy over deeper rays because the former spends a proportionately larger amount of time in the fast layer. More deeply bottoming energy propagates through

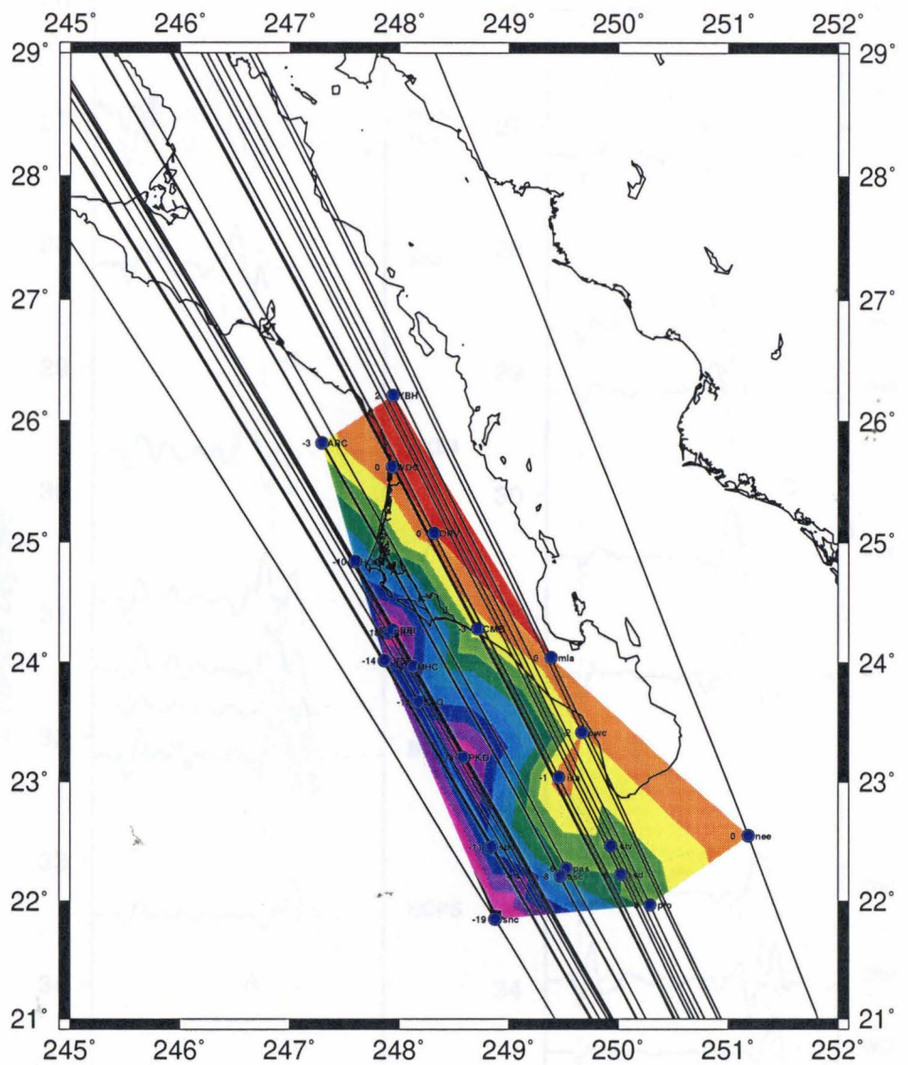

Figure 5.16: *SS* raypaths contoured and delayed, showing azimuthal dependence of the A-B branch travel times. Darkest blue represents -20 Seconds travel time, brightest red indicates +5 seconds traveltime. Dots show the *SS* midpoint bounce. The entire raypaths for this event are shown in Figure 5.18.

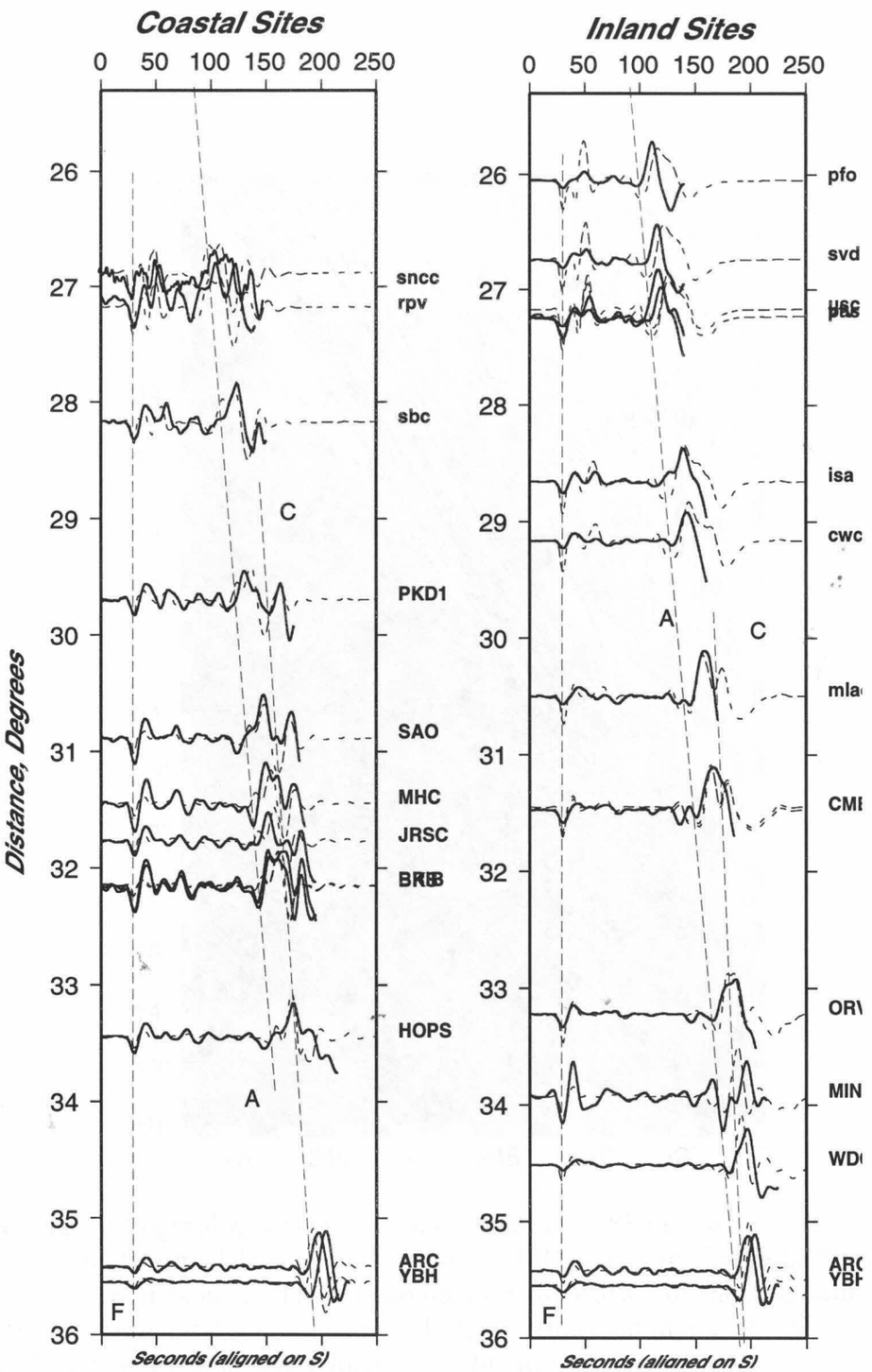

Figure 5.17: Breakout of Figure 5.6 of Coastal and Inland sites. From this plot the early arriving A branch is easily identified and systematically arrives 10-15 seconds before the A branch recorded on inland sites. The two sets of synthetics are derived from different 1D velocity models, shown in Figure 5.20. The A branch of the Coastal arrivals is between 10 to 15 seconds early than for the inland sites.

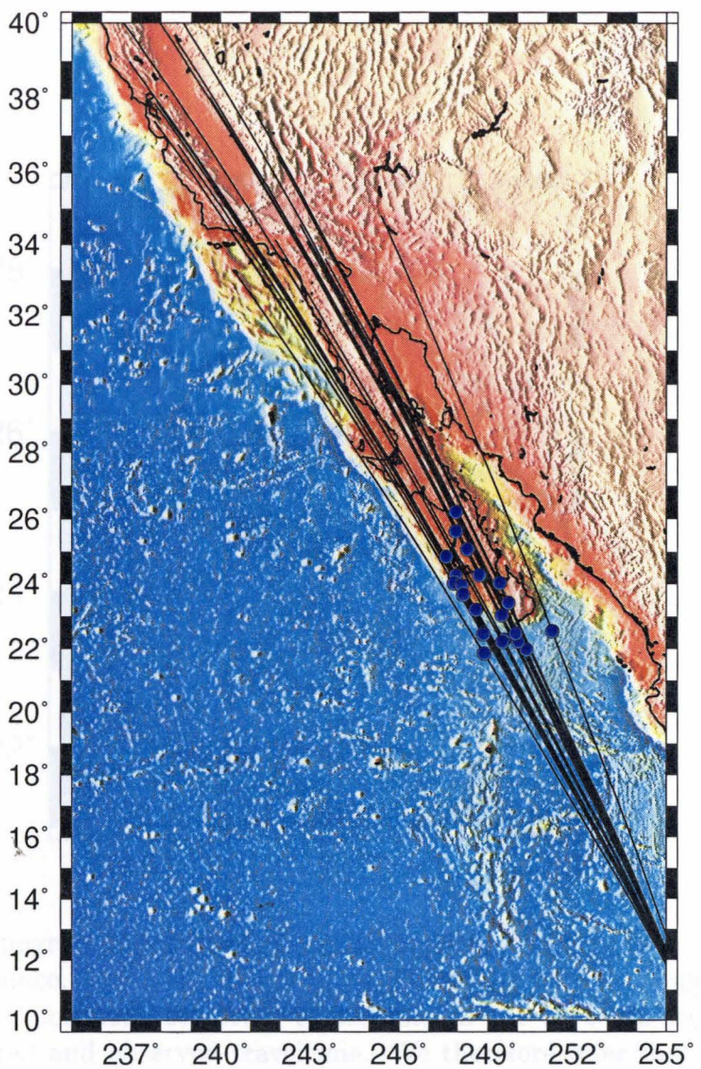

Figure 5.18: Topography, bathymetry and raypaths of *SS* raypaths plotted with synthetics for the two models with and without a LID shown in Figure 5.17. Blue dots show *SS* midpoint bounce. There is no obvious correlation of the A-B branch velocity with the continental margin and the lack of orthogonal raypaths makes discerning where along the raypaths the velocities are highest difficult.

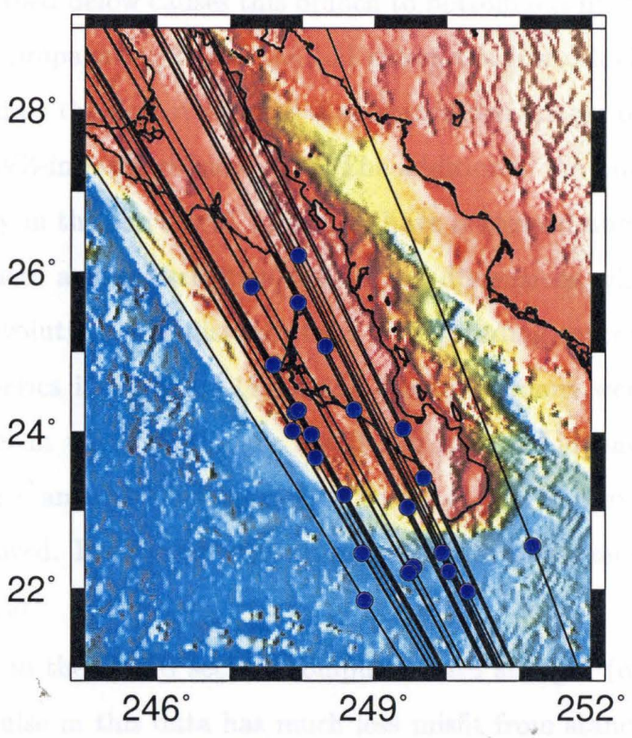

Figure 5.19: Topography, bathymetry and raypaths of *SS* phase here. Blue dots show *SS* midpoint bounce. The local bouncepoints cannot contribute enough of a delay for any reasonable lithospheric structure to account for the up to 20 seconds difference between predicted and observed traveltime. We therefore infer that the uppermost mantle along the entire path is anomalous.

this region at steeper angles and therefore spends less time in the region and the associated delay is less. Secondly, by Snell's Law, the addition of the fast layer causes the first arriving, shallowly bottoming energy to bottom out more shallowly still, increasing ever more the net amount of time spent in the fast layer and compounding the overall phase advance. The effect is extreme; for example, at 15° distance the first arriving A branch bottoms near 300 Km depth without a Lid, whereas the addition of the Lid described below causes this branch to bottom out in the vicinity of 100 Km depth. Energy propagating below the Lid enters the low velocity zone, is deflected downwards, and by the time it surfaces it appears much further out in distance, at the far end of the LVZ-induced shadow zone. The addition of the Lid therefore constrains all of the energy in the arriving A branch to have bottomed above the bottom of the Lid, and produces a fairly sensitive test of Lid dimensions which we use below to constrain Lid evolution with distance from the spreading center. Through trial and error the synthetics in Figure 5.17 for the coastal stations were generated using a TNA-like model in which the upper 35-70 Km form a Lid having a velocity 3.5% faster than the standard TNA model. The fit of the A branch for these sites is markedly improved. It remains to see if raypaths traversing more westerly azimuths also require a Lid.

Further out in the record section computed with straight (on-Lid) TNA (Figure 5.21), the *SS* pulse in this data has much less misfit from standard TNA synthetics than at closer ranges. The largest deviations are concerned with the relative amplitudes of *SS* versus S, in that the data have a much higher ratio than predicted by straight TNA. Additionally, what appears to be the decaying 410 B branch, arriving after the C branch at ranges 38° through 40° to form a right shoulder on the main *SS* pulse, is not present in the synthetics at all, suggesting a somewhat stronger 410 reflector at this range than that in TNA. Furthermore, the growing 670 reflection, E-F, seen in the data at ranges 41°-44°, has an increasingly large right side shoulder on *SS* , which is not observed in the synthetics at all.

These synthetics indicate that standard TNA is a bit slow, in that most of the obvious triplicated and surface phases arrive earlier in the data than the model predicts.

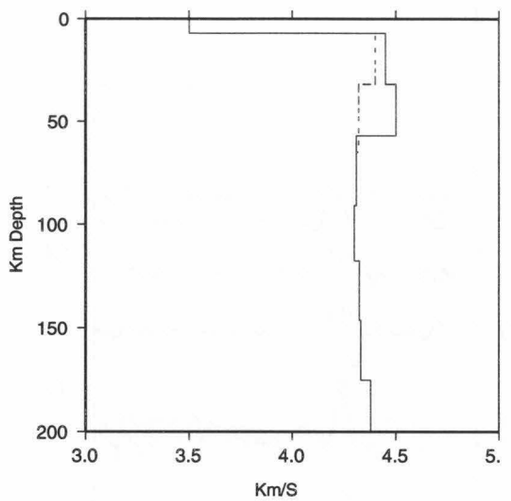

Figure 5.20: Modified TNA (solid) overlain on TNA (dashed) used to explain the coastal early arrivals of the A branch in Figures 5.15 and 5.17.

The strong lateral gradient in uppermost mantle velocity which suggests the need for a Lid in the discussion above is a tip-off that the data at other ranges following more westerly propagation paths through the upper mantle should be compared against synthetics generated with models containing a Lid. Part of the misfit here (41°-44°, Figure 5.21) may come from the fact that the synthetics are calculated from a model which does not have a Lid in it, which the *SS* data at closer ranges suggests ought to be there if Lid the thickness depends systematically on distance perpendicular to the ridge crest axis. The existence of a well established Lid should be observable at these ranges because the structure will produce a substantial shadow zone which will differentially affect the amplitudes of the sub-phases forming the triplications. We therefore calculate synthetics for the more distant ranges which travel further away from the EPR crest for the TNA model modified to contain a Lid to see if in fact such a modification is warranted by data other than for which it was prescribed. In addition, the relative branch amplitudes will depend to some extent on differential attenuation, so at further distances we introduce the upper mantle attenuation structure of Ding and Grand (1993), which was derived for East Pacific Rise events recorded in Western North America.

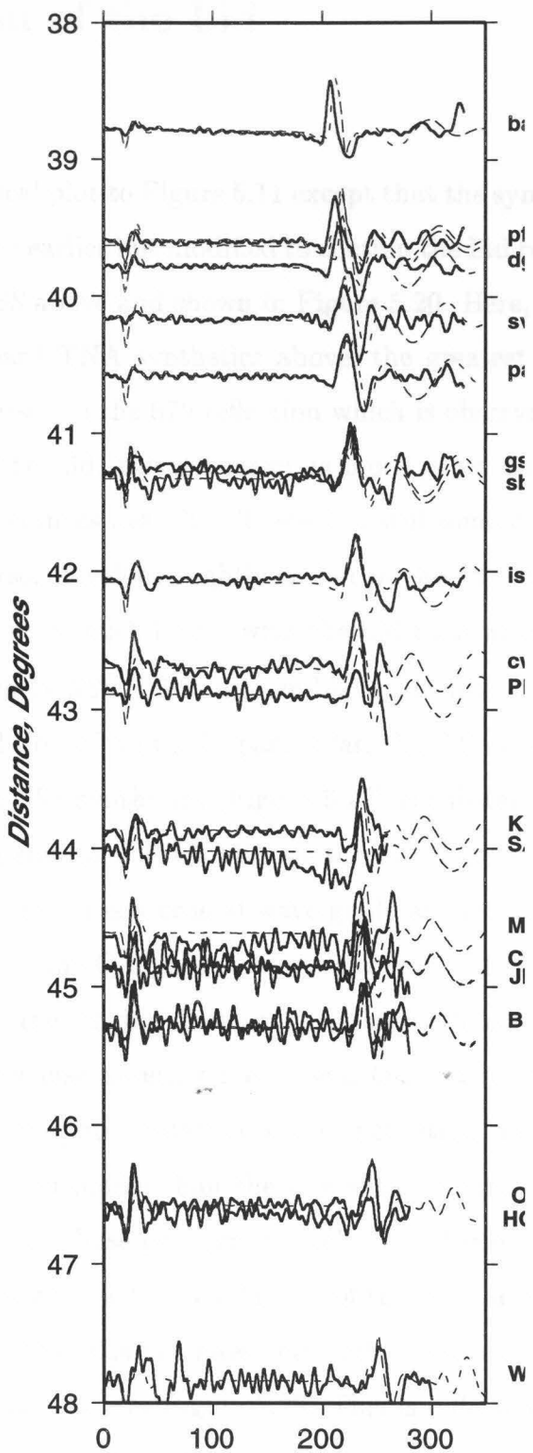

Figure 5.21: Data and Synthetics of *SS* 410 and 670 triplications for the TNA model without a LID. Unlike the *SS* 410 triplication back branch, the overall behavior of the waveforms here are fairly good, with the greatest misfit caused by the relative *S* - *SS* amplitudes. The addition of a LID, however, improves the fit substantially.

5.5 Evolution of the Lid

Triple-S

Figure 5.22 is an identical plot to Figure 5.11 except that the synthetics are calculated for the TNA model used earlier but modified to contain the Lid required by the coastal propagation paths of *SS* above and shown in Figure 5.20. Here, the synthetics fit the data better. In standard TNA synthetics above, the greatest misfit consisted of a lack of the small precursor to the 670 reflection which is observed in the data. In the synthetics employing the Lid, this precursor is much more strongly developed and matches the data to distances near 70°. There is a still some misfit between 70° and 69°, in that the precursor develops slightly earlier in the data than these synthetics, but in general the the fit is much better with the Lid than without it.

At closer ranges, where *SSS* is first discernible from the surface waves, the fit also improves with the addition of a Lid. In particular, the differential time between the G phase and *S* on the *SSS* synthetics (Figure 5.23) is substantially better than the fits derived from using standard TNA without the Lid (Figure 5.24). The ringing at the tail of these seismograms is a crustal wave-guide artifact induced by a high-Q 7 Km thick crust; we leave the Q high in the model because it is specified in Ding and Grand (1993), because the ringing does not interfere with the triplication phases at these distances, and because lowering the crustal Q contributes to a slight velocity shift which would bias the interpretation of the synthetics. The G phase at 57.7° is much later in the non-Lid model than the one with it; this is expected due to its strong influence on the G phase propagation velocity. However, at these ranges the model is still a bit slow, even with the addition of the coastal-*SS* appropriate Lid, as observed from the fact that the G phase and both branches of the 670 triplication arrive slightly, but equally, late in Figure 5.23. This is indicative of a need for a still slightly faster uppermost mantle, rather than velocity perturbations at depth in the vicinity of the discontinuities. This is important to note, because these raypaths lie the furthest from the ridge axis (Figure 5.3) on average over their propagation path to the seismic networks. Based on these records, the Lid model which fits data traveling

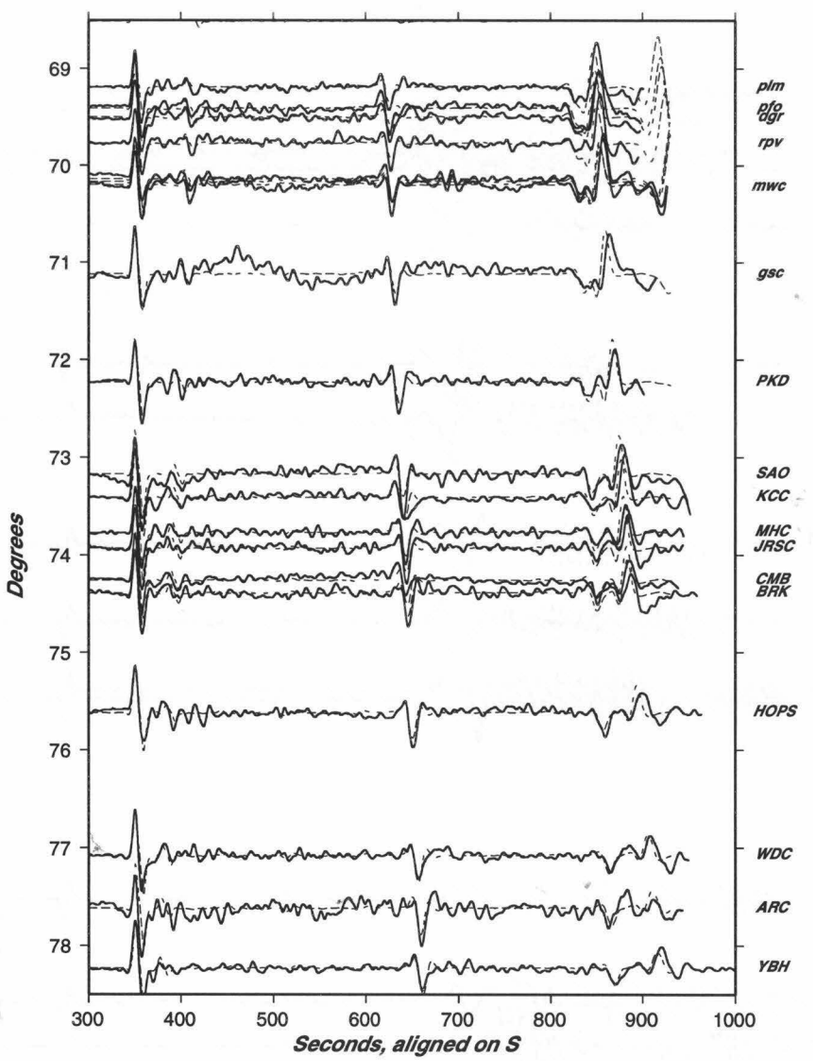

Figure 5.22: The D and F branches of *SSS* (Solid Black line) overlaid by FK synthetics based on Tectonic North America modified to contain a LID, as shown in 5.20. All traces are normalized to the maximum amplitude shown in the window and aligned on the S arrival time. The fit is better here than with Standard TNA. Particularly the small phase developing near 70° is much better.

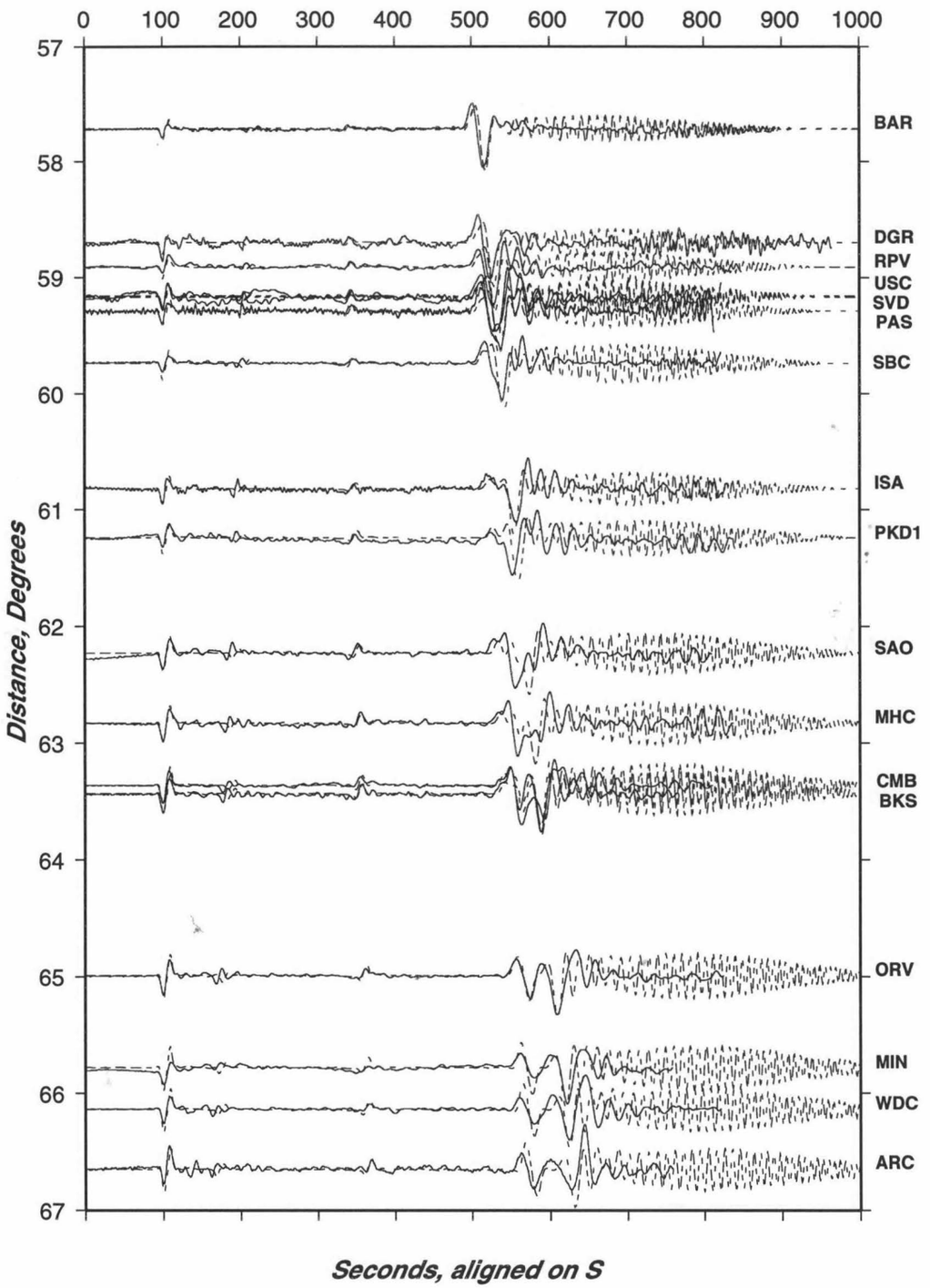

Figure 5.23: *SSS* emerges from the G phase by 60°, where the CD-EF branches are clearly discernible. The synthetics correspond to TNA with the LID derived from the coastal *SS* data at closer ranges. However, the model is still a bit slow, as observed from the G phase and both branchs of the 670 triplication arrive slightly, but equally, late. This is indicative of a need for an slightly faster uppermost mantle, rather than velocity perturbations at depth in the vicinity of the discontinuities.

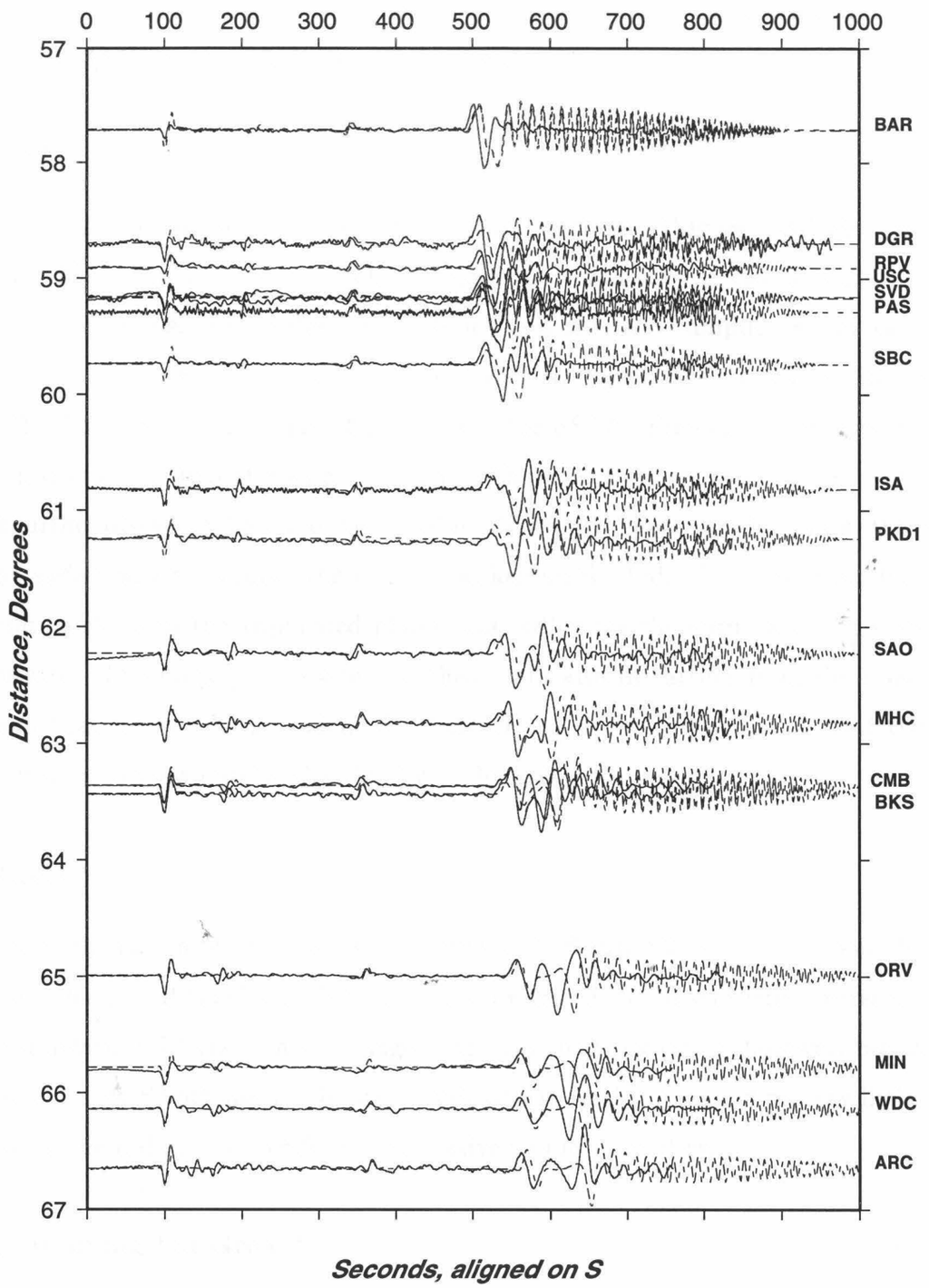

Figure 5.24: Synthetics calculated from standard (no LID) TNA clearly do not fit the data very well in terms of modelling the whole seismogram. The synthetics are clearly late in the triplicated 670 phase as well as the G phase, and a faster uppermost mantle would speed up these arrivals equally without inducing relative shifts.

closer to the axis is insufficiently thick to fit more off-axis data, and would appear to indicate Lid growth with distance from the ridge axis.

Double S

At still closer ranges, the *SS* 670 triplication synthetics (Figure 5.25) also improve with the addition of the Lid. The *SS* ensemble timing at the closest station, BAR (38.7°) is more similar to the data both in terms of relative amplitude and waveform shape than those derived with the standard TNA synthetics (compare with Figure 5.21). Furthermore, throughout the range of the *SS* 670 triplication (through 48°) the fit is demonstrably better with a Lid than without it. However, like the *SSS* synthetics at further distances, here too the model is still slightly slow overall, and like the *SSS* , the easiest way to improve the fit is to thicken up the Lid, which won't produce any relative shifts in the triplicated phases but will move the entire arriving ensemble forward. The propagation paths for these data also lie farther from the ridge axis than that for which the Lid model was derived, indicating here too that the Lid continues to grow outside the vicinity of the axis.

Direct-S

The *S* triplication, shown again with synthetics in Figure 5.26, doesn't help much here. From this plot it is evident that the fit is no worse than the synthetics corresponding to standard TNA through this range. This is actually expected, however, because at these ranges *S* bottoms deeply and travels nearly vertically, spending very little time within the Lid and is therefore not sensitive to Lid properties.

Quantifying Lid Growth

The growth of the Lid with distance from the spreading center is an important constraint on the dynamics of ridge melt and mass transport, and so merits a quantitative estimate of its growth rate with distance from the ridge crest. Through experimentation with different types of LidS in which we vary thickness and velocity as above,

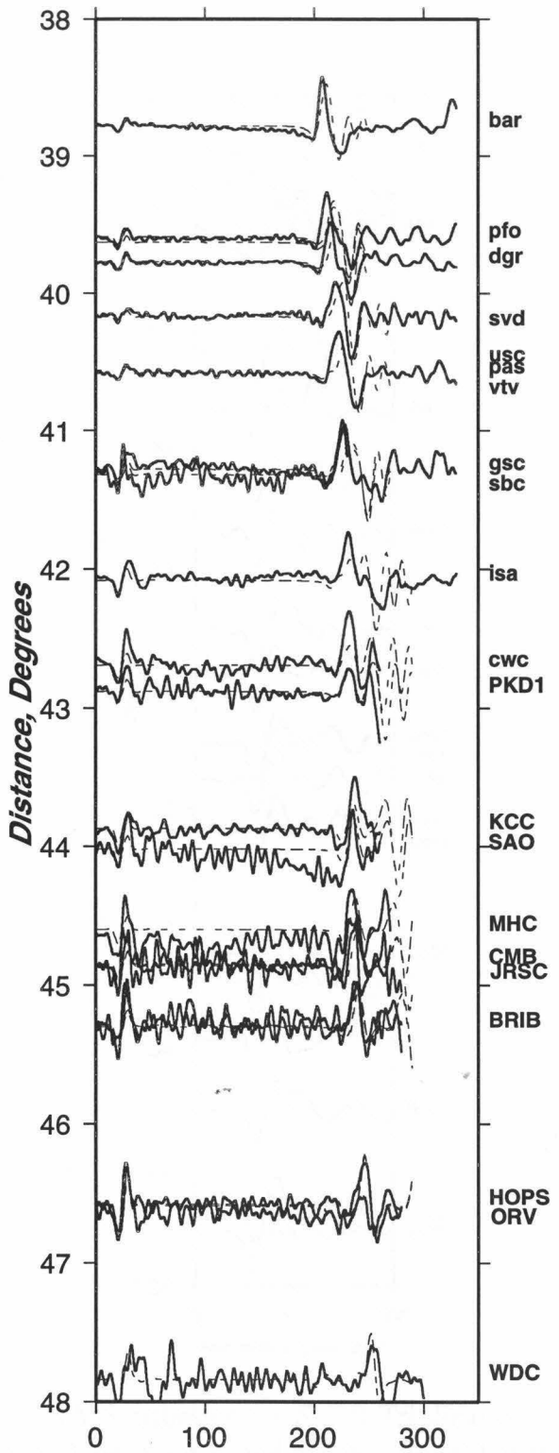

Figure 5.25: Data and Synthetics of *SS* 410 and 670 triplications. Unlike the *SS* 410 triplication back branch, the overall behavior of the waveforms here are fairly good, with the greatest misfit caused by the relative *S* - *SS* amplitudes. These synthetics are generated by TNA modified to contain the LID shown in Figure 5.20. As is the case with the *SSS* triplications, the entire triplicated ensemble is arriving later in the synthetics than in the data, indicating that the model needs to be sped up a bit at the shallowest mantle, i.e., the LID needs to be thicker here.

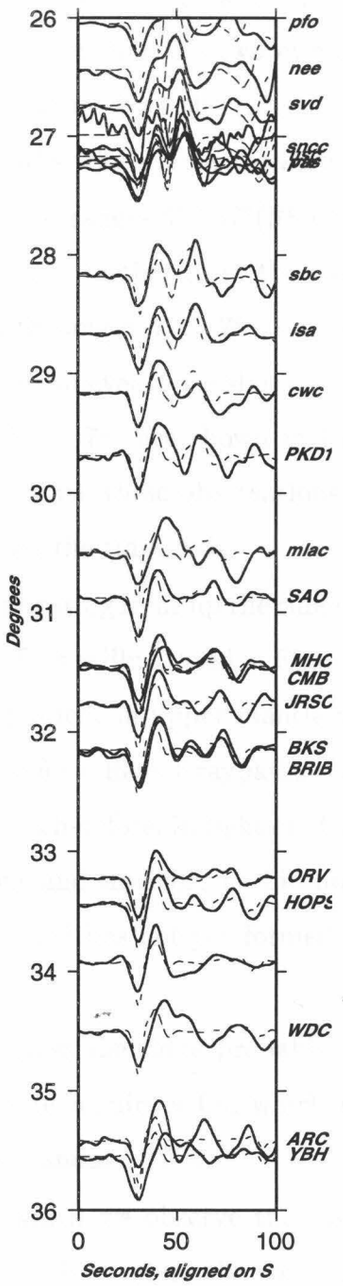

Figure 5.26: Modified TNA Synthetics for S 670 Triplication; D-F branch moveout and FK Synthetics. Since S dose not spend much time within the uppermost mantle, the addition of a LID to these synthetics does not alter them appreciably. Simply put, S is not diagnostic of LID structure.

we can come up with optimum structures to best fit the off-axis data. Two different Lids are required to fit the three different events which show *SSS* and *SS* phases; this is not surprising in light of the fact that the two events requiring the thickest Lid have raypaths which travel well away from the ridge crest while the event requiring a slightly thinner Lid has raypaths which cross the spreading ridge.

The raypaths corresponding to ranges 57°-67°(*SSS*) and 38°-48°(*SS* ; see Figure 5.3 for raypaths) travel on average farther from the ridge crest axis than the data from the most distant event with ranges 68° - 78°, whose paths actually cross under the EPR. The synthetics for the two events are shown in Figures 5.29 and 5.28, while the synthetics for the ranges 68° - 78° are shown in Figure 5.22. The Lids which produce them are Figure 5.27. With these observations we can make an estimation of Lid growth with distance from the ridge axis.

To summarize, for data propagating right up the ridge axis in the Gulf of California we see no sign of any gradient. This is illustrated in Figures 5.32 and 5.31, which show that there is little to no EW gradient in upper mantle velocity which would yield a systematically faster first arrival for different raypaths traversing up the western Gulf of California or Baja Peninsula. Therefore, in light of other studies (eg, Neele (1996)) which show no low velocity zone and therefore no Lid under the Gulf, in this general region it is safe to say that the Lid has not yet formed over the distances traversed by these raypaths.

While the raypaths which cross the ridge probably exhibit a retardation in the vicinity of the crest and therefore require a Lid which is about 4 Km thinner than this and only 3.5% faster than standard TNA.

Moving west, the data in which we observe the fastest changing Lid structure occurs across raypaths all of which straddle the continental margin over the latter third of their propagation paths and straddle the ridge over the first third. Here the Lid structure appears to develop very quickly. Our best guess at its dimensions and development rate are a 3.5% velocity increase over 40 Km radially. Determining the exact lateral gradient is impossible because the raypaths do not parallel the ridge axis but rather fan out from a origin near the crest (Figure 5.18). Simply

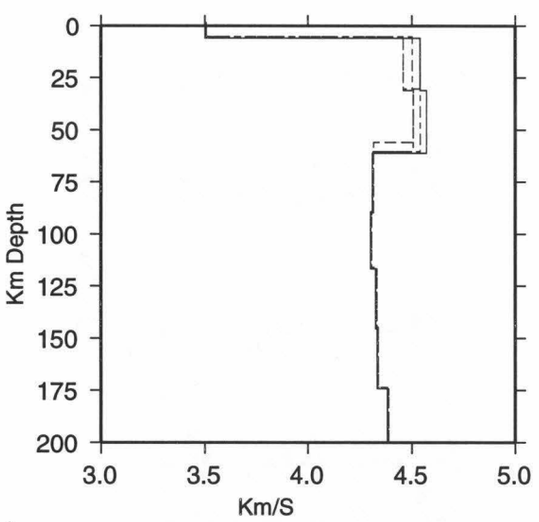

Figure 5.27: The fastest, thickest LID (solid) produces the best fitting synthetics for the raypaths corresponding to distancs of 57°-67° and 38°-48°, which travel the furthest from the ridge axis in the entire data set. The slowest and thinnest LID (even dashed) was that derived for the coastal *SS* data, whose raypaths straddle the ridge crest over half their propagation path. The intermediate model (uneven dashed) corresponds to the furthest ranges (68° - 78°, whose paths actually cross under the EPR about a third of the way through their propagation path (see Figure 5.3).

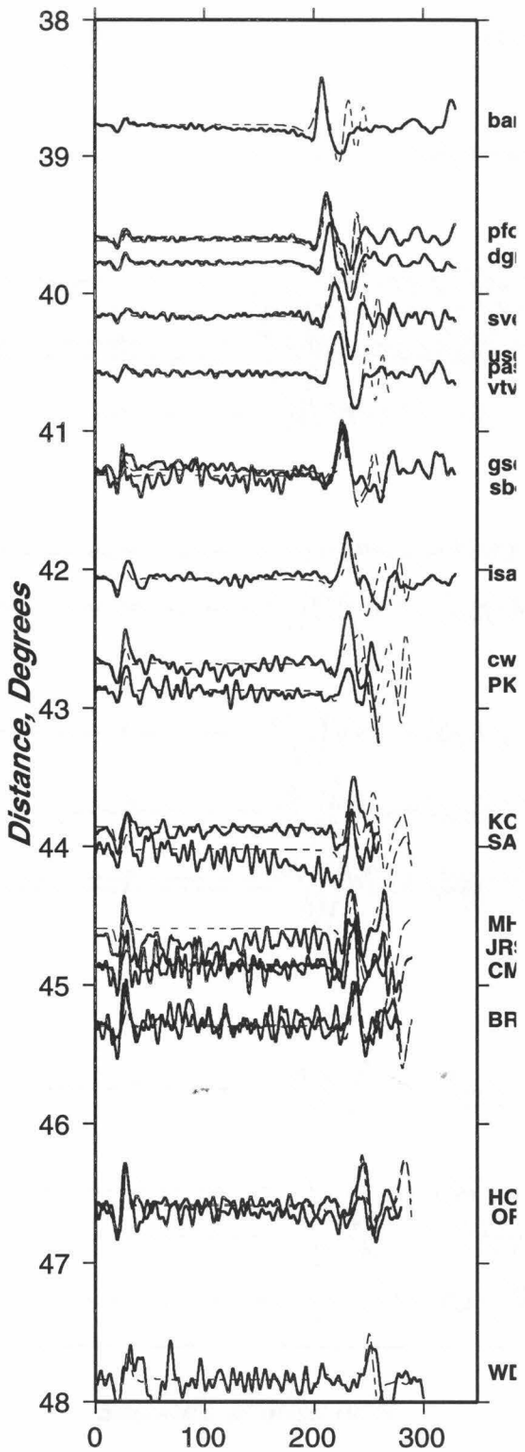

Figure 5.28: Data and Synthetics of *SS* 410 and 670 triplications calculated with a faster LID, shown in Figure 5.27. Here the synthetics of the triplication fit well over the entire range, and overall provide a better fit than the LID derived for the coastal *SS* data

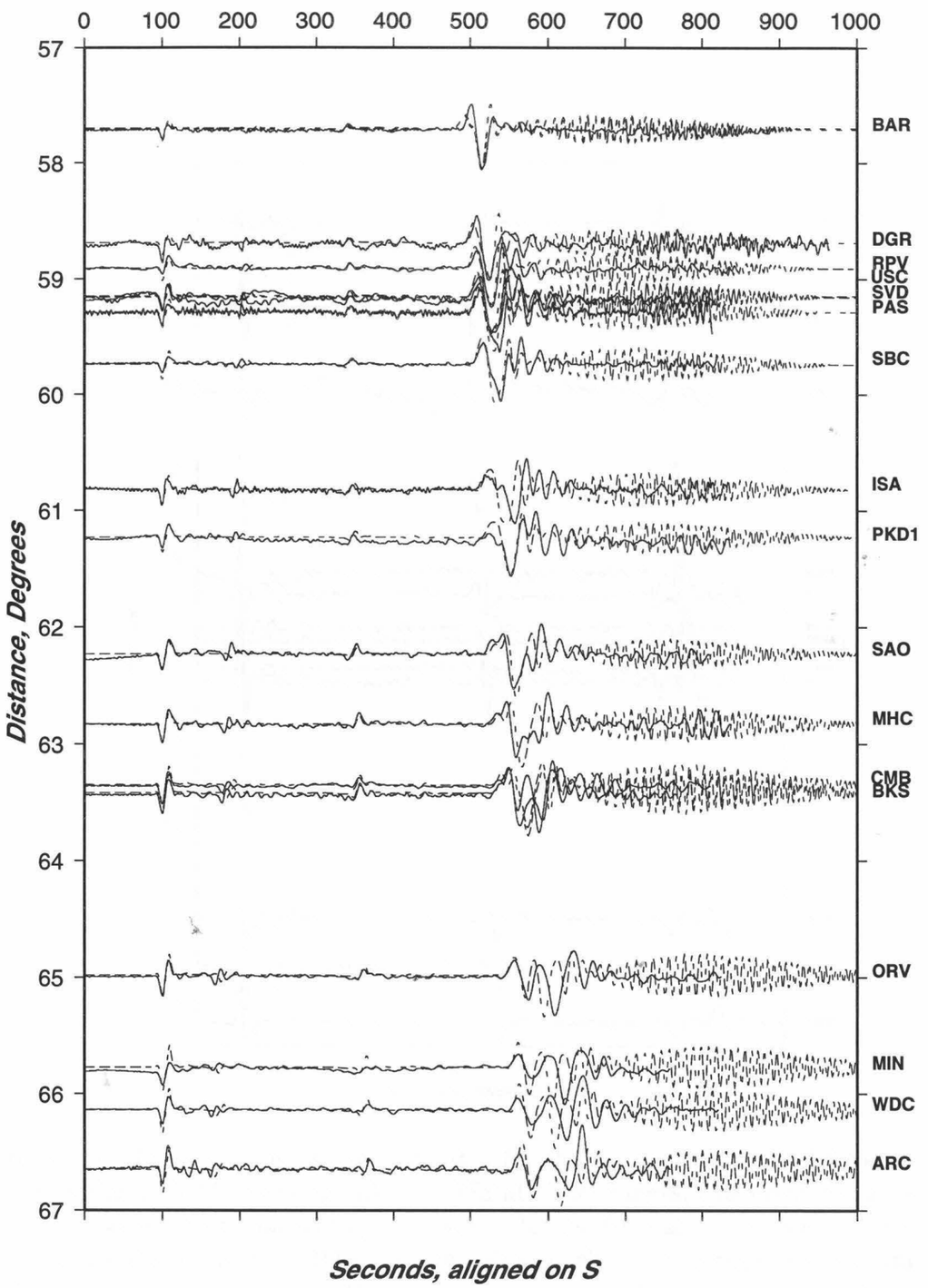

Figure 5.29: *SSS* synthetics for the open ocean LID structure. Overall, the whole seismogram fit is better with the addtionally LID structure than that derived for coastal *SS* data; the S-G timeing is better, and the individual 670 triplication phases line up substantially better.

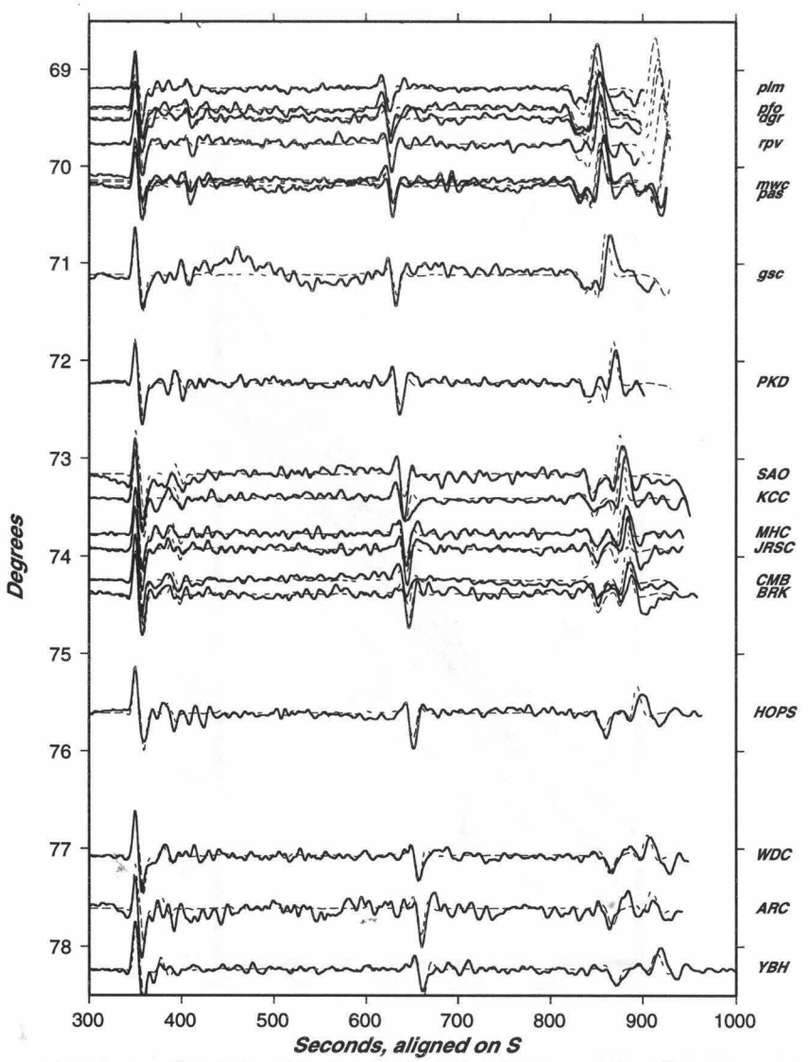

Figure 5.30: These synthetics are calculated for the medium thickness LID structure shown in Figure 5.27. Although like the *SSS* at closer ranges, this event has a geometry which causes the raypaths to propagate under the EPR and as a result the thinner LID reflects this inherently 2D structure. Most likely, for the regions traversing out under the open abyssal plains the LID structure should be there, but with our 1D approximate models we cannot resolve this.

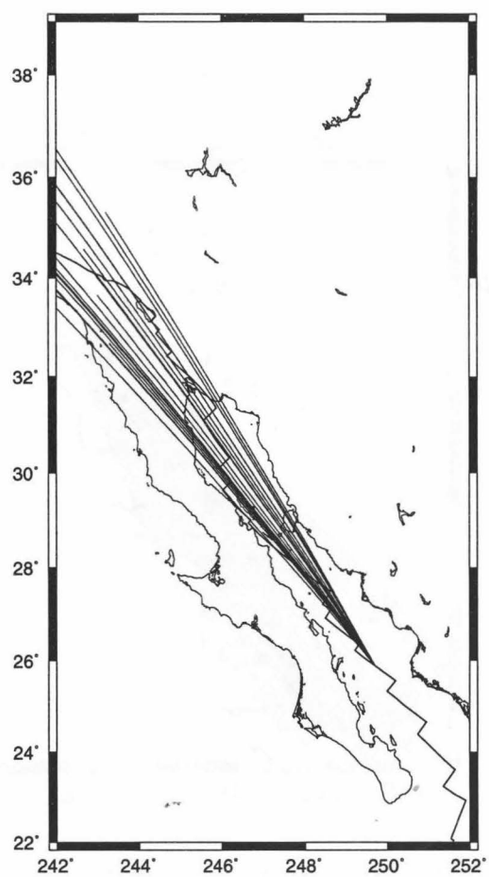

Figure 5.31: Raypaths for seismograms arriving between 12° and 22°. The majority of the raypaths here traverse under the ridge axis proper and their relative first arrival times show no clear correlation with azimuth, indicating a relatively uniform uppermost mantle structure.

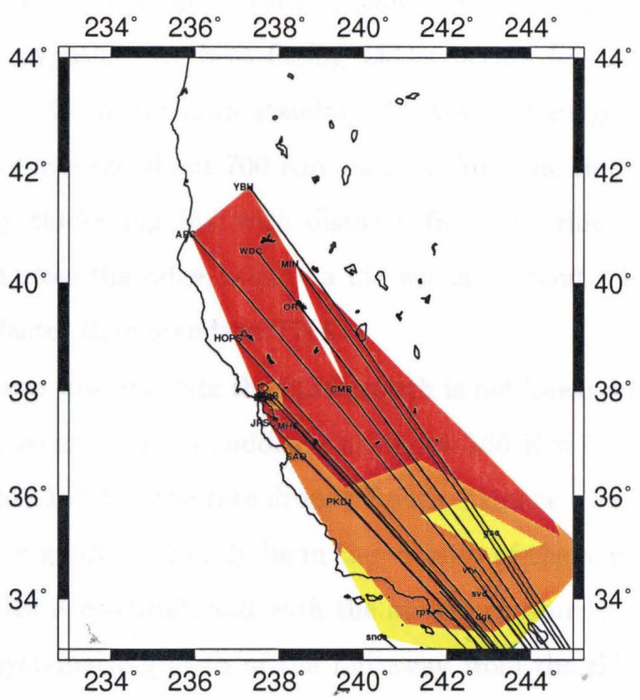

Figure 5.32: Contoured delay of S from that predicted by TNA. The lack of any EW patterns suggests that there is not much of a LID gradient in the central Gulf area. The range observed here is only a couple seconds, which is within our ability to pick.

taking the average horizontal separation of the rays indicates that the Lid starts to form approximately 100 Km from the ridge axis and is fully formed by 150 Km from the ridge crest, indicating a 3.5% velocity change over 50 Km laterally. As further verification of its existence, the addition of the Lid appropriate to these data for synthetics derived for the further off-axis paths reproduce the data better than synthetics which do not contain a Lid. The synthetics corresponding to the closer *SSS* phases, which travel furthest from the ridge axis and are essentially bouncing under the open ocean, however, are still to slow and require an even faster uppermost mantle. these raypaths, the best fitting Lid structure has a thickness of 58 Km and and is about 4% faster than standard TNA would suggest. The rays used to estimate this Lid average about 700 Km distance from the ridge crest, this indicates a systematically thickening Lid with distance from the ridge crest. The furthest raypaths, which cross the ridge, require a Lid which is about 4 Km thinner than this and only 3.5% faster than standard TNA.

These estimates also indicate that Lid growth is not linear with distance from the ridge. The Lid seems to form suddenly at about 100 Km from the ridge axis and outside of roughly 150 Km the rate drops off with distance from the ridge crest. The strongest velocity gradients clearly lie in the vicinity of the axis. Further quantification of these rates is essential, and with the abundant sources we should be able to document the systematic growth of the Lid away from the ridge axis. However, in this analysis, the fact that nearly all, rather than just a few, phases traversing paths away from the ridge crest proper which are sensitive to Lid structure consistently fit synthetics computed with the Lid better than those without it suggests that the structure is systematic in its growth and regional in extent rather than anomalous along-axis variation.

5.6 Discussion

The fundamental observation of a sharp Lid onset followed by moderate growth is limited by the fact that we can't constrain where specifically along the raypaths

these perturbations in the Lid actually occur. We are therefore forced to make the assumption that they are averaged along the entire path; ie, the velocity models are 1D. To a certain extent this makes sense, but precludes some interpretations which might bolster geochemical-based models of melt transportation in the vicinity of spreading ridges. This is a relevant worry in light of the differential spreading rates along different sections of the EPR as well as ideas relating to melt delivery in the form of 3D diapirs (Wang *et al.* (1996)). To a large degree the surface expressions of the ridge vicinity (eg, bathymetry, gravity, seamount chains) the first order affect appears to be distance from the ridge crest and so the 1D assumption is probably valid to the first order. Since, without orthogonal raypaths we cannot constrain where the propagation delays actually occur, we have no choice but to make this assumption. It does have some basis, however. Structurally, the largest feature in the region is the EPR crest itself, and since the direction of plate motion throughout the area is orthogonal to this ridge axis it stands to reason that first order variations in structure should be orthogonal to the ridge axis rather than along it. There is complication to this because some of the *SS* raypaths certainly interact with the continental margin of North America as well as the Baja California peninsula, but overall the paths are more or less cleanly separated from the continental margin.

The strong Lid gradient we find located on the order of 100 Km from the ridge axis bears on the major question of how melt is transported from the distributed melt production region in the uppermost mantle to the narrow ridge axis itself. This question was recently addressed by the multi-disciplinary MELT experiment, which placed 50 OBS across portions of the EPR sampled in this study (Forsyth *et al.* (1998)). The significant result of this study indicated that melt, or at least very low (3.8 Km/S) velocities, appears to be present beneath the EPR in a broad region several hundred Km across and extending to depths of the order of 100 Km. Additionally, the small melt percentage inferred from petrologic analysis indicates that melt is relatively mobile within its generation area Spiegelman and Elliott (1993). In our data, the sudden onset of the Lid for raypaths traversing approximately 150 Km off the ridge axis may be related to this observation as a spatial limitation on the

extent and distribution of partial melt. As shown in Figure 5.32, there is a noticeable lack of any gradient for the event in this study which travels up the Gulf of California and under the Baja Peninsula. Within our ability to pick the travel times, there is no discernible East-West bias of of first arriving energy and synthetics indicated that a standard TNA is entirely appropriate; there is no Lid or LVZ under the Gulf of California spreading center. Once our raypaths move off the ridge axis, though, we see a sudden onset of a fast high-velocity layer in the upper 60 Km of the mantle. This is consistent with the results of the Melt study, but in addition would seem to further constrain the distribution of partial melt to be uniform within a fixed region. The several hundred Km width of their inferred uniform partial melt zone predicts that energy propagating entirely within this region should not experience nearly as strong lateral gradients in velocity as groups of raypaths which straddle the edge of the melt region, particularly if the boundary is fairly sharp, as our *SS* data suggests it is. If a small percentage of melt is more or less uniformly distributed over a fixed source region, then raypaths straddling the edge of this source region will be exhibit extremely strong lateral gradient due to the melt-induced veloicty drop.

As an interesting side-note, for the energy propagating through the strong gradient region there seems to be no simple relationship between the Lid velocity structure and the overlying Baja Peninsula and North American margin, in that the onset of the Lid appears to be well inland of the topographic expression of the margin rather than on its edge. This would suggest that the velocity changes associated with the composition of the Baja California peninnsula does not extend into the uppermost mantle but rather seems to be a surface feature confined to the upper 10s of Km.

Bibliography

Allan, J., Geology of the northern Colima and Zacoalco grabens, Southwest Mexico: Late Cenozoic rifting in the Mexican volcanic belt, *Geol. Soc. Am. Bull.*, *97*, 473–485, 1986.

Anderson, D., *Theory of the Earth*, Blackwell, Oxford, 1989.

Bandy, B., , Ph.D. thesis, Tex. A&M Univ., College Station, 1992.

Barrientos, S., G. Plafker, and E. Lorca, Postseismic Coastal Uplift in Southern Chile, *Geophys. Res. Lett.*, *1992*, 701–704, 1992.

Benz, H., and J. Vidale, Sharpness of upper-mantle discontinuities determined from high-frequency reflections, *Nature*, *365*, 147–150, 1993.

Bina, C., and G. Helffrich, Phase transition Clapeyron slopes and transition zone seismic discontinuity topography, *J. Geophys. Res.*, *99*, 15,853–15,860, 1994.

Bina, C., and B. Wood, The olivine-spinel transitions: Experimental and thermodynamic constraints and implications for the nature of the 400-km seismic discontinuity, *J. Geophys. Res.*, *92*, 4853–4866, 1987.

Bucknam, R., G. Plafker, and R. Sharp, Fault movement (afterslip) following the Guatemala earthquake of February 4, 1976, *Geology*, *6*, 170–173, 1978.

Burdick, L., and D. Helmbeger, The upper mantle P velocity structure of the western United States, *J. Geophys. Res.*, *83*, 1699–1712, 1987.

Byrne, D., D. Davis, and L. Sykes, Loci and maximum size of thrust earthquakes and the mechanics of the shallow region of subduction zones, *Tectonics*, *7*, 833–857, 1988.

Chen, A., C. Frohlich, and G. Latham, Seismicity of the forearc marginal wedge (accretionary prism), *J. Geophys. Res.*, *87*, 3679, 1982.

Choy, G., and P. Richards, Pulse Distortion and Hilbert transformation in multiply reflected and refracted body waves, *Bull. Seism. Soc. Am.*, *65*, 1975.

Cohen, S., On the rapid postseismic uplift along Turnagain Arm, Alaska following the 1964 Prince William Sound earthquake, *Geophys. Res. Lett.*, *25*, 1213–1215, 1998.

Danobeitia, J., D. Cordoba, and L. D. et al., 1997 Fall Meeting Abstracts, 1997.

Davis, E. E., and R. D. Hyndman, Accretion and recent deformation of sediments along the northern Cascadia subduction zone, *Geol. Soc. Am. Bull.*, *101*, 1465–1480, 1989.

DeMets, C., and S. Stein, Present-day kinematics of the Rivera plate and implications for tectonics in Southwestern Mexico, *J. Geophys. Res.*, *95*, 21,931–21,948, 1990.

Ding, X., and S. Grand, Upper Mantle Q Structure Beneath the East Pacific Rise, *J. Geophys. Res.*, *98*, 1973–1985, 1993.

Dueker, K. G., and A. F. Sheehan, Mantle Discontinuity Structure from Midpoint Stacks of converted P-waves to S-waves across the Yellowstone hotspot track, *J. Geophys. Res.*, *102*, 8313–8327, 1997.

Dziewonski, A., and D. Anderson, Preliminary reference earth model, *Phys. Earth Planetary Int.*, *25*, 297–356, 1981.

Ferrari, L., and J. Rosas, Late Miocene to Quaternary extension at the northern boundary of the Jalisco block, western Mexico: the Tepic-Zacoalco rift revised, *Geol. Soc. Am. Bull.*, 1996.

Flanagan, M., and P. Shearer, Global Mapping of Topography on Transition Zone Velocity Discontinuities by stacking SS Precursors, *J. Geophys. Res.*, pp. 2673–2692, 1998.

Forsyth, D., S. Webb, and D. B. et al., Imaging the Deep Seismic Structure Beneath a Mid-Ocean Ridge: The MELT Experiment, *Science*, *280*, 1215–1217, 1998.

Gossler, J., and R. Kind, Seismic evidence for very deep roots of continents, *Earth and Planetary Sci. Lett.*, *138*, 1–13, 1996.

Grand, S., Mantle Shear Structure beneath the America and Surrounding oceans, *J. Geophys. Res.*, *99*, 11591–11621, 1994.

Grand, S., and D. Helmberger, Upper Mantle Shear Structure of North America, *Geophys. J. Int.*, 1984.

Heaton, T., and H. Kanamori, Seismic Potential Associated with Subduction in the Northwestern United States, *Bull. Seism. Soc. Am.*, pp. 933–941, 1984.

Heki, K., and Y. Tamura, Short-term afterslip in the 1994 Sanriku-Haruka-Oki Earthquake, *Geophys. Res. Lett.*, *24*, 3285–3288, 1997.

Heki, K., S. Miyazaki, and H. Tsuji, Silent fault slip following an interplate thrust earthquake at the Japan Trench, *Nature*, *386*, 595–598, 1997.

Helffrich, G., and C. Bina, Frequency dependence of the visibility and depths of mantle seismic discontinuities, *Geophys. Res. Lett.*, *21*, 2613–2616, 1994.

Helffrich, G., and B. Wood, 410 km discontinuity sharpness and the form of the olivine alpha-beta phase diagram - resolution of the apparent seismic contradictions, *Geophys. J. Int.*, *126*, F7–F12, 1996.

Helmberger, D., *Theory and Application of Synthetic Seismograms*, pp. 173–222, Soc. Italiana di Fisica, Bologna, Italy, 1983.

Hirahara, K., T. Nakano, and M. K. et al., GPS Observations of Post-Seismic Crustal Movements in the Focal Region of the 1995 Hyogo-ken nanbu Earthquake - Static and Real-Time Kinematic GPS Observations, *J. Phys. Earth*, *44*, 301–315, 1996.

Hudnut, K., *et al.*, Co-Seismic Displacements of the 1994 Northridge, California, Earthquake, *Bull. Seism. Soc. Am.*, *86*(1B), S19–S36, 1996.

Humphreys, E. D., and K. Dueker, Physical state of the western U.S. upper mantle, *J. Geophys. Res.*, *99*, 9635–9650, 1994.

Hyndman, R., and K. Wang, Thermal constraints on the zone of major thrust earthquake failure: the Cascadia subduction zone, *J. Geophys. Res.*, *100*, 22,133–22,154, 1995a.

Hyndman, R., and K. Wang, The Rupture zone of Cascadia great earthquakes from current deformation and the thermal regime, *J. Geophys. Res.*, *100*, 22,133–22,154, 1995b.

Ihmle, P., and J. Ruegg, Source tomography by simulated annealing using broadband surface waves and geodetic data: application to the mw=8.1 chile 1995 event, *Geophys. J. Int.*, *131*, 146–158, 1997.

Jordan, T., The continental tectosphere, *Rev. Geophys. Space Phys.*, *13*, 1–12, 1975.

Kanamori, H., Mode of Strain Release Associated with Major Earthquakes in Japan, *Annual Review of Earth and Planetary Sciences*, *1*, 213–239, 1973.

Kanamori, H., *Seismic and aseismic slip along subduction zones and their tectonic implications*, American Geophysical Union, Washington, D. C, 1977.

Katsura, T., and E. Ito, The system Mg2SiO4-Fe2SiO4 at high pressures and temperatues: precise determination of stabilities ov olivine, modified spinel, and spinel, *J. Geophys. Res.*, *94*, 15,663–15,670, 1989.

Kawasaki, I., Y. Asai, Y. Tamura, T. Sagiya, N. Mikami, Y. Okada, M. Sakata, and M. Kasahara, The 1992 Sanriku-Oki, Japan, Ultra-Slow Earthquake, *J. Phys. Earth*, *43*, 105–116, 1995.

Kikuchi, M., Yokohama City University Seismology Report, Electronic Publication, 1995.

Klotz, A., J. Reinking, and D. Angermann, Die Vermessung der Deformation de Erdoberflache, *Geowissenschaften*, *14*, 384–389, 1996.

Kostoglodov, V., and W. Bandy, Seismotectonic constraints on the convergence rate between the Rivera and North American plates, *J. Geophys. Res.*, *100*, 17,977–17,989, 1995.

Larsen, S., Geodetic Measurement of Deformation in Southern California, Ph.D. thesis, California Inst. of Technology, 1991.

Lichten, D., and J. S. Border, Strategies for high precision Global Positioning System orbit determination, *J. Geophys. Res.*, *92*, 12751–12762, 1987.

Marone, C., and C. H. Scholz, The depth of seismic faulting and the upper transition from stable to unstable slip regimes, *Geophys. Res. Lett.*, *15*, 621–624, 1988.

Marone, C., C. Scholtz, and R. Bilham, On the mechanics of afterslip, *J. Geophys. Res.*, *96*, 8441–8452, 1991.

McCaffrey, R., Influences of recurrence times and fault zone temperatures on the age-rate dependence of subduction zone seismicity, *J. Geophys. Res.*, *102*, 22839–22854, 1997.

Melbourne, T., I. Carmichael, C. DeMets, K. Hudnut, O. sanchez, J. Stock, G. Suarez, and F. Webb, The geodetic signature of the M8.0 Oct.9, 1995 Jalisco subduction earthquake, *Geophys. Res. Lett.*, *24*, 715–718, 1997.

Nakanishi, I., Reflections of P'P' from upper mantle discontinuities beneath the mid-Atlantic ridge, *Geophys. J.*, *93*, 335–346, 1988.

Nakano, T., and K. Hirahara, GPS observations of postseismic deformation for the 1995 Hyogo-ken Nanbu earthquake, Japan, *Geophys. Res. Lett.*, *24*, 503–506, 1997.

Neele, F., Sharp 400 Km Discontinuity from P Reflections, *Geophys. Res. Lett.*, *23*, 419–422, 1996.

Nishimura, T., H. Nakahara, H. Sato, and M. Ohtake, Source process of the 1994 Sanriku earthquake, Japan, as inferred from a broad-band seismogram, *Tohoku Geophys. J.*, *34*, 121,134, 1996.

Okada, Y., Internal deformation due to shear and tensile faults in a half-space, *Bull. Seism. Soc. Am.*, *82*, 1018–1040, 1993.

Okal, E., Seismic parameters controlling far-field tsunami amplitudes: A review, *Natural Hazards*, pp. 67–96, 1988.

Ortiz, M., J. Gonzalies, J. Reyes, and C. Nava, Efectos Costeros del Tsunami del 9 de Oictubre de 1995 en la Costa de Colima y Jalicso, *Tech. rep.*, Facultad de Ciencias Marina, Universidad de Colima, 1996.

Pacheco, J. F., L. R. Sykes, and C. H. Scholz, Nature of seismic coupling along simple plate boundaries of the subduction type, *J. Geophys. Res.*, *98*, 14133–14159, 1993.

Pardo, M., and G. Suarez, Steep subduction geometry of the Rivera plate beneath the Jalisco block in Western Mexico, *Geophys. Res. Lett.*, *20*, 2391–2394, 1993.

Polet, J., and D. Anderson, Depth extent of cratons as inferred from tomographic studies, *Geology*, *23*, 205–208, 1995.

Priestley, K., J. Cipar, A. Egorkin, and N. Pavlenkova, Upper-mantle velocity structure beneath the Siberian platform., *Geophys. J. Int.*, *118*, 369–378, 1994.

Revenaugh, J., and T. Jordan, Mantle Layering from ScS Reverberations 1. Waveform inversion of Zeroth-Order reverberations, *J. Geophys. Res.*, *96*, 19,749–19,762, 1991.

Ringwood, A., Phase transformations in the mantle, *Earth and Planetary Sci. Lett.*, *5*, 402–422, 1969.

Ruegg, J., *et al.*, The Mw=8.1 Antofagasta (North Chile) Earthquake of July 30, 1995: First results from teleseismic and geodetic data, *Geophys. Res. Lett.*, *23*, 917–920, 1996.

Satake, K., Mechanism of the 1992 Nicaragua Tsunami Earthquake, *Geophys. Res. Lett.*, *21*, 2519–2522, 1995.

Sato, T., K. Imanishi, and M. Kosuga, Three-stage rupture process of the 28 December 1994 Sanriku-oki earthquake, *Geophys. Res. Lett.*, *23*, 33–36, 1996.

Savage, J., A dislocation model of strain accumulation and release at a subduction zone, *J. Geophys. Res.*, *88*, 4984–4996, 1983.

Savage, J., and G. Plafker, Tide Gage Measurements of Uplift Along the South Coast of Alaska, *J. Geophys. Res.*, pp. 4325–4335, 1991.

Scherneck, H. G., A parametrized solid earth tide model and ocean tide loading effects for global geodetic base-line measurements, *Geophys. J. Int.*, *106*, 677–694, 1991.

Scholz, C., "Mechanics of Faulting", *Annu. Rev. Earth Plan. Sci. Lett.*, *17*, 309–334, 1989.

Scholz, C., Earthquakes and friction laws, *Nature*, *391*, 37–42, 1998.

Shearer, P., Constraints on upper mantle discontinuities from observations of long-period reflected and converted phases, *J. Geophys. Res.*, *96*, 18,147–18,182, 1991.

Shearer, P., Global mapping of upper mantle reflectors from long-period SS precursors, *Geophys. J. Int.*, *115*, 878–904, 1993.

Sipkin, S., and T. Jordan, Lateral heterogeneity of the upper mantle determined from the travel times of multiple ScS, *J. Geophys. Res.*, *81*, 6307–6320, 1976.

Smith, S. W., and M. Wyss, Displacement on the San Andreas fault subsequent to the 1966 Parkfield earthquake, *Bull. Seism. Soc. Am.*, *58*, 1955–1973, 1968.

Solomatov, V., and D. J. Stevenson, Can sharp seismic discontinuities be caused by non-equilibrium phase transformations?, *Earth and Planetary Sci. Lett.*, *125*, 267–279, 1994.

Spiegelman, M., and T. Elliott, Consequences of melt transport for uranium series disequilibrium in young lavas, *Earth and Planetary Sci. Lett.*, *118*, 1993.

Stixrude, L., Structure and sharpness of phase-transitions and mantle discontinuities, *J. Geophys. Res.*, *102*, 14835–14852, 1997.

Suarez, G., and O. Sanchez, Shallow depth of seismogenic coupling in southern Mexico: implications for the maximum size of earthquakes in the subduction zone, *Phys. Earth Planetary Int.*, *00*, 1–9, 1996.

Tabei, T., T. Ozawa, U. Data, K. Hirahara, and T. Nakano, Crustal deformation at the Nankai subduction zone, southwest Japan, derived from GPS measurements, *Geophys. Res. Lett.*, *23*(21), 3059–3062, 1996.

Tanioka, Y., L. Ruff, and K. Satake, The sanriku-oki, japan, earthquake fo december 28, 1994 (mw 7.7) - rupture of a different asperity from a previous earthquake, *Geophys. Res. Lett.*, *23*, 1465–1468, 1996.

Thatcher, W., The earthquake deformation cycle at the Nankai trough, Southwest Japan, *J. Geophys. Res.*, *89*, 3087–3101, 1984.

Thatcher, W., and N. Fujita, Deformation of the Mitaka Rhombus: Strain Buildup Following the 1923 Kanto Earthquake, Central Honshu, Japan, *J. Geophys. Res.*, *89*, 3102–3106, 1984.

Thatcher, W., and J. Rundle, A viscoelastic coupling model for the cyclic deformation due to periodically repeated earthquakes at subduction zones, *J. Geophys. Res.*, *89*, 7631–7640, 1984.

Tichelar, B., and L. Ruff, Depth of seismic coupling along subduction zones, *J. Geophys. Res.*, *98*, 2017–2037, 1993.

Tsuji, Y., Y. Hatanaka, S. Takeshi, and M. Hashimoto, Coseismic crustal deformation from the 1994 Hokkaido-Toho-Oki earthquake monitored by a nationwide continuous GPS array in Japan, *Geophys. Res. Lett.*, *22*(13), 1669–1672, 1995.

USGS, Preliminary determination of epicenters, United States Government Printing Office, 1995.

Vidale, J., X. Ding, and S. P. Grand, The 410-km-depth discontinuity: A sharpness estimate from near critical reflections, *Geophys. Res. Lett.*, *22*, 2557–2560, 1995.

Walck, M., The P-wave upper mantle structure beneath an active spreading centre: the Gulf of California, *Geophys. J. R. astr. Soc.*, *76*, 697–723, 1984.

Wang, X., J. Cochran, and G. Barth, Gravity anomalies, crustal thickness, and the pattern of mantle flow at the fast spreading east pacific rise, 9° - 10°- evidence for 3-dimensional upwelling, *J. Geophys. Res.*, *101*, 17927–17940, 1996.

Williams, P., and H. Magistrale, Slip along the Superstition Hills Fault Associated with the 24 November 1987 Superstition hills, California, Earthquake, *Bull. Seism. Soc. Am.*, pp. 390–410, 1989.

Wilson, D. S., and C. DeMets, Relative motions of the Pacific, Rivera, North American, and Cocos plates since 0.78 Ma, *J. Geophys. Res.*, *102*(B2), 2789–2806, 1997.

Zobin, V. M., The rupture history of the Mw 8.0 Jalisco, Mexico, earthquake of 1995 October 9, *Geophys. J. Int.*, *130*, 220–228, 1997.

Zumberge, J., R. Liu, and R. E. Neilan, International GPS Service for Geodynamics 1994 Annual Report, *J. Geophys. Res.*, 1995.

Zumberge, J., M. Heflin, D. Jefferson, M. Watkins, and F. Webb, Precise point positioning for the efficient and robust analysis of GPS data from large networks, *J. Geophys. Res.*, *102*, 5005–5017, 1997.